# Search for Supersymmetry with Jets, Missing Transverse Momentum, and a Single Tau at CMS

Dissertation

zur Erlangung des Doktorgrades

des Department Physik

der Universität Hamburg

vorgelegt von

Friederike Nowak

aus Hamburg

Hamburg

2012

| | |
|---|---|
| Gutachter der Dissertation: | Prof. Dr. Peter Schleper<br>Prof. Dr. Teruki Kamon |
| Gutachter der Disputation: | Dr. Isabell Melzer-Pellmann<br>Prof. Dr. Johannes Haller |
| Datum der Disputation: | 14. Mai 2012 |
| Vorsitzender des Prüfungsausschusses: | Dr. Georg Steinbrück |
| Vorsitzender des Promotionsausschusses: | Prof. Dr. Peter Hauschild |
| Leiterin des Fachbereichs Physik: | Prof. Dr. Daniela Pfannkuche |
| Dekan der Fakultät für Mathematik, Informatik und Naturwissenschaften: | Prof. Dr. Heinrich Graener |

# Abstract

This thesis presents a search for physics beyond the Standard Model with jets, missing transverse momentum, and a single tau. It aims especially at a cosmological favored region in Supersymmetry, the stau-LSP co-annihilation region with an enhanced production of taus. It is performed with data taken 2011 by the CMS experiment at the LHC, corresponding to an integrated luminosity of 5 $fb^{-1}$. The background was divided in two different contributions, one with real and one with fake taus. Both estimates were derived with data-driven techniques. The final measurement yields 28 events, while the number of background events was predicted to be 28.5 $\pm$ 2.6 (stat) $\pm$ 2.4 (syst), and thus, no deviation from the Standard Model could be found. As a result, exclusion limits on the supersymmetric cMSSM have been calculated.
Data taking and distribution imposes a challenge to the computing grid. To monitor the stability of the infrastructure, modules for Tier 2 operations within the HappyFace Project have been developed, tested, and taken into usage.



# Kurzfassung

In dieser Arbeit wird eine Suche nach Physik jenseits des Standardmodells mit Jets, fehlender transversaler Energie und einem Tau präsentiert. Sie ziehlt besonders auf eine kosmologisch bevorzugte Region von Supersymmetrie, der Stau-LSP Co-Anihilationsregion, in welcher häufig Taus produziert werden. Die verwendeten Daten aus 2011 entsprechen einer integrierten Luminosität von 5 $fb^{-1}$ und wurden mit dem CMS experiment am LHC genommen. Der Untergrund wurde aufgeteilt in einen solchen mit echten Taus, und einen solchen mit falsch identifizierten Taus, und mit datengetriebenen Methoden abgeschätzt. Die finale Selektion enthält 28 Ereignisse, während die Untergrundabschätzung 28.5 $\pm$ 2.6 (stat) $\pm$ 2.4 (syst) vorhersagt. Eine Abweichung von der theoretischen Vorhersage des Standard-Modells wurde nicht gefunden. Daher wurden Ausschlussgrenzen für diesen Kanal im supersymmetrischen cMSSM berechnet.
Datennahme und Verteilung sind eine Herausforderung für die Infrastruktur des Computings. Um ihre Stabilität und Funktionalität zu überwachen, wurden Module fuer das HappyFace Project entwickelt. Der Schwerpunkt lag hier in dem Betrieb von Tier 2 Centern.

# Contents

# List of Figures

# List of Tables

# Chapter 1

# Introduction

Since 40 years, the Standard Model dominates high energy physics. Although not a fundamental theory, its description of particle physics was and is extremely successful. Several of its predictions were found to be realized in nature. The formulation of quantum chromo dynamics in the beginning 1970s lead to the prediction of gluons, which where found in form of three-jet events at PETRA in 1979. The bottom quark was predicted 1973 in order to explain CP-violation, and indeed was found in 1977 at Fermilab. The top quark, also introduced 1973 due to CP-violation, was found 22 years later, at 1995, again at Fermilab. Also in 1973, the neutral currents where predicted as essential ingredient for the electroweak unification. Shortly after, in 1974, they were found at Gargamelle. The second to last particle left, the tau neutrino, which would complete the third generation of leptons, was found in 2000 by the DONUT collaboration. The last particle undiscovered is the Higgs boson, one of the main reasons for constructing the LHC[1].
Although the description of physics in the Standard Model is quite accurate, a few open questions remain. Gravity is not included in the Standard Model whatsoever. While the assumption of gravitational influences in particle physics is valid up to a scale of $10^{19}$ GeV, and thus, is no penalty to probing particle physics today, the inability to include gravity into a quantum field theory is a strong hint to physics beyond the Standard Model and to physics beyond the common mathematical descriptions. A second, not described phenomenon is the existence of dark matter indicated by cosmological measurements. After ruling out the neutrinos as a main source of this dark matter, the Standard Model does not provide any other candidate.
A lot of different new theories addressing one or more of the problems of the Standard Model have been introduced since its formulation. A prominent theory is Supersymmetry, which not only gives access to gravity, but also provides solutions to aesthetic issues of the current modeling of particle physics, such as the Higgs mass stabilization. It also includes a natural candidate for dark matter in the form cosmology suggests. Supersymmetry itself imposes little restrictions on its phenomenology. Here, again, cosmology shows a preference of certain signatures. The lightest supersymmetric particle, i.e. the dark matter candidate,

[1] Currently, hints of an higgs-like particle with the mass of around 125 GeV are seen by both ATLAS and CMS at the LHC, as well as CDF at the Tevatron.

is expected to have a mass of the order of $\mathcal{O}(100$ GeV). It can also be heavier, if the annihilation probability of the dark matter is enhanced, for instance by an annihilation via a resonance, e.g. a pseudo-scalar Higgs. Another possibility would be a co-annihilation with the second lightest supersymmetric particle. In some models, like the cMSSM, the stau can become such a co-annihilation partner, leading to an enhanced production of taus in the event. Thus, the tau-lepton is expected to be an interesting probe for new physics.
In the 2011 data taking period from March until November, the CMS experiment took 5 fb$^{-1}$ of data. In this thesis, the full dataset of 2011 was analyzed. A search for new physics focusing on Supersymmetry with one tau-lepton, jets and missing energy has been performed. The background in form of real taus from Standard Model processes, and fake taus from mis-identified jets, has been estimated with data-driven methods. The data has been found to be consistent with the Standard Model predictions.
Data taking and analyzing also imposes a great challenge to the LHC computing grid. To ensure the stability of the computing units, their networks, and the workflow within the grid, a constant and extensive surveillance of the system has to be maintained. This thesis also describes the development of Tier 2 related plug-in modules for The HappyFace Project.
The structure of this document is as follows. Chapter 2 introduces the basic theoretical concepts of the Standard Model and of Supersymmetry. In chapter 3, a brief description of the CMS detector is given, followed by a summary of the computing structure used at CMS, the description of The HappyFace Project and the developed modules in chapter 4. Chapter 5 contains event simulation, and in chapter 6, the object reconstruction is described, with special attention to tau reconstruction and identification. In chapter 7, the event selection is defined. The background estimate is described in chapter 8, the results and the interpretation of the results are presented in chapter 9. Finally, this thesis closes with a summary and an outlook in chapter 10.

# Chapter 2

# The Standard Model and Beyond

## 2.1 The Standard Model

The Standard Model [1] is an effective description of all known fundamental particles. It is very successful, even though there are open questions like the origin of masses. It describes matter particles and their interactions, and also includes a mechanism to generate masses.

### 2.1.1 Matter

Matter consists of fermions, i.e. particles with half-integer spin. Two types of fermions exists, the leptons and the quarks. The leptons include all electron-type particles, the electron, the muon, and the tau. They also include neutrino-like particles, the electron-neutrino, the muon-neutrino, and the tau-neutrino. The quarks include the up-type quarks, the up-quark, the charm-quark, and the top-quark, and the down-type quarks, the down-quark, the strange-quark, and the bottom-quark. All same-type particles differ only in their masses, not in their quantum numbers, and thus are arranged in three different "generations"[1], beginning with the lightest particles in the first generation, up to the heaviest particles in the third generation.
All fermions introduced here are in principle two disjunct particles, one with right-handed, and the other one with left-handed chirality, but with the same quantum numbers. In the Standard Model, they are treated as one particle with two different components, as they mix due to their equal masses. The left-handed components are arranged in doublets and the right-handed in singlets. Except for the neutrinos, all fermions of the second and third generation decay into the particles of the first generation, which are stable. All left-handed fermions are charged under the weak force. All electron-like and quark-like particle interact electromagnetically, and quark-like particles couple also via the strong interaction (see table 2.1).
All of these particles have been measured experimentally. The least known properties are

[1]This is not entirely true, as their mass eigenstates are not the same as the interaction eigenstates, which are written into the generation due to historical reasons.

| | 1 | 2 | 3 | charges |
|---|---|---|---|---|
| leptons | $\begin{pmatrix}\nu_e\\ e\end{pmatrix}_L$ | $\begin{pmatrix}\nu_\mu\\ \mu\end{pmatrix}_L$ | $\begin{pmatrix}\nu_\tau\\ \tau\end{pmatrix}_L$ | weak<br>weak, electromagnetic |
| | $e_R$ | $\mu_R$ | $\tau_R$ | electromagnetic |
| quarks | $\begin{pmatrix}u\\ d\end{pmatrix}_L$ | $\begin{pmatrix}c\\ s\end{pmatrix}_L$ | $\begin{pmatrix}t\\ b\end{pmatrix}_L$ | weak, electromagnetic, strong |
| | $u_R, d_R$ | $c_R, s_R$ | $b_R, t_R$ | electromagnetic, strong |

Table 2.1: Fermions of the Standard Model and their charges, arranged in the three generations. Only the left-handed fermions interact weakly and are arranged in doublets. The right-handed fermions are singlets. The right-handed neutrinos are not present in this table, as they do not interact with one of the forces of the Standard Model.

those of the neutrino sector, due to the tiny masses of the neutrinos.

### 2.1.2 Interactions

The interactions are mediated by bosons. They are the quanta of the gauge fields, and couple to the corresponding charges. The interactions are described by symmetry transformations U of the group SU($n$). They are unitary ($UU^\dagger = 1$) and special ($\det(U) = 1$). An operator

$$U(x) = \exp\left(i \sum_{a=1}^{n^2-1} \theta^a(x) T_a\right) \tag{2.1}$$

of this group has $n^2 - 1$ free parameters $\theta^a$ and generators $T_a$. For the generators, the relation

$$[T_a, T_b] = i f_{ab}^c T_c \tag{2.2}$$

is valid. If the structure constant $f_{ab}^c$ is zero, the generators commute, the corresponding gauge bosons are not charged, and the algebra is called "abelian".
The photon as mediator of the electromagnetic field and the $Z$ boson as carrier of the weak interaction are gauge bosons that are not charged themselves and therefore do not interact with other of their kind. The structure constant of the $W$ bosons and the gluons does not vanish, leading to self-interaction.

### The Strong Force

The symmetry group of "quantum chromo dynamics" (QCD) is the non-abelian SU(3) [2][3]. Their generators do not commute, and therefore, the mediators of the strong force, the gluons, carry the charge of the strong force ("color") themselves [4]. The SU(3) has eight free parameters, leading to eight gluons. Each gluon carries two strong charges: a color and another anticolor. The ninth possible combination of three colors and three anti-colors would be a gluon carrying a color and its corresponding anticolor, and thus, be uncharged. It is not part of the generators of the SU(3).
This attribute, gauge bosons being charged themselves and their masslessness[2] leads to the so-called "confinement"[3], which means that colored particles cannot exist freely. On the other hand, at small distances, these particles can be treated as free. If a particle gets enough energy to move away from the other particles (e.g. in a hard collision), it soon becomes energetically favorable to produce two new particles, neutralizing the color of the original ones. These particle composites are colorless ("white") from the outside, such that they can be treated as free particles. They are called "hadrons", and consist of either two ("mesons") or three ("baryons") quarks[4]. They usually appear in larger numbers, forming a so-called "jet" in the detector [6].

### The Electroweak Unification

The postulation of the conservation of the weak currents leads to the existence of gauge fields. For this, operators $\frac{1}{2}(1 \pm \gamma^5)$ were introduced, which project the fermion fields $\Psi$ to their right and left handed components $\psi^R$, $\psi^L$:

$$\Psi = \frac{1}{2}(1+\gamma^5)\Psi + \frac{1}{2}(1-\gamma^5)\Psi = \psi^R + \psi^L \tag{2.3}$$

The gamma matrix $\gamma^5 = i\gamma^0\gamma^1\gamma^2\gamma^3$ is derived from the Dirac equation. The left-handed lepton field can be formulated as a 2-component field:

$$\Psi_l^L(x) = \begin{pmatrix} \psi_{\nu l}^L(x) \\ \psi_l^L(x) \end{pmatrix} \tag{2.4}$$

The Lagrangian density can now be written as

$$\mathcal{L}_{0,l} = i[\bar{\Psi}_l^L(x)\partial\!\!\!/\Psi_l^L(x) + \bar{\psi}_l^R(x)\partial\!\!\!/\psi_l^R + \bar{\psi}_{\nu l}^R(x)\partial\!\!\!/\psi_{\nu l}^R] \tag{2.5}$$

with $\partial\!\!\!/ = \partial_\mu\gamma^\mu$. The particles, bosons as well as fermions, are set to be massless in order to keep the gauge invariance. The Lagrangian density has to be invariant under local SU(2) transformations $U(w_j) = \exp(ig\tau_j w_j(x)/2)$, as well as under local U(1) transformations

[2]Also the $W$ bosons are charged, but in this case, it is their mass that determines their reach, not their self-interaction.

[3]Also, the number of fermions $n_f$ and the number of colors $N_C$ must fulfill $11N_C - 2n_f > 0$, which is left out for simplicity.

[4]The next possible combination, "pentaquarks", has not been observed yet, but claimed [5].

$U(f) = \exp(ig'Yf(x))$. The $\tau_j$ are the Pauli spin matrices, $Y = Q/e - I_3^W$ is the hyper charge, $w_j, j = 1, 2, 3$ and $f(x)$ any differentiable functions and $g, g'$ real constants. The gauge fields $W_1(x), W_2(x), W_3(x)$ and $B(x)$ are the corresponding gauge fields to $U(w_j)$ and U(1), respectively. These new gauge fields can be absorbed into the now covariant derivative:

$$\mathcal{L}_{0,l} = i[\bar{\Psi}_l^L(x) \not{D} \Psi_l^L(x) + \bar{\psi}_l^R(x) \not{D} \psi_l^R + \bar{\psi}_{\nu l}^R(x) \not{D} \psi_\nu^R l] \tag{2.6}$$

with

$$D^\mu \Psi_l^L(x) = [\partial^\mu + ig\tau_j W_j^\mu(x)/2 - ig'B^\mu(x)/2]\Psi_l^L(x), \tag{2.7}$$

$$D^\mu \psi_l^R = [\partial^\mu - ig'B^\mu(x)]\psi_l^R, \tag{2.8}$$

and

$$D^\mu \psi_{\nu l}^R = \partial^\mu \psi_{\nu l}^R. \tag{2.9}$$

The electroweak bosons $W^\pm$, $Z$ and photon $A$ are the linear combinations of the gauge fields $W_i, B$:

$$W_\mu^\pm = \frac{1}{\sqrt{2}}[W_{1\mu}(x) \pm iW_{2\mu}(x)], \tag{2.10}$$

$$W_{3\mu}(x) = \cos\theta_W Z_\mu(x) + \sin\theta_W A_\mu(x), \tag{2.11}$$

and

$$B_\mu(x) = -\sin\theta_W Z_\mu(x) + \cos\theta_W A_\mu(x), \tag{2.12}$$

where $\theta_W$ is the weak angle [7]. The photon is massless and stable, the weak bosons $W^\pm, Z$ have a lifetime of $\sim 10^{-25}$ seconds and masses of $80.399 \pm 0.023$ GeV and $91.1876 \pm 0.0021$ GeV, respectively [8].

### 2.1.3 The Origin of Masses

The electroweak unification is not only a very elegant, but also a very successful theory. It predicted the weak current, represented by the $Z$-boson, which was later found at Gargamelle [9]. But as this gauge theory requires massless particles by design, a mechanism to give the particles their masses and to break the electroweak symmetry is needed. Furthermore, it must be constructed in a way that leaves the gauge invariance of the Lagrangian density intact. The currently most favored theory is the spontaneous symmetry breaking via the Higgs mechanism.

#### The Higgs Mechanism

In this theory, the lowest energy state (vacuum) is degenerated, i.e. it is no longer invariant under symmetry transformations, while the symmetry of the Lagrangian remains. A so-called "Higgs-field" is introduced, with a non-zero vacuum state. An ansatz of such a field is

$$\mathcal{L}(x) = [D^\mu \phi(x)][D_\mu \phi(x)] - \mu^2|\phi(x)|^2 - \lambda|\phi(x)|^4 - \frac{1}{4}F_{\mu\nu}(x)F^{\mu\nu}(x). \tag{2.13}$$

$F_{\mu\nu}(x) = \delta_\mu A_\nu(x) - \delta_\nu A_\mu(x)$ is the Lagrangian density of the free field, $D^\mu$ the covariant derivative, $\phi(x)$ the scalar Higgs field, and $\mu^2, \lambda$ real parameters.
Equation (2.13) is invariant under U(1) transformations, and therefore the photon is held massless. If the Higgs field is defined in multiple components, a similar invariance under SU(2) transformations can be avoided:

$$\Phi(x) = \begin{pmatrix} \phi_a(x) \\ \phi_b(x) \end{pmatrix} \tag{2.14}$$

It can be written in an arbitrary gauge:

$$\Phi(x) = \frac{1}{\sqrt{2}} \begin{pmatrix} \eta_1(x) + i\eta_2(x) \\ v + \sigma(x) + i\eta_3(x) \end{pmatrix} \tag{2.15}$$

with the four real fields $\sigma(x)$ and $\eta_i(x)$, $i = 1, 2, 3$, and $v = (-\mu^2/\lambda)^{-1/2}$. This can always be transformed to

$$\Phi(x) = \frac{1}{\sqrt{2}} \begin{pmatrix} 0 \\ v + \sigma(x) \end{pmatrix} \tag{2.16}$$

which does not include the $\eta_i$. These were absorbed by the boson fields $W^\pm, Z^0$, giving them their masses. The fermions gain their masses by a direct coupling to the higgs field $\sigma(x)$. The Higgs boson is not discovered yet, but hints of an higgs-like particle at a mass of approximately 125 GeV have been seen at different experiments [10][11][12].

### 2.1.4 Limitations of the Standard Model

Although the Standard Model is very successful in describing physics at the electroweak scale, a few questions remain:

- **Gravity**: The Standard Model does not include gravity and already for this reason alone, it cannot be a complete description of nature.
- **No Electrostrong Unification**: The hope of physics in the end is to unify all forces, but while the strong force is well represented by the SU(3), it is not unified with the other forces like it is the case for the electromagnetic and the weak force.
- **Dark Matter**: Astrophysical observations indicate a much greater accumulation of matter in the visible universe than can be explained by baryonic matter [13]. This "dark matter" cannot be explained by neutrinos, which could form only a small fraction of it. The "Modified Newtonian Dynamics" (MOND) [14] was developed in order to explain this excess within the existing theories. It was very successful, especially in explaining the measurement of galaxy rotation curves [15], until the bullet cluster [16] was discovered. Being actually two clusters passing each other, the bullet cluster shows a discrepancy between the center of the masses detected by direct observation and the center of the masses detected by gravitational lensing. This cannot be explained by MOND alone.

- **WW Scattering**: In the Standard Model, the four-vector-boson interaction becomes divergent with rising energy. If the Higgs mechanism turns out to be realized, a new term due to interactions of the vector-bosons with the Higgs is introduced, which cancels out this divergence. But this will only work, if the higgs mass is of the order of 100 GeV, and the WW scattering problem turns into the "fine-tuning" problem.

- **Neutrino Masses**: In the original Standard Model, neutrinos are set to be massless. Experiments showed that neutrinos indeed have non-zero masses [17]. In case of a sterile Dirac neutrino[5], the Standard Model can be extended to include massive neutrinos. If it turns out that neutrinos are Majorana particles[6], new physics beyond the Standard Model has to be introduced to explain the tiny masses of the neutrinos.

- **Hierarchy Problem**: In the Standard Model, the quantum corrections to the Higgs mass are quadratically divergent. If the Standard Model is assumed to be valid up to the Planck scale[7], these corrections are huge compared to the physical Higgs mass.

## 2.2 Physics Beyond the Standard Model

Several theories beyond the Standard Model have been proposed. The most popular is Supersymmetry. It provides a natural candidate for dark matter, as well as the possibility of the inclusion of gravity. In introducing a mechanism to convert fermions to bosons and vice versa, it potentially unifies matter with the forces. In an unbroken Supersymmetry, the divergent higgs mass corrections cancel out. Broken Supersymmetry still reduces the problem to a logarithmic dependence instead of a quadratic one, and thus the corrections becomes important at a much higher mass scale than without Supersymmetry.

### 2.2.1 Supersymmetry

Following the Coleman-Mandula-Theorem [18], there is no bosonic expansion of the Poincare group, which describes the symmetry transformations. There is, however, the possibility to extend with fermionic operators [19], as done in Supersymmetry. The first supersymmetric Lagrangian was introduced by Zumino and Wess [20] in 1974.
In the Standard Model, there is no possible transition between the fermions as matter particles, and the bosons as force mediators. In Supersymmetry, four-dimensional fermionic operators $Q^N$ are introduced, which allow the transformation of a fermion into a boson $Q|\text{fermion}\rangle \sim |\text{boson}\rangle$ and vice versa $Q|\text{boson}\rangle \sim |\text{fermion}\rangle$. The dimension $N$ gives the new number of freedom in the super space spanned by the fermionic operators. In the following, only the case where $N = 1$ is considered.
The operators form a Lie algebra [21]:

[5] In case of a Dirac neutrino, the right-handed component carry masses, but does not interact electromagnetically, strongly, or weakly, which is why it has not been observed.
[6] Majorana particles are identical to their anti-particles.
[7] The Planck scale at $10^{19}$ GeV is the scale at which gravitational corrections become important.

$$\{Q_\alpha, \bar{Q}_{\dot{\beta}}\} = 2\sigma^m_{\alpha\dot{\beta}} P_m \tag{2.17}$$

$$\{Q_\alpha, Q_\beta\} = \{\bar{Q}_{\dot{\alpha}}, \bar{Q}_{\dot{\beta}}\} = 0 \tag{2.18}$$

$$[P_m, Q_\alpha] = [P_m, \bar{Q}_{\dot{\beta}}] = 0 \tag{2.19}$$

$$[P_m, P_n] = 0 \tag{2.20}$$

$P$ is the energy-momentum-vector, $\sigma^m$ are the spin matrices, with $m, n = 0 \ldots 3$, and $\alpha, \dot{\beta} = 1, 2$. In case the operators $Q$ are defined locally, i.e. $Q = Q(x)$, $P$ is also local, and therefore would give a handle on (super)gravity.
The group elements of this Lie algebra can be written as

$$G(x, \theta, \bar{\theta}) = \exp(i(-x^m P_m + \theta Q + \bar{\theta}\bar{Q})), \tag{2.21}$$

where $z = (x, \theta, \bar{\theta})$ are the elements in the superspace. The $\theta$ have properties of Grassmann variables, i.e.

$$\int \theta\theta d^2\theta = 1 \quad \texttt{and} \quad \int \bar{\theta}\bar{\theta} d^2\bar{\theta} = 1. \tag{2.22}$$

For this reason, the expansion of a superfield $\Phi$ is finite and can be described like

$$\begin{aligned} \Phi = A(x) + i\theta\sigma^m\bar{\theta}\delta_m A(x) + (1/4)\theta\theta\bar{\theta}\bar{\theta}\Box A(x) \\ +\sqrt{2}\theta\psi(x) - (i/\sqrt{2})\theta\theta\delta_m\psi(x)\sigma^m\bar{\theta} + \theta\theta F(x). \end{aligned} \tag{2.23}$$

The Lagrange density now yields

$$\begin{aligned} \mathcal{L} = i\delta_m\bar{\psi}_i\bar{\sigma}^m\psi_i + A_i^*\Box A_i + (1/2)m_{ik}\psi_i\psi_k + (1/2)m_{ik}^*\bar{\psi}_i\bar{\psi}_k \\ -g_{ijk}\psi_i\psi_j A_k + g_{ijk}^*\bar{\psi}_i\bar{\psi}_j A_k^* + V(A_i, A_j). \end{aligned} \tag{2.24}$$

From the commutation relations follows the introduction of a superparticle to each standard model particle. The Higgs sector is built up by two Higgs doublets, in order to give both up-type and down-type fermions their masses[8] [22].
The super particles will now be denoted with an "s" in the front, if it is a boson ("selectron"), or an "ino" at the end, if it is a fermion ("gluino"). Furthermore, because all the super gauge bosons and higgsinos except the gluino have the same quantum numbers, they mix into mass eigenstates $\chi_i^0$, $i = 0, \ldots, 4$, and $\chi_j^+$, $j = 1, 2$. These particles are called "neutralinos" and "charginos", respectively, and are ordered by their masses w.l.o.g.

[8]This is the easiest way to generate masses in Supersymmetry via the Higgs, but one-doublet models or theories with more than two doublets are also possible.

### R-Parity

In supersymmetric processes, the baryon number and the lepton number are not preserved automatically. This would allow the proton to decay, while its lifetime is determined to $\geqslant 10^{32}$ years experimentally. The simplest way to solve this problem is to introduce a new quantity, the so-called "R-Parity":

$$R = (-1)^{3B-L+2S} \tag{2.25}$$

The baryon number $B$ is $1/3$ for quarks and $-1/3$ for anti-quarks, else 0. The lepton number $L$ is 1 for leptons, -1 for anti-leptons, and else 0. $S$ is the spin quantum number. Particles of the Standard Model have $R = 1$, those of Supersymmetry have $R = -1$. If $R$ is conserved, the consequence is that supersymmetric particles have to be produced in pairs, and the lightest supersymmetric particle (LSP) is stable. This LSP is a natural candidate for dark matter, as long as it is electromagnetically and strongly uncharged[9]. Then the LSP interacts at most via the weak interaction with normal matter, and will escape the detector unseen.
In this study, R-Parity conserving is always assumed.

### Breaking Supersymmetry

In pure Supersymmetry, the masses of the sparticles are the same as their Standard Model partners. In this case, they would have been observed already. Thus, Supersymmetry must be broken, to rise the masses of the sparticles above the current observation limits. Several breaking scenarios have been formulated. Some popular models are listed here:

- **Soft Supersymmetry Breaking**: This breaking scenario leaves supersymmetry renormalizable. The term "soft" refers to the aspect that Supersymmetry is broken in a way that does not introduce quadratic divergences and thus harm the higgs mass stabilization. It leads to the Minimal Supersymmetric Standard Model (MSSM), with at least 105 free parameters left [23]. In the MSSM, the breaking parameters are introduced as additional mass terms for the gauginos and sfermions in the Lagrangian, and their trilinear couplings.

- **Hidden Sector Framework**: The hidden sector framework is a subset of the soft Supersymmetry breaking. The theory is split up in a visible sector, including the Standard Model and Supersymmetry particles, and a hidden sector, where the breaking takes place. This breaking is mediated via messenger particles. The currently most prominent models in this framework are the constrained MSSM (cMSSM), in which gravity is the mediator, and the Gauge Mediated Symmetry Breaking (GMSB), where gauge interactions play the role of the messenger.

[9] In Supersymmetry, an electromagnetically or strongly charged LSP is possible. It would form anomalous heavy isotopes, which have not been observed so far.

| | |
|---|---|
| $m_0$ | Mass of the sfermions at the GUT scale |
| $m_{1/2}$ | Mass of the gauginos at the GUT scale |
| $A_0$ | Trilinear coupling at the GUT scale |
| $\tan\beta$ | Ratio of the vacuum expectation values of the higgs doublets |
| sign($\mu$) | sign of the Higgs mass parameter |

Table 2.2: Free parameters of the cMSSM breaking scenario.

| Benchmark | $m_0$ | $m_{1/2}$ | $A_0$ | $\tan\beta$ | sign($\mu$) | $\sigma$ [pb] | notes |
|---|---|---|---|---|---|---|---|
| LM2 | 185 | 350 | 0 | 35 | + | 0.6 | $B(\tilde{\tau}_1 \to \chi_1^0\tau) = 100\%$<br>$B(\chi_2^0 \to \tilde{\tau}_1\tau) = 96\%$<br>$B(\chi_1^+ \to \tilde{\tau}_1\nu) = 95\%$ |
| LM13 | 270 | 218 | -553 | 40 | + | 6.9 | $B(\tilde{\tau}_1 \to \chi_1^0\tau) = 100\%$<br>$B(\chi_2^0 \to \tilde{\tau}_1\tau) = 100\%$<br>$B(\chi_1^+ \to \tilde{\tau}_1\nu) = 100\%$ |

Table 2.3: CMS benchmark points in the cMSSM scenario used in this thesis. Listed are the defining values of $m_0$, $m_{1/2}$, $A_0$, $\tan\beta$, and sign($\mu$), and important decay modes. Also shown is the leading order cross section for proton-proton collisions at $\sqrt{s} = 7$ TeV. For both benchmark scenarios, the LSP is the lightest neutralino $\chi_1^0$ and the next-to-lightest supersymmetric particle (NLSP) is the $\tilde{\tau}_1$.

This thesis focuses on the cMSSM breaking scenario, which reduces the number of free parameters from 105 to 5. They are $m_0$, the unified mass of the sfermions at the GUT[10] scale, $m_{1/2}$, the unified mass of the gauginos at the GUT scale, $A_0$, the trilinear coupling of the scalar superfields at the GUT scale, $\tan\beta$, the ratio of the vacuum expectation values of the Higgs doublets, and sign($\mu$), the sign of the Higgs mass parameter $\mu$. They are listed in table 2.2.
CMS defined several benchmark points in this model. The ones used in this study for comparison with the Standard Model expectations are listed in table 2.3, together with some of their characteristics.

[10]The GUT (Grand Unified Theories) scale $\Lambda_{GUT} \approx 10^{16}$ GeV is the scale where the forces are unified.

### Taus in Supersymmetry

The soft breaking mass terms of the MSSM introduce a mixing between the sfermionic partners of the left- and right-handed fermions [24]. In case of no flavor mixing and in case of all parameters being real, the mixing matrix $\mathcal{M}_{\tilde{\tau}}$ in the basis of the gauge eigenstates $(\tilde{\tau}_L, \tilde{\tau}_R)$ reads

$$\mathcal{M}^2_{\tilde{\tau}} = \begin{pmatrix} m^2_\tau + m^2_{LL} & m_\tau X_\tau \\ m_\tau X_\tau & m^2_\tau + m^2_{RR} \end{pmatrix} \tag{2.26}$$

with

$$m^2_{LL} = m^2_{\tilde{L}_3} + (-1/2 + \sin^2\theta_W) M^2_Z \cos 2\beta$$
$$m^2_{RR} = m^2_{\tilde{E}_3} - \sin^2\theta_W M^2_Z \cos 2\beta$$
$$X_\tau = A_\tau - \mu \tan\beta$$

where $m_\tau$ is the mass of the tau, $M_Z$ is the mass of the $Z$-boson, $\theta_W$ the Weinberg angle, $m_{\tilde{L}_3}$ and $m_{\tilde{E}_3}$ are the left- and right-handed stau soft mass breaking terms, and $A_\tau$ is the trilinear stau-Higgs coupling $\tilde{\tau}_R \tilde{\tau}_L H_1$.
Although all sfermions have a similar mixing matrix, for the first and second generation, this mass mixing is negligible, if the soft-braking parameters for the first two generations are not orders of magnitude higher that for the third. Hence, $\tilde{q}_{L,R}$ with $\tilde{q} = \tilde{u}, \tilde{d}, \tilde{c}, \tilde{s}$ and $\tilde{l}_{R,L}$ with $l = e, \mu$ and $\tilde{\nu}$ are approximately real mass eigenstates, while the third generation mix to $\tilde{q}_{1,2}$ with $\tilde{q} = \tilde{b}, \tilde{t}$ and $\tilde{\tau}_{1,2}$, respectively. Per definition, the eigenstate with index 1 has the smaller mass.
The staus couple to the electroweak gauge bosons and their superpartners via gauge interactions, and to the Higgs and Higgsinos via the tau Yukawa coupling

$$Y_\tau = -g m_\tau / (\sqrt{2} m_W \cos\beta) \tag{2.27}$$

If $m_\tau \tan\beta$ is large, the mixing of $(\tilde{\tau}_L, \tilde{\tau}_R)$ becomes large, as well as the stau-Higgs and stau-Higgsino couplings. In the cMSSM, $\tan\beta$ can become as large as $\sim m_b/m_t$, values up to $40 - 50$ are possible [25].
Due to the large mixing, the mass of the $\tilde{\tau}_1$ can become small and can reach the mass of the LSP[11]. This region is one of the so-called "co-annihilation" regions. Due to the small mass difference, the taus produced in the decay of the $\tilde{\tau}_1$ into the LSP have small momenta.

### Cosmological Implications on the cMSSM

Since the measurement of galaxy rotation curves in 1959, several hints on non-baryonic dark matter in cosmology have been observed. The combination [26] of supernova, cluster, and cosmic microwave background [27] measurement indicates a universe with $\Omega_M = \frac{\rho_M}{\rho_{crit}} = 27\%$ and $\Omega_\Lambda = \frac{\rho_\Lambda}{\rho_{crit}} = 73\%$, where $\rho_M$ is the mass density of the universe, $\rho_\Lambda$ is the energy density, and $\rho_{crit}$ is the critical density of a flat universe (see figure 2.1). It was shown that only 4.4% of the matter contribution consists of baryonic matter.

[11] In principle, the $\tilde{\tau}_1$ can even become the LSP, but this is excluded due to reasons mentioned before.

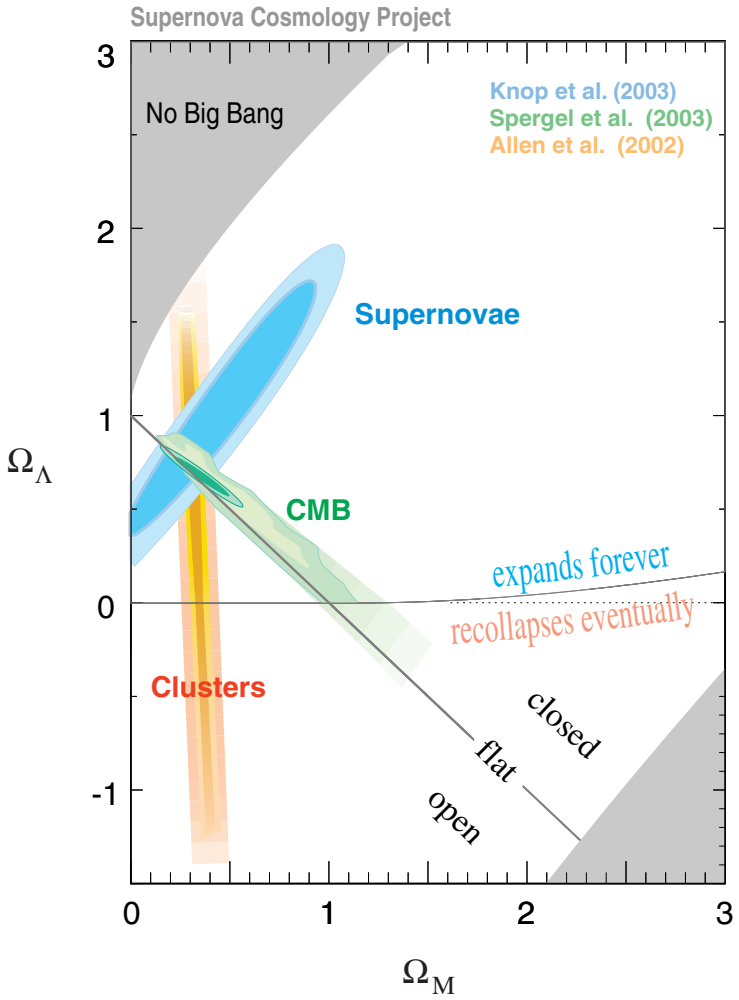


Figure 2.1: Combination of supernova, cluster, and cosmic microwave background (CMB) data to determine the mass $\Omega_M$ and energy $\Omega_\Lambda$ densities of the universe. From [26].

If the left-over dark matter contribution is identified with the supersymmetric LSP in the cMSSM [28], restrictions on the properties of the LSP can be made. The relic density was measured to be $\Omega_{\mathrm{DM}}h^2 = 0.1123 \pm 0.0035$ [27]. The allowed region by this measurement is then defined as a conservative $3\sigma$ limit, i.e. $0.101 < \Omega_{\mathrm{DM}}h^2 < 0.123$.

To lead to this measured dark matter, the LSP either has to be light ($\mathcal{O}(100)$) [29], the LSP-LSP annihilation is enhanced due to a resonance like the $A^0$ Higgs, or other processes despite LSP-LSP annihilation reducing the dark matter content in the universe must be present, for instance co-annihilation of the LSP with another superparticle. The $\tilde{\tau}$-LSP co-annihilation region mentioned before is one of these regions [30], where the stau and the LSP can (co-)annihilate:

$$\tilde{\tau}\ \text{LSP} \rightarrow \tau\ X. \tag{2.28}$$

Depending on the composition of the LSP, $X$ can be a photon, a $Z$-boson, or a neutral higgs.

Not only the relic density can be used as constraint on the cMSSM, but also other measurements. The anomalous magnetic moment of the muon $a_\mu$ is sensitive to contributions of physics beyond the Standard Model via loop corrections and current experiments find a $3.4\sigma$ deviance from the Standard Model predictions [31]. On the other hand, measurements on radiative b-quark decays $b \rightarrow X_s\gamma$, which are sensitive to flavor changing neutral currents, introduced by supersymmetry for instance, find the data in agreement to the Standard Model predictions [32]. In addition, the branching ratio of the decay of the $B_s^0$ into two muons can be enhanced by new physics. So far, this has not been seen [33]. Also the lower boundaries on the higgs and lightest chargino masses can be used.

Figure 2.2 [28] shows a combination of these measurements within the cMSSM. The green regions indicate the areas still allowed by relic density constraints. Also shown are boundaries by $a_\mu$ (red lines), the higgs mass (blue line), and $b \rightarrow X_s\gamma$ (cyan region). The measurement on $B_s^0$ has not been used. The red filled region indicates the area where the $\tilde{\tau}$ would be the LSP, and is therefore excluded. The green tunnel neighboring the excluded $\tilde{\tau} = \text{LSP}$ region is the $\tilde{\tau}$-LSP co-annihilation region. Note that in this figure older values for the measured quantities have been used. This has no impact on the motivation presented here. Note also that the allowed region shown depends severely on the assumed parameters, and is different for other values of $\tan\beta$, $A_0$, and $\text{sign}(\mu)$.

The possible co-annihilation reaction is not important for collider searches. However, the described configuration leads to supersymmetric decay chains, which include almost always a stau, as it would be the second lightest sparticle. In this case, in nearly each event one or more taus will be produced and can serve as a signature for a discovery. In the practical case, not each of the produced taus can be identified (see section 6). Thus, from the experimental side of view, many of the events with several taus will be single-tau events, on which this analysis concentrates.

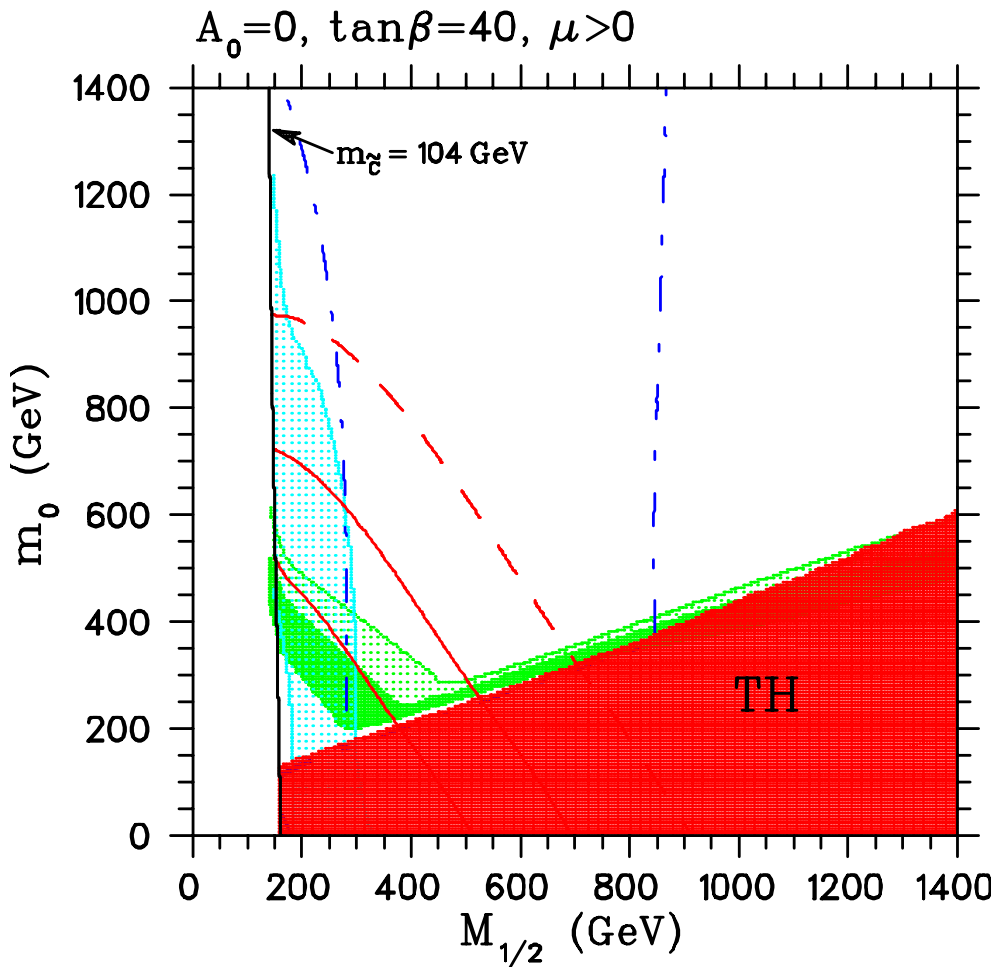


Figure 2.2: Allowed regions of the cMSSM at $\tan\beta = 40$ after applying constraints implied by the measurement of the cosmic microwave background. $m_0$ and $m_{1/2}$ are the free cMSSM mass parameters. The mass of the top is taken to be 175 GeV. The dark green shaded area denote the region where $0.08 < \Omega_{\rm DM}h^2 < 0.18$. For the light green shaded area, it is $0.18 < \Omega_{\rm DM}h^2 < 0.3$. The solid red lines mark the regions where the contributions of supersymmetry to the anomalous magnetic moment of the muon is $a_\mu^{SUSY} = (361 \pm 106) \times 10^{-11}$. The dashed red line is the boundary of the region for which the lower bound is moved to a $2\sigma$ limit. The dashed dotted blue line denote the outer boundaries where $113.5 \leq m_{Higgs} \leq 117.0$. The cyan shaded region is excluded due to $b \to X_s\gamma$. The lower boundaries of the lightest chargino mass $m_{\tilde{c}}$ are also shown. The red filled region labeled "TH" is excluded because the $\tilde{\tau}$ would be the LSP. The neighboring allowed green tunnel is the $\tilde{\tau}$-LSP co-annihilation region. From [28].

# Chapter 3

# Experimental Setup

## 3.1 The Large Hadron Collider

The Large Hadron Collider (LHC) is a proton-proton collider at the European Organization for Nuclear Research (CERN)[1], residing in the 26.7 km tunnel originally build for the Large Electron Positron Collider (LEP) [34]. It consists of two rings with counter-rotating beams, being crossed at four interaction points, point 1, 2, 5, and 8[2]. The proton beams are ramped up to the energy of 450 GeV by a chain of pre-accelerators, and are then injected into the LHC ring (figure 3.1). The LHC is using superconducting magnets, which are, due to very restrictive space in the tunnel, dedicated to both rings at one time. One of the also superconducting cables between these magnets caused an incident in 2008, where a bad thermal connection lead to up-heating of material and liquid helium [35]. The LHC was restarted in March 2010 [36] not running at the originally planned center-of-mass energy of 14 TeV, but at 7 TeV. The design luminosity L is $10^{34}$ $cm^{-2}s^{-1}$, with a bunch crossing every 25 ns.
Several experiments are hosted at the LHC. ATLAS (A Toroidal Lhc ApparatuS) [37] and CMS (Compact Muon Solenoid) [38] are multi-purpose detectors, aiming at Standard Model physics including higgs searches and physics beyond the Standard Model. LHCb [39] is dedicated to b-quark physics and the related problem of CP violation the matter-antimatter asymmetry in the universe. As the LHC can also be run in heavy ion (lead-lead) collision mode, one experiment, ALICE (A Large Ion Collider Experiment) [40], focuses on strongly interacting matter and quark-gluon plasma. Finally, another two experiments, LHCf [41] and TOTEM (TOTal Elastic and diffractive cross section Measurement) [42] are designed to study the total proton-proton interaction cross-section.

[1]The acronym CERN comes from "Conseil Européen pour la Recherche Nucléaire" (engl. European Council for Nuclear Research), which named the provisional council setting up the laboratory in 1954.
[2]The "missing" interaction points 3, 4, 6, and 7 were part of LEP and are not used by experiments.

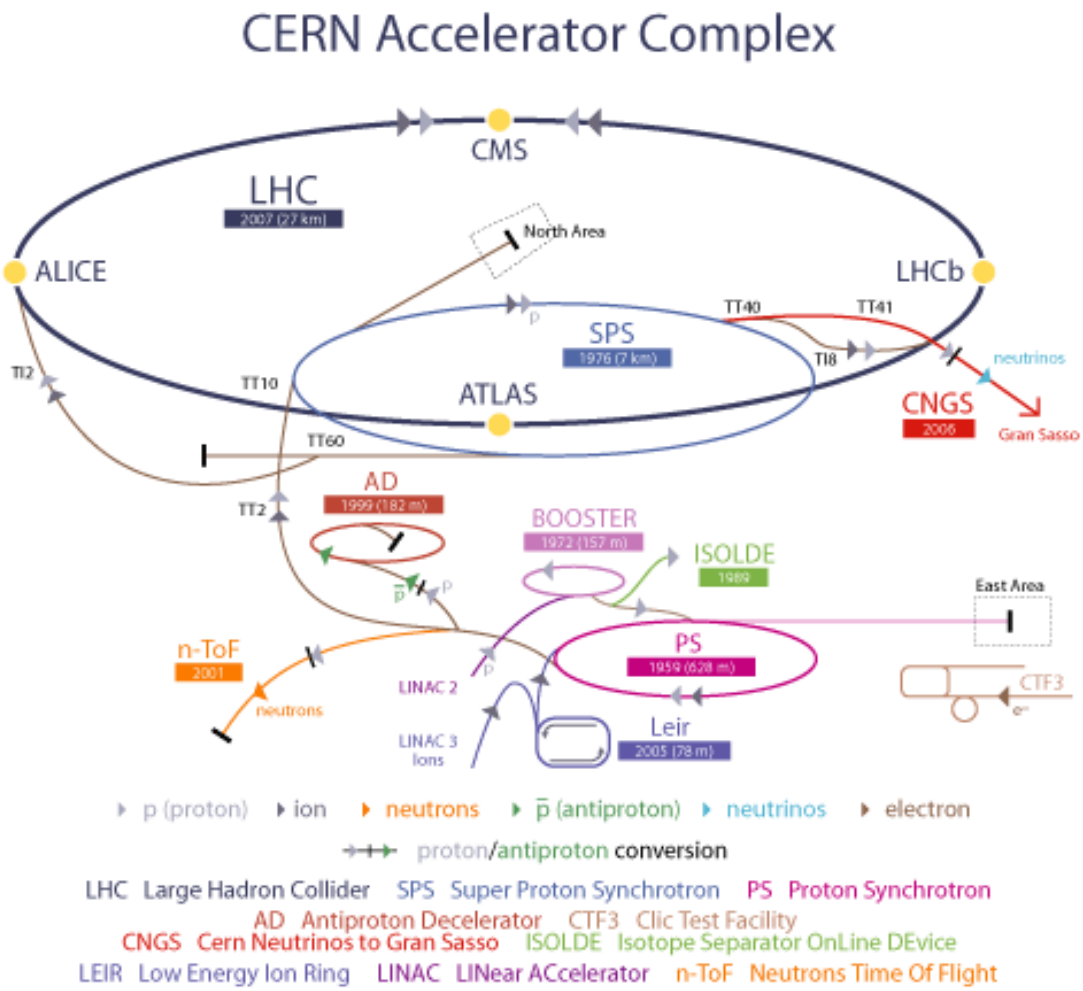


Figure 3.1: Schematic view of the LHC with its four big experiments. Also shown are the pre-accelerators, as well as several other experiments operated at CERN [43].

## 3.2 The Compact Muon Solenoid

The Compact Muon Solenoid (CMS) [44] is designed to fulfill two main tasks.

- **First**, survey and completion of the Standard Model. While many Standard Model parameters are already measured very precisely, some parts remain interesting. For instance, the increased production of top-quarks at the LHC will give the opportunity to measure not only its mass and the inclusive cross section, but also the differential cross section, the charge, and the spin. In addition, the only unknown part of the Standard Model remaining is the mechanism of Electroweak Symmetry Breaking. The most favored model is the higgs model, which predicts at least one new gauge

boson interacting with matter. This higgs-particle is not discovered yet, and thus CMS[3] was designed especially for this task.

- **Second**, physics beyond the Standard Model is of special interest, either in detecting discrepancies in precision measurements from the predictions, or even in direct discoveries.

To achieve good momentum measurements, a high magnetic field was chosen. Consequently, the solenoid magnet is the distinctive feature of CMS. Figure 3.2 shows the layout of the detector, beginning most inwards with the tracker near the beam pipe, going outward over the electromagnetic and the hadronic calorimeters, the solenoid, and the muon chambers within the return yoke.

### 3.2.1 The Tracker

The tracker system has to sustain a very high particle flux, while being responsible for a precise measurement of charged particle tracks at the same time [45]. It was decided to use silicon detectors only [46]. They differ in their granularity and in their position with respect to the beam pipe[4].

- **Pixel Detector:** The innermost tracker detector is the pixel detector. It consists of pixel sensors of the size 100 $\times$ 150 $\mu$m, arranged in layers (three in the barrel, two in the endcaps). The pixel detector is very important for the reconstruction of primary and secondary vertices and therefore crucial for the identification of heavy flavor quark (b,c) jets.

- **Tracker Inner Barrel and Disks:** The Tracker Inner Barrel and Disks (TIB/TID) belong to the strip detector following the pixel detector. The TIB is composed of four layers of silicon sensors containing the strips. The pitch of the strips varies from 80 to 120 $\mu$m, and the sensors have a size of 10cm $\times$ 80$\mu$m and a thickness of 320 $\mu$m. The Tracker Inner Disks comprises 3 disks with strips centered around the beamline, pointing to it.

- **Tracker Outer Barrel and End Cap:** As the radiation levels are smaller in the outer region than in the TIB, silicon sensors of the size of 25cm $\times$ 180 $\mu$m and the thickness of 500 $\mu$m are installed in six layers forming the Tracker Outer Barrel (TOB), allowing a better signal to noise ratio. The pitches of the strips vary from 120

[3]This is also true for ATLAS.

[4]In CMS, the $x$-axis points radially inward toward the LHC center, the $y$-axis points vertically upwards, and the $z$-axis is defined to point along the beam direction in the direction of the Jura mountains. The azimuthal angle $\phi$ is measured in the $x-y$ plane, with its point of origin at the $x$-axis. The polar angle $\theta$ is measured from the $z$-axis, the pseudorapidity $\eta$ is defined as $\eta = -\ln\tan(\theta/2)$ [44].

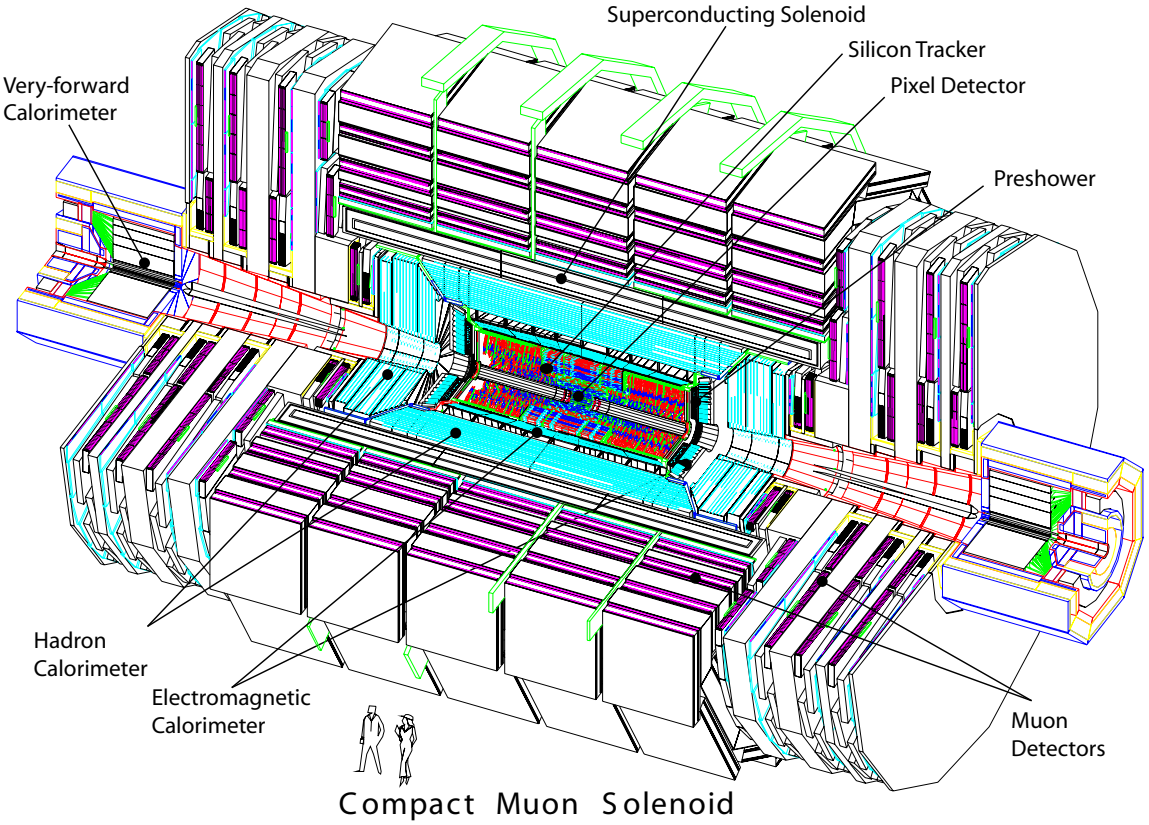


Figure 3.2: A cross-sectional view of the CMS experiment [44]. Except for the very-forward calorimeter, the marked detector parts are described in this chapter.

to 180 $\mu$m. In the Tracker End Cap (TEC), sensors of the thickness of 320 $\mu$m (inner four rings) and the thickness of 500 $\mu$m (outer rings) for both sides are installed. They are arranged in disks like in the TID.

Several of the strip layers are equipped with double modules, with the second module tilted against the first for enhancing the spatial resolution along the strips.
All in all, the tracker system covers the region up to $|\eta| < 2.5$.

### 3.2.2 The Electromagnetic Calorimeter

The electromagnetic calorimeter (ECAL) is made out of more then 60000 lead-tungstate crystals, arranged in "superclusters" of $5 \times 5$ crystals [44]. The crystal length corresponds to 25.8 radiation length[5] $X_0$, its cross section $\eta \times \phi \approx 0.0174 \times 0.0174$ [38]. The barrel area

[5]The radiation length of a material is defined as the distance where an electron looses all but 1/e of its energy by traveling through it.

ends at $|\eta| < 1.479$, the endcap region covers at $1.479 < |\eta| < 3.0$ .
The crystals are read out by photomultipliers, in the barrel region by avalanche photodiodes, in the endcap area by vacuum phototriodes.
The energy resolution of the ECAL is parametrized as a function of energy:

$$\left(\frac{\sigma}{E}\right)^2 = \left(\frac{S}{\sqrt{E}}\right)^2 + \left(\frac{N}{E}\right)^2 + C^2 \tag{3.1}$$

with a stochastic term S, a noise term N, and a constant term C. For $3 \times 3$ clusters, this has been measured to be

$$\left(\frac{\sigma}{E}\right)^2 = \left(\frac{2.8\%}{\sqrt{E}}\right)^2 + \left(\frac{0.12}{E}\right)^2 + (0.3\%)^2 \tag{3.2}$$

As the benchmark channel for the design of the ECAL was $H \to \gamma\gamma$, the most promising decay channel for $M_H < 130$ GeV, it is important to have a very good resolution for single, isolated photons. While in the barrel the distinction between a single photon and the decay of a $\pi^0$ to two photons closely together is possible due to the high granularity of the ECAL in that region, this might fail in the endcaps. Hence, a preshower detector resides at $1.653 < |\eta| < 2.6$ before the endcaps. It consists of two layers of lead to initiate the showering of photons and electrons, and a silicon strip layer for measuring the shower profiles for rejecting a $\pi^0$ with $P_T \approx 60$ GeV mimicking a single photon [47].

### 3.2.3 The Hadronic Calorimeter

The hadronic calorimeter (HCAL) follows the ECAL, but is still located inside the magnet, except the outermost layer. It consists of alternating layers of brass as absorber and plastic scintillator [44]. The innermost and the outermost layer are made out of stainless steel due to structural reasons. Together with the ECAL, the HCAL is arranged in towers, read out by single wavelength shifting fibers. The barrel area covers the region $|\eta| < 1.3$ and overlaps with the endcap, which ranges from $1.3 < |\eta| < 3.0$ [38]. In addition, the forward calorimeters cover the region from $2.9 < |\eta| < 5$. The scintillators have a granularity of $\Delta\eta \times \Delta\phi = 0.087 \times 0.087$ for $|\eta| < 1.6$ and $\Delta\eta \times \Delta\phi \approx 0.17 \times 0.17$ above. At the edge of the barrel region at $|\eta| < 1.3$, the absorber plates add up to an interaction length[6] $\lambda_I$ of 10.6 ($11.7\lambda_I$ with the ECAL material in front).
The energy resolution for particles above 5 GeV energy in the HCAL barrel combined with the ECAL is parametrized as $\sigma/E = a/\sqrt{E} \oplus b$, with $a = 0.847 \pm 0.016$ as stochastic term, and $b = 0.074 \pm 0.008$ as constant term [48].

### 3.2.4 The Magnet

One of the main features of CMS is the magnet. A superconducting niobium-titanium solenoid was chosen, for having a field parallel to the beams and a bending of tracks in

[6]The interaction length is the mean distance in a material, where the number of relativistic charged particles produced by a hadronic particle is reduced to 1/e.

the transverse plane [49]. It was designed to produce a field of 4 T in a volume of 6 m diameter and 12.5 m length [38], and is operated at 3.8 T. The return yoke is composed of 5 wheels and 2 endcaps, weighting a total of 10,000 tons.
The high magnetic field suppresses the muon trigger rates in comparison to a lower field. Because of this, CMS can renounce of a hard-wired level 2 trigger. It also increases the muon system and tracker resolution in comparison to a lower magnetic field, and also the calibration of the ECAL, done with e.g. $Z \rightarrow ee$ events, will be enhanced. The flux of charged particles reaching the ECAL is reduced with increasing field, lowering its occupancy.

### 3.2.5 The Muon Chambers

The muon chambers are interweaved with the magnet return yoke, which also serves as an hadron absorber for a clean signal. Because of the relatively low magnetic field ($\sim 1.2-1.8$ T [50]) and the low muon and neutron background rate, drift tube chambers are used in the barrel region ($|\eta| < 1.2$) [51]. They are operated with an $Ar/CO_2$ gas mixture and have a time resolution of a few nano seconds. The particle rate as well as the magnetic field is non-uniform and higher in the endcaps, hence, cathode strip chambers cover the region up to $|\eta| < 2.4$. In addition, resistive plate chambers are placed in the region where $|\eta| < 1.6$ [44]. They have a very good time resolution and are therefore used for muon triggering.
The standalone muon chamber resolution for muons with transverse momentum of 200 GeV is $\sim 9\%$, decreasing to 15%-40% at 1 TeV depending on the $|\eta|$-region. Together with the inner tracker system, this resolution is improved to 5% at 1 TeV [38].

## 3.3 Trigger

The trigger system is necessary to reduce the event rate from $10^9$ Hz to 100 Hz in order to be stored. This is done in two steps: the first system (Level-1, L1) is hardware based for increased speed, the second one (High-Level-Trigger, HLT) is based on commercial processors [52].

### 3.3.1 Level 1 Trigger

The L1 runs on those detector parts, which have fast readouts and can be combined with simplified object finding algorithms. These are the three muon chamber systems and the calorimeters. For the calorimeter, first, Trigger Primitive information (e.g. transformation of the input scale to the transverse energy scale, computation of the tower energy sum, etc) are calculated and then used to identify loosely defined electrons, photons, muons and jets. The type of these objects as well as the transverse energy threshold chosen will define the rate of the combined L1 triggers. As the aim of the L1 is to reduce the rate to 100 kHz, the thresholds can become very high. To still keep low threshold triggered objects, a

trigger path can be prescaled by a factor of x, such that only the x-th triggered event will pass.
While the L1 is running, the full detector output is stored in a pipeline for 3.2 $\mu$s to be given to the HLT in case of a positive L1 decision.

### 3.3.2 High Level Trigger

The purpose of the HLT is to reduce the rate further to 100 Hz [53]. This number is driven by the archival storage capability, which lies at $\approx$ 100 MB/s. It is a pure software trigger system running on commercial processors, thus benefiting from both reduced cost and proceeding development of this technology. Another important advantage is the flexibility in the design of the individual triggers, as they can access the full detector information. Hence, the algorithm defining the trigger objects must be carefully written to be both fast enough to provide a substantial reduction of the rate, as well as being as close to the algorithms used in physics analyses as possible. The HLT is divided in many virtual trigger levels, each using different detector parts and trying to reject the event as fast as possible. The reasons for L1 and HLT decision are stored with the event.

# Chapter 4

# CMS Computing and The HappyFace Project

Around 15 Petabyte of data are expected to be produced by the LHC experiments per year, and analyzed by around 8000 physicists. The storage, networking, and processing power needed for storing and analyzing this data are well beyond the scope of a reasonable and affordable centralized computing model [54]. For CMS alone, currently approximately 50 Petabytes of disk storage, around 70 Petabyte of tape storage, and roughly 600 kHS06[1] of CPU power are installed [58]. Hence, the decision to distribute the computing tasks both geographically as well as in function was made [59]. CMS has organized its computing resources and services in tiers embedded in a grid called the "Worldwide LHC Computing Grid" (WLCG) [60], developed and maintained in conjunction with the other LHC experiments. Currently, over 140 sites in 35 countries are part of the WLCG.

## 4.1 The Tiered Computing Structure

A distributed tiered structure benefits from already existing resources and the expertise of the (also distributed) CMS members. In addition, due to redundancy, it provides robustness and data security. The multiple tasks to be carried out are assigned to three different layers[2], called Tier 0, Tier 1, and Tier 2 centers, defined by service agreements specified in a Memorandum of Understanding [61]. Beginning from the HLT, the data migrates in various steps to the Tier 2 centers, where in the end the analyses take place. Figure 4.1 illustrates this process, which will also be explained in detail in the following:

- **Tier 0 center**: The data (RAW) collected by the CMS detector and selected by the HLT will first reach the Tier 0 located at CERN. A copy of this RAW data

[1] The HEP-SPEC2006 CPU benchmark (HS06) [55] [56] is based on the SPEC CPU2006 [57] benchmark. It consists of source code to be compiled on the system for measuring the performance.

[2] The fourth layer, the Tier 3, can be anything between a laptop and a center with the resources of a large Tier 2. But as it is not defined by CMS and has not to fulfill any formal requirements, it is left out here.

is immediately stored on safe and permanent mass storage. The CERN Analysis Facility (CAF) [62] is connected to the Tier 0, allowing for a first offline data quality monitoring. On the CAF, the alignment and calibration constants are computed from a first express reconstruction (within 1-2 hours) of a small subset of data done on the Tier 0. These constants are then used for a reconstruction (RECO) of the full data present at the Tier 0. Datasets reconstructed in this way are referred to as "Prompt". The resulting RECO datasets as well as a copy of each RAW dataset are then transferred to at least one of the Tier 1 centers.

- **Tier 1 centers**: Both the RAW as well as the RECO dataset received from the Tier 0 will be saved on mass storage. Due to this strategy, each set of RAW data is always present at at least two different computing centers distributed over the world. At the Tier 1 centers, a re-reprocessing of the RAW data with improved calibration is done. The corresponding datasets are called "ReReco". Another data layer is produced here, the Analysis Object Data (AOD), which is a subset of the RECO data, and has the advantage of reduced size. In addition, the datasets are skimmed with respect to different triggers ("Skim"), classifying the data due to different physics interest.
  The AOD skims and, if needed, also RECO datasets are distributed further to the Tier 2 centers.

- **Tier 2 centers**: The Tier 2 centers are dedicated to physics analyses. Hence, they must provide primarily CPU and intermediate storage recourses. Each CMS user has access to one of the Tier 2 centers, and the Tier 2 centers have to provide a certain amount of storage to both central processes (e.g. the Skims received from the Tier 1 centers) as well as private users.
  The main central task beside hosting physics analyses is to reconstruct simulated data. While the pure simulation of events (Monte-Carlo events, MC) is done on the Tier 1 centers, the simulation of the detector hits and the following physics object reconstruction based on the simulated hits is done on the Tier 2 centers. The resulting MC data files are transferred back to the Tier 1 centers, where they are collected and combined to a dataset, and then again distributed to dedicated Tier 2 sites for analysis.

### 4.1.1 Network Connections

The sites are connected by high-speed networks [64]. The stable and reliable data flow between the Tier 0 center and the Tier 1 centers (RAW and RECO distribution), in-between Tier 1 centers (further data distribution) and between the Tier 1 and Tier 2 centers (Skims in the one, MC samples in the other direction) is crucial for the computing model[3]. A certification procedure was defined using a traffic generator to test the quality of the connections. A link is declared commissioned, if it can demonstrate to be able to

[3]Connections between Tier 2 centers are also allowed, but are not part of the original computing model.

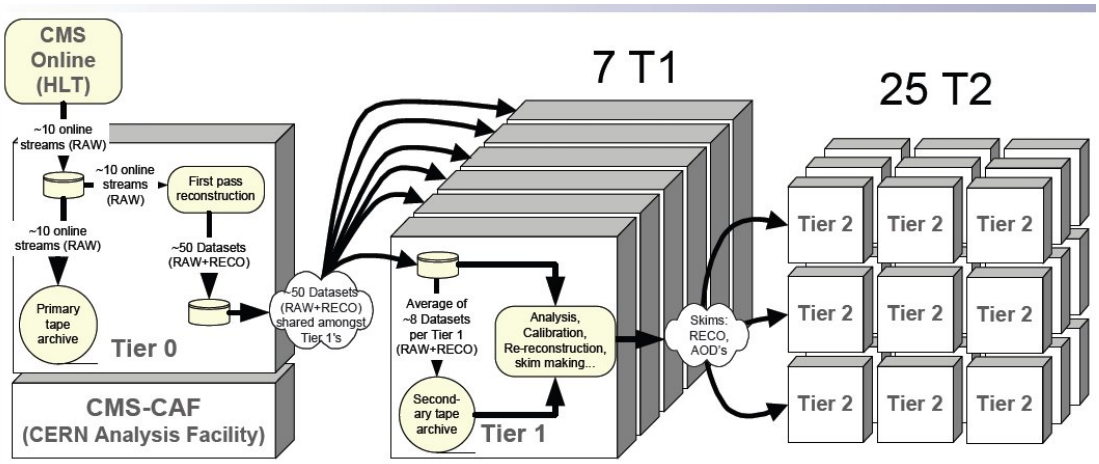


Figure 4.1: Schematic view of the data flow in the CMS computing model [63].

keep up an average traffic rate. At the time of the definition of this test, this was selected to 20 MB/s average over 24 hours for links between the Tier 0 and a Tier 1 or in-between Tier 1 sites, and 5 MB/s for links between Tier 1 and Tier 2 sites.

## 4.2 Data Transfer

Data distribution in CMS is managed by the "Physics Experiment Data Export" service (PhEDEx) [65]. It consists of a transfer management database (TMDB), automated global transfer agents, responsible for transferring files through the grid, automated local transfer agents for preparing transfered files for analysis, automated managing agents, tools for data requests, and finally monitoring tools. These agents [66] are simple processes that propagate files through the various stages of transfer. They are autonomous and do not communicate directly with each other, but via a "blackboard", the TMDB. PhEDEx is developed centrally and updates are released periodically.

## 4.3 Monitoring

Due to the very complex and also distributed nature of the CMS computing system, it is crucial to monitor the single components in order to keep the sites running. The DESY Tier 2 for instance provides approximately 1 Petabyte of storage (which is 5% of the installed storage of all Tier 2 sites within CMS) and roughly 30 kHS06 of CPU power to CMS users. In has to maintain not only the hardware, but also the software running the services, like the virtual file system dCache [67], PhEDEx for data distribution, the grid middleware gLite [68], and the CMS Software (CMSSW) [44]. Several tools for surveillance have been developed, focusing on different aspects. The following list is by far not complete, and its

elements are under ongoing development:

- **Service Availability Monitor:** Services provided by the WLCG are commonly tested by a framework called "Service Availability Monitor" (SAM). It consists of a uniform platform for executing the tests and a central database storing their results. The test scripts (sensors) are plug-in modules and are either containers or individual code units [69].
  CMS has adopted these tests to check if a CMS site is correctly embedded in the grid. This includes tests that determine if a job can be sent to a site and run there, tests that check if the CMS software is properly installed and configured, tests for accessing local data in a job, and also tests that copy data in and out of local storage [70].

- **Job Robot:** In addition to the test jobs created by SAM, the so-called "Job Robot" was developed. Unlike SAM, it uses the CMS job submission tool (CMS Remote Analysis Builder, CRAB [71]). As it submits its test jobs at a higher rate with respect to SAM, the load on the storage system is higher. Also, the accessed dataset can be distributed over several disks. With this characteristics, it performs more like an analysis job than a simple test.

- **Dashboard:** The "Experiment Dashboard" [72] is a generic tool, providing user-centric monitoring data. It uses multiple sources of information, including other grid monitoring tools. It is not coupled to a given infrastructure or middleware, and is used by various experiments including CMS. The Dashboard provides a web-based user interface, making a graphical interpretation of the monitoring data available.

- **Site Readiness:** In order to enhance the stability and reliability of sites, CMS has defined "Site Readiness" criteria. The Site Readiness depends on the number of successful SAM and Job Robot tests per day, as well as the number of commissioned and active links to other CMS sites. It also accounts for scheduled downtimes of a site. It is used to determine if a site fulfills all requirements in terms of availability and accessibility from the CMS point of view, and is therefore an important monitor for the individual CMS sites.

## 4.4 The HappyFace Project

Many difficulties in maintaining a site arise from the fact that the site has not only to monitor local aspects, like computing and storage elements, but also experiment specific ones, e.g. the connectivity to other sites, incoming and outgoing data transfers, and the embedding of the local system into the grid. While all of these components are monitored separately by individual systems (e.g. SAM, Job Robot), or even collected on a user-centered basis (Dashboard), site-centered monitoring remains problematic. Usually, shifters would carry out the task of collecting and reviewing the monitoring data. As some of the monitoring tools have long loading times, this can occupy the shifter for a long

period. In addition, because the shifter is often a non-expert, identifying and interpreting of relevant but rather unstructured information becomes a difficult task.
The "HappyFace Project" [73][74][75] is a meta-monitoring tool written in Python, developed to carry out the gathering of monitoring data obtained by other tools. It also provides a pre-evaluation, rating the information in three categories: *critical*, *warning*, and *everything is fine*[4].
It consists of two parts. The first part is the "HappyCore", which provides all basic functionalities. It is responsible for the regular ($\mathcal{O}$(15 min)) execution of the modules, the initialization and access of the database (SQLite [76]), calculation of the combined rating of the modules, and finally the visualization of the data by generating a dynamic webpage. The easy-to-plug-in modules are the second part of HappyFace. They are specialized test scripts, querying external monitoring data. A module will evaluate the collected information according to its configuration. A PHP fragment, containing the logic for the database query, is produced by the modules and collected and assembled by the HappyCore. The modules are grouped and displayed in categories for easy access. Figure 4.2 illustrates the workflow of the framework.

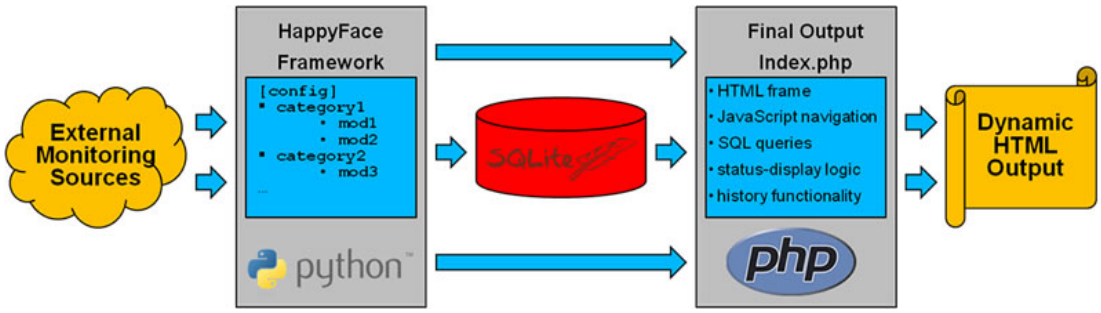


Figure 4.2: Workflow of the framework. Modules embedded in the HappyCore collect monitoring data from external sources, which are then stored in a database. This database is read out by a dynamic HTML website [73].

Another feature of HappyFace is the possibility to make date-dependent queries to the database, forming a history functionality that can be used to analyze the site's performance over time. It also provides the possibility to make trend plots of the different modules. In addition, an external "Firefox" plugin exists, which displays the status of a given HappyFace instance in an condensed and easy-to-access way.
Figure 4.3 shows the webpage of the HappyFace instance [77] used at the Tier 2 at "Deutsches Elektronen SYnchrotron" (DESY) [78].

[4]This rating was originally visualized by three different face icons: a crying face, a moderate face, and a happy face, giving the project its name.

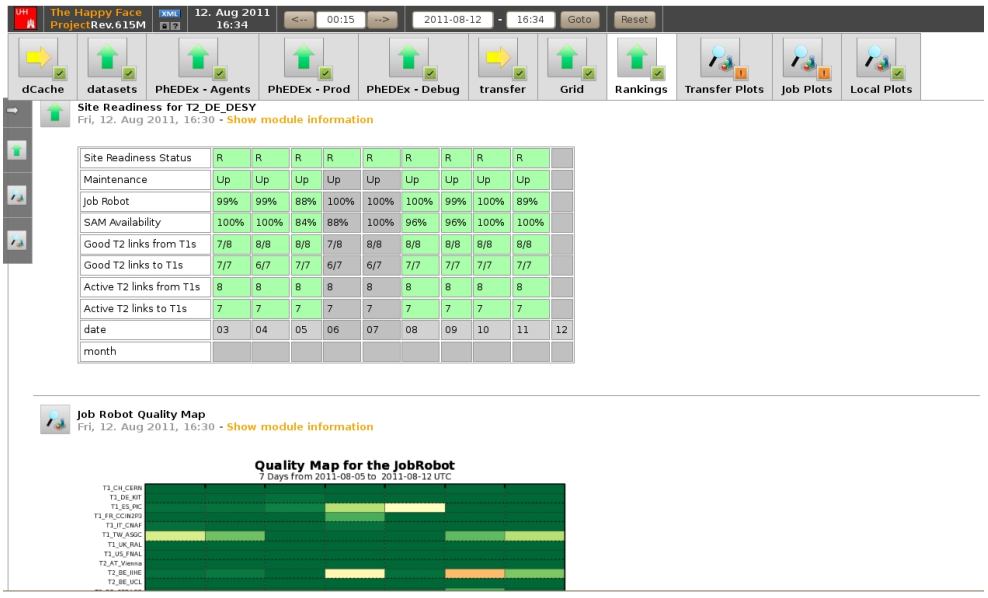


Figure 4.3: Screenshot of the website of the HappyFace instance at DESY.

### 4.4.1 CMS modules for the HappyFace Project

Several groups from CMS and ATLAS were involved in developing the HappyFace Project. Hence, the core framework providing the basic functionalities is independent from experiment related differences. The external monitoring sources, however, are tailored to the specific needs of the experiments. This specialization is taken care of by the modules. A module communicates to the framework through well-defined interfaces, and is executed in a multi-threaded environment controlled by the core. They are set up by an individual configuration file, which is also used to generate global information about the module displayed at the website. Each module has to fulfill several tasks:

- **Testing Procedure**: The module has to define and execute the testing procedure during collecting and processing the data.
- **Rating**: It has to evaluate the monitoring information.
- **Database Write**: It stores all relevant data as well as the resulting rate in the database.
- **Database Read Out**: Finally, it defines a PHP fragment for dynamical HTML output.

The status evaluated by the module is visualized in two ways. First, a status icon provided by the core marks the module at all places it is cited by the website. Second, the data leading to the decision is color coded. Usually green is used for *everything is fine*, yellow for *warning*, and red for *critical* status.

In the context of this work, several modules for DESY Tier 2 operation surveillance have been developed. They focus on the transfer of datasets, their usage of the experiment, their completeness, and on the performance of the site from CMS side of view. Some of these modules are also used at other sites like Aachen Tier 2 [79] and even Karlsruhe Tier 1 (KIT) [80]. They are described in the following in detail.

### PhEDEx Agents

The complex task of transferring a dataset from one site to another is carried out by PhEDEx agents representing simple processes. Each site runs a server, where the agents dedicated to this site are hosted. PhEDEx provides a website, where these agents can be monitored centrally. It also provides an XML service, where the actual information about the agents is reported. This service is read out by this module. The data used include the name and label of the agents, its status if critical or not, the time of its last report, its host and directory, and finally the version of the PhEDEx instance to which it belongs to. The information displayed is divided in two parts: the name, label, time of last report, and status is directly shown on the website for a fast overview, the other data is hidden behind a mask.
The rating is done on basis of the time of the last report. The module reports a warning (critical) state if the last report is older than one (two) hour. These timescales are the default values and are easy to configure to the specific needs of a site. It is also possible to exclude certain agents from the tests.

### Dataset Transfer

Even if the PhEDEx agents are up and running, the transfer of datasets remains error-prone. It depends not only on PhEDEx itself, but also on the configuration and load of the storage systems on both sites, the network connectivity, the transfer time, and on several other aspects. Hence, an additional monitoring of data transfers is mandatory. PhEDEx provides information about transfer errors also in an XML format, which is used by the "Dataset Transfer" module. Its state is evaluated from a number of transfer errors that occurred in the last 24 hours, but only if the number of errors exceeds a configurable amplitude (default is 10). The status depends then on the configurable fraction of errors caused by a specific site. For example, the warning state might be reached if the fraction of site errors exceeds 5% and critical state might be reached at 10%. In addition, warning and critical state can also be defined for errors caused by other sites.

### Dataset Usage by Physics Groups

In CMS, "Physics Groups" are formed by users of the same physics interest, e.g. "top-physics" or "supersymmetry". These Physics Groups can claim a certain size of storage at

dedicated sites. The Tier 2 at DESY for instance, provides 100 TB of disc space currently[5] for each of the groups "top-physics", "QCD-physics", "jets and missing $E_T$-physics", and "forward-physics". To keep track of the used space, each of the requested datasets is assigned to one group, either a Physics Group, an administrative group or the "local" group.
With the "Dataset Usage" module, for each group present at a site, the resident data and files, as well as the subscribed data and files are displayed. For each group, a warning appears, if the amount of resident data is smaller than the amount of requested data. The error state is reached, if a group uses more than its dedicated amount of storage. Instead of getting an overall storage amount assigned, a group can also have an individual storage threshold. E.g. if a site wishes to give the "AnalysisOps" group more space than the official one requested, this can be defined in the config file.

### Most and Least Used Datasets

This module can either read out the most or least used dataset from Dashboard via the XML download. The number of datasets is configurable and is set to 10 by default. It provides information about the name of the datasets, the number of jobs run in a certain period of time and the corresponding number of users, and also the success rate of these jobs. It can be useful for a site administrator to know which dataset are heavily used, or seldomly touched, in order to know which datasets could be removed and which are better to be kept. However, as the number of jobs run on a dataset itself is neither critical nor good, no evaluation takes place. The displayed datasets are marked in blue to indicate this.

### Incomplete Block Replica

The smallest unit in a dataset is a file. These files are combined to blocks, and several blocks form a dataset. To find out if a full dataset is stored at a site, PhEDEx checks its completeness at block level and makes a list of incomplete blocks available via XML. The "Incomplete Block Replica" module displays the dataset name, the block name, the nominal number of block files and their size, and the resident block files and size at a site, and also the group that requested the dataset. However, PhEDEx can not differentiate between a block that is incomplete because it is broken, and a block that is incomplete because it is in the progress of transfer. Hence, this module does not rate its status, and the blocks are displayed in blue.

### Link Status

Another important component of a site is the state of the links to other sites. PhEDEx provides information about the links from one site to other sites, including the name of

[5]The concrete number of storage changes with time as the amount of collected data depends on the running time of LHC.

the sites the link points to, the state, and the last update of the source and destination site. This module displays all existing links to or from one site to other sites, with their status color coded: green for "OK", red for "down", gray for "excluded", and lilac for "deactivated". The determination of the overall module state depends on the number of links "down", but also on the type of the site the link is connecting with. For example, a Tier 2 site might want to see a warning if one or more links to other Tier 2 sites are "down", and a critical status, if one or more links to a Tier 1 center do not work. In addition, it is possible to exclude individual sites or site types from status computation, as well as include individual sites in the list of sites that cause critical errors if not linked.

**Site Readiness**

The Site Readiness is used by CMS to determine if a site fulfills its duties from the CMS point of view. Thus, it is important for a site to know how it is rated in this scheme. The information is provided on a HTML website, which is parsed by this module[6]. It is assembled by different components, namely the number and status of links, the SAM availability, the number of successful JobRobot jobs, the maintenance status, and the week day[7]. The Site Readiness is already an overall rating, hence it is used directly by the module.

In Summary, seven modules for the meta-monitoring suite HappyFace have been developed, relating to the operation of a CMS site. Their usage led to a greatly reduced amount of time needed to monitor the DESY Tier 2, as all relevant data are collected automatically by the HappyFace instance. As a result, less manpower is needed, i.e. the system of shifts was dropped, without reducing performance of the site, which has been at 98% availability for the last year.

[6]Don't do that at home.

[7]For Tier 2 sites, uptime is only required for week days. This is not true for Tier 1 sites.

# Chapter 5

# Event Simulation

Event simulation (also: event generation, Monte-Carlo events (MC)) is a method of modeling physics processes after the current theoretical descriptions. It is divided in several steps. First, the proton-proton collision and the resulting particles from the hard process are simulated. Depending on the MC generator, the number of possible final particles can vary. The second step is the calculation of the parton showers, originating from initial- or final-state radiation of gluons due to higher-order QCD processes. Third, the hadronization of colored particles into color-neutral, composed hadrons is computed. All particles present after these three steps are referred to as "generator level" particles. Several different event generators are available, from which only few where relevant in this thesis.
Pythia [81] is the "working horse" of particle physics. It is a multi-purpose event generator, which can be used as stand-alone package. All steps listed above can be performed by it, but it provides also the possibility to read in the hard process results from other generators, and pass them to the parton shower and hadronization. A double counting of radiation calculated from both the matrix element generator and the parton shower can appear. To avoid this, a matching of the partons has to be done.
MadGraph [82] is a matrix element generator, simulating up to $2 \rightarrow 9$ particles in the hard process. The result can be read in by Pythia to perform the showering and hadronization steps.
ISAJET [83] is used to calculate the matrix elements of supersymmetric events. The results are again handled over to Pythia.
In addition, a package dedicated to the tau decay simulation, named TAUOLA [84], was used.
Finally, all stable generated particles are given to a detector simulation. For CMS, this simulation is based on Geant4 [85]. The standard CMS reconstruction algorithms are then used on the simulated detector response, and the resulting particles are referred to as "reconstruction level" particles.
In case of the cMSSM scans, the detector simulation is not done with Geant4, but with CMS Fast Simulation [86]. Fast Simulation is a simplified detector simulation less computational intensive than Geant4, and is validated with Geant4 output and test beam data.

## 5.1 Used Simulated Events

As the Standard Model background expectation was derived on data, most of the listed samples had no direct impact on the estimate. They were, however, used for testing the methods and compared to data for illustration purposes. Their cross sections were derived on tree-level (leading order, LO), on next-to-leading order (NLO), or next-to-next-to-leading order (NNLO). Except for the QCD calculations, MadGraph was used as event generator for the Standard Model processes (see table 5.1). For the cMSSM scans, the cross section at NLO were computed with Prospino [87].
The QCD simulation is a so-called "flat" event set, where the momentum transfer in the hard process is not simulated according to Feynman calculations. Instead, a still falling, but much less steeper distribution is chosen. This leads to higher statistics in the region with high jet activity and less statistics in regions with small activity, and the event set must not only be weighted according to its cross section, but also each event has to be individually weighted according to the momentum transfer present in the event. Hence, very large weights can be present in this event set.
The simulation of the production of $W$ bosons in association with jets ($W$ plus jets) is the only simulated event set directly influencing the background estimate. It was used to derive several weighting factors for data events. With 2010 data taking, it was shown that the description of data by simulation according to tau reconstruction was accurate (see section 6.3.5).
For di-boson production, only $WW$-events were taken into account. While $WW$-events have the largest cross section of the di-boson events, in principle, also $ZZ$ -events, especially $ZZ \to \nu\nu\tau\tau$, and $WZ$-events are part of the background. However, simulation predicts $WW$ to be the source of only $\sim 1\%$ of the background in the final selection. The other di-boson background contributions are of the same order, and are thus left out for simplicity.
The Standard Model prediction was compared to two different SUSY benchmarks from the cMSSM (LM2 and LM13, see section 2.2.1). In addition, limits were set in the cMSSM model. For this, a scan consisting of different benchmark points ranging from $m_0 = 220 \ldots 3000$ GeV and $m_{1/2} = 100 \ldots 1000$ GeV in 20 GeV steps, and generated with $\tan\beta = 40$, $A_0 = -500$, and $\text{sign}\mu = +$ was used (see also table 5.1).

| Process | Generator | Order | Cross section [pb] | #events |
|---|---|---|---|---|
| QCD | Pythia | LO | 10960800 | $2.21310^{10}$ |
| $W \to l\nu$ | MadGraph | NNLO | 31314 | 81352581 |
| $Z \to ll$ + Jets ($m_{ll} > 50$ GeV) | MadGraph | NNLO | 3048 | 36277961 |
| $Z \to \nu\nu$ + Jets ($H_T > 200$ GeV) | MadGraph | LO | 33 | 3067017 |
| $WW \to l\nu l\nu$ + Jets | MadGraph | NLO | 43 | 1197558 |
| $t\bar{t}$ | MadGraph | NLO | 165 | 3701947 |
| LM2 | Pythia | LO | 0.6 | 77000 |
| LM13 | Pythia | LO | 6.9 | 11000 |
| cMSSM scan | ISAJET | NLO | | 10000 each |

Table 5.1: Summary of the simulated processes and the generators used. Also shown is the corresponding cross section for proton-proton collisions at $\sqrt{s} = 7$ TeV, the order at it is calculated, and the simulated number of events. The cMSSM scan consists of different benchmark points ranging from $m_0 = 220 \ldots 3000$ GeV and $m_{1/2} = 100 \ldots 1000$ GeV in 20 GeV steps. The other variables were set to $\tan\beta = 40$, $A_0 = -500$, and $\text{sign}\mu = +$.

# Chapter 6

# Tau Reconstruction and Identification

## 6.1 The Tau Lepton

The Tau Lepton was discovered in 1975 at SLAC in the $e^+ + e^- \rightarrow e^\pm + \mu^\mp +$ missing energy channel[1][88][89]. With a mass of 1776.82 $\pm$ 0.16 MeV, it is the heaviest of the leptons, and also heavier than the lightest hadrons. Not only the leptonic decay branch $\tau \rightarrow \nu_\tau W^* \rightarrow \nu_\tau l \nu_l$ with $l$ = (electron, muon) is possible, but also the hadronic decay branch, where the virtual boson $W^*$ will decay into one or more charged and neutral hadrons. This branch shares a fraction of $\sim$ 65% of all decays. Most of the hadronic decays are so called "one-prong" decays, where only one charged hadron will be produced, or "three-prong" decays, with three charged hadrons. They can be accompanied by neutral pions, as listed in table 6.1. The decay products always include a neutrino, hence energy is lost to the measurement, and therefore the tau cannot be completely reconstructed. The hadronic decay products are reconstructed as a jet in the detector. To differentiate tau jets from ordinary jets produced by QCD or other processes, CMS developed several algorithms. All of them currently used are based on the so-called "particle-flow" event reconstruction.

## 6.2 Particle-Flow

The idea of particle-flow [90] event reconstruction is to identify all stable particles within the acceptance of the detector. All detector parts are used. With its excellent tracker and electromagnetic calorimeter, together with the high magnetic field, CMS is well suited for this task.
Even in an event with high-$P_T$ jets, most of the jet constituents will have low momentum. To obtain an efficient reconstruction of all these elements at reasonable low fake rate in a

[1] Martin Perl won the Nobel Price in 1995 for this discovery.

| Decay mode | Resonance | Mass [MeV] | BF(%) |
|---|---|---|---|
| $\tau^- \to h^-\nu_\tau$ | $\pi$ | 139.6 | 11.6 |
| $\tau^- \to h^-\pi^0\nu_\tau$ | $\rho$ | 770 | 26.0 |
| $\tau^- \to h^-\pi^0\pi^0\nu_\tau$ | $a_1$ | 1200 | 10.8 |
| $\tau^- \to h^-h^+h^-\nu_\tau$ | $a_1$ | 1200 | 9.8 |
| $\tau^- \to h^-h^+h^-\pi^0\nu_\tau$ | | | 4.8 |
| other hadronic modes | | | 1.7 |
| total | | | 64.8 |

Table 6.1: Hadronic tau decay modes into either one or three charged hadrons $h$ and potential $\pi^0$, and the corresponding branching fractions BF. Also shown are the intermediate resonances and their masses, which are used in some of the tau reconstruction algorithms.

high-density environment, the particle-flow algorithm is divided in several steps:

- **Iterative tracking**: Up to a momentum of several hundreds of GeV, the tracker has a superior resolution with respect to the hadronic calorimeter. In addition, it provides a direct direction measurement of the charged particle at its vertex, before the bending due to the magnetic field comes into play. Thus, the tracking efficiency must be close to 100%, but its fake rate must also be kept small. An iterative approach was chosen to archieve these goals. The first iteration of track finding starts with very tight criteria to supress the possibility of wrong identified tracks. At each following iteration, the critereas are loosenend, and the hits used by the foregoing step are removed. In the end, particles with a $P_T$ as small as 150 MeV can be reconstructed with a fake rate at the order of one percent.

- **Calorimeter Clustering**: The next part is the calorimeter clustering. Its purpose is to reconstruct neutral particles like photons or neutral hadrons, and separate their energy deposits from charged particles. In addition, electrons and their accompanying bremsstrahlung photons are to be identified. Lastly, the calorimeter measurement should also support the measurement of charged hadrons, in case of a low-quality or high-energy track. The algorithm starts with defining "cluster seeds", build out of calorimeter cells exceeding a certain threshold. Then, surrounding cells with sufficient energy are added, forming "topological clusters". A calorimeter cell can belong to more than one cluster, and its energy is then divided according to its distance to the corresponding seeds.

- **Linking**: Generally, a given particle will leave traces in more than one subdetector. The linking step combines any two particle-flow elements reconstructed beforehand. This includes linking tracks to calorimeter cells, finding bremsstrahlung photons at the trajectory of a track, combining clusters of different calorimeter detectors, and matching a track to entries in the muon systems. For each link, a quality parameter

is defined, e.g. for muons the $\chi^2$ of the fit.

- **Particle Identification**: After the linking, particle identification takes place. After the identification, all components used in building up the particle are removed from the list of linked blocks. First, the muons as combined elements of tracker and muon chamber hits ("global muon") are tagged. Then, electrons and the corresponding bremsstrahlung photons are dealt with. Tighter track criteria are applied for identifying the remaining charged hadrons, photons, and neutral hadrons, which are finally added to the list of particle-flow particles.

Once all linked detector elements are identified without leaving ambiguities, all resulting particles are handed over to the jet reconstruction algorithms.

## 6.3 Tau Identification

The decay products of a hadronic tau, the charged and neutral pions, are reconstructed by the particle-flow algorithm. To identify them as originating from a tau, and not being part of an ordinary jet, is more difficult. Jets are used as a starting point in tau reconstruction. In the following, algorithms to tag a jet as tau-jet used at CMS are presented.

### 6.3.1 Shrinking Cone Algorithm

In a hadronic tau decay, very few particles are produced in comparison to an ordinary quark or gluon jet [91]. These particles are usually grouped around the $P_T$-leading charged hadron ("leading pion") with a small distance to it. This is an effect of the tau Lorentz boost, which leads to narrow distributed decay products. The Shrinking Cone algorithm comprises of two cones (see figure 6.1). The first, narrow cone ("signal cone") is centered around the leading pion, which is required to exceed a certain $P_T$-threshold, and has to include all particles produced by the tau. The predecessor of the Shrinking Cone, the Fixed Cone algorithm, had the opening angle of the cone fixed to $\Delta R_{sig}(\eta, \phi) = 0.07$. The size of the signal cone depends on transverse energy of the tau-jet, and is defined to $\Delta R_{sig} = 5/E_T$, with a minimal size of $\Delta R_{sig} = 0.07$ and a maximal size of $\Delta R_{sig} = 0.15$ for charged particles, and a fixed cone of the size $\Delta R_{sig} = 0.15$ for photon candidates [92]. The larger cone size at small energies allows a better reconstruction of the three-prong decays, which have usually more particles in the jet than the one-prong decays.
The second cone ("isolation cone") is defined around the signal cone, with a typical size of $\Delta R_{iso} = 0.45$. In the isolation cone, no particle above a certain $P_T$-threshold is allowed.

### 6.3.2 Tau Neural Classifier

The Tau Neural Classifier (TaNC) [93] is not a standalone algorithm, but is combined with the Shrinking Cone. It comprises of five neural networks for each of the dominating decay modes, working on the already tagged tau-jets by the Shrinking Cone. The TaNC

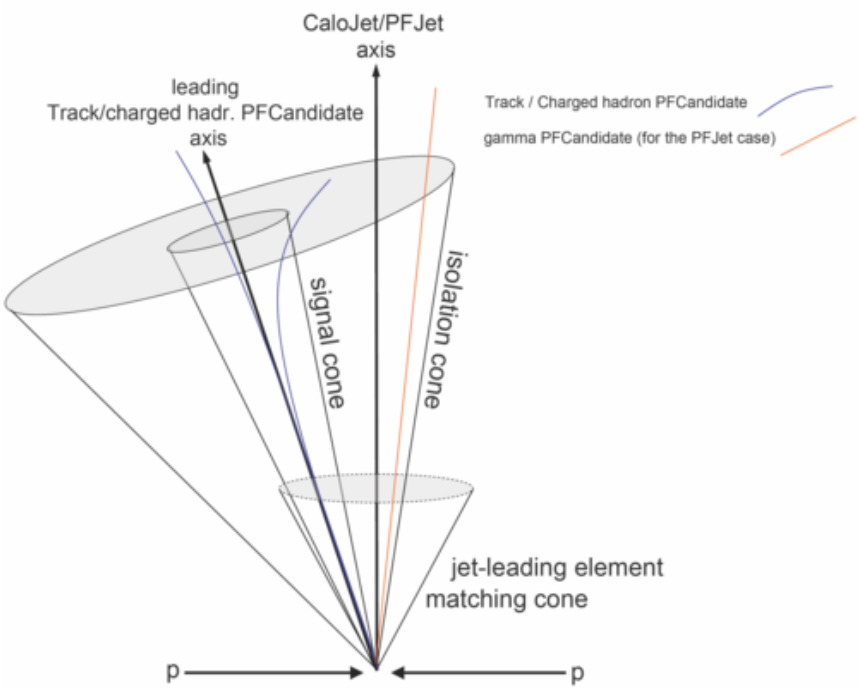


Figure 6.1: Schematic view of the Shrinking Cone algorithm. A signal cone is laid around the leading particle-flow candidates, and an isolation cone is defined around the first cone. The direction of the Shrinking Cone tau-jet defined by the direction of the leading pion is not necessarily the same as the direction of the full jet [92].

combines the particle-flow candidate photons in the signal cone to the pair invariant mass most compatible to the $\pi^0$ mass. In addition, single photons with an energy residing in this invariant mass window as possible merged photon pairs are also considered. Once the number of neutral pions and thus the decay mode is identified, the tau candidate is given to the corresponding neural network. The input parameters of the neural network are chosen to parametrize the intermediate resonance the decay products are going through (see table 6.1). The networks are trained on simulated $Z \rightarrow \tau\tau$ as signal and simulated QCD multijet as background sample. Several working points are defined, which are based on the average fake rate per QCD jet.

### 6.3.3 Hadron plus Strips

The Hadron plus Strips (HPS) algorithm is a cut-based algorithm focusing on the reconstruction of neutral pions. A strip-shaped area of $\Delta\eta = 0.05$ and $\Delta\phi = 0.2$ is centered around the electromagnetic particle with the highest $P_T$ in the jet. If other electromagnetic particles within the strip are found, the one with the highest $P_T$ of the additional particles is combined with the first particle, and the center of the strip is recalibrated to the center

of the combined object. This procedure is repeated until no further particle inwards the strip is found. The resulting strips are considered as being neutral pion candidates and are combined with the charged hadrons in the jet. Except for $\tau \to h^- h^+ h^- \pi^0 \nu_\tau$, all of the dominating decay modes are considered. All particles found are required to be in a narrow cone of size $\Delta R = 2.8\ \text{GeV}/P_T^\tau$, and the direction of the leading charged hadron has to be in a $\Delta R > 0.1$ distance to the direction of the jet. The invariant mass of the particles found has to be in the region of the corresponding intermediate resonance (see table 6.1). In addition, an isolation requirement is applied, which defines several working points. Within the isolation cone, only charged particles originating from the primary vertex are taken into account. A correction for neutral Pile-Up particles in the cone has been applied. The thresholds for particles in the isolation area are[2]:

- **Very Loose Isolation**: Veto taus with charged hadrons with $P_T > 1.5$ GeV and photon candidates with $P_T > 2$ GeV within $\Delta R < 0.3$.
- **Loose Isolation**: Veto taus with charged hadrons with $P_T > 1$ GeV and photon candidates with $P_T > 1.5$ GeV within $\Delta R < 0.5$.
- **Medium Isolation**: Veto taus with charged hadrons with $P_T > 0.8$ GeV and photon candidates with $P_T > 0.8$ GeV within $\Delta R < 0.5$.
- **Tight Isolation**: Veto taus with charged hadrons with $P_T > 0.5$ GeV and photon candidates with $P_T > 0.5$ GeV within $\Delta R < 0.5$.

### 6.3.4 Against Lepton Discriminators

Not only jets, but also electrons and muons can be misidentified as taus. Hence, a set of discriminators are defined to identify and veto light leptons in the tau-finding process.

- **Against Muon Discriminator**: The tau candidate is dropped, if the track of the leading hadron is matched to muon chamber hits (loose variant), or to a reconstructed muon (tight variant), either to a tracker only muon, or a global muon.
- **Against Electron Discriminator**: To identify electrons, a fast multivariate analysis of tracker and calorimeter information is performed. In addition, the discriminator makes use of the fact that an electron will deposit its energy mainly in the ECAL, while a pion leaves also some energy in the HCAL.

### 6.3.5 Reconstruction Efficiency and Fake Rates

A detailed analysis of the reconstruction efficiency and the fake rate has been performed by CMS on 2010 data [93]. The efficiency has been studied on a $Z \to \tau\tau \to \mu\tau_h$ sample,

[2]There is also the possibility to define the isolation as a sum over the energy of all particles within the isolation area in contrast to the energy of the individual particles. This was not used here.

were the muon was used as tag, and a jet with the leading track having more than 5 GeV transverse momentum as probe. Several kinematic cuts were used to suppress contributions other than the $Z$-resonance. Both the $\mu$-jet invariant mass distributions of the samples where the jet passes the tau identification as well as where the jet fails the identification were fitted using simulated events of background and signal. In case the tau is identified, the tau-jet is used for computing the invariant mass, else the jet is used. The efficiency is then defined as

$$\epsilon = N_{\text{pass}}^{Z\to\tau\tau}/(N_{\text{pass}}^{Z\to\tau\tau} + N_{\text{fail}}^{Z\to\tau\tau}). \tag{6.1}$$

The results for different algorithms and working points can be found in table 6.2. Note that both the cut on the transverse momentum of the jet as well as the clean $Z \to \tau\tau$ environment produces a biased sample, which leads to an identification efficiency higher than for an inclusive sample. The efficiency is expected to be dependent on $\mathrm{P_T}$ and $\eta$ of the taus, and also on the individual analysis. For and inclusive $Z \to \tau\tau$ sample, the expected efficiencies are listed in table 6.3.

The aim of this study was to determine correction factors Data/MC and their uncertainty. With this method, the latter are of 20-30%. To decrease them further, two additional approaches have been used in [94]. The first was a simulatious fit of several decay channels of the $Z \to \tau\tau$ events ("combined fit"). The second was a comparison of the $\mu\tau_{had}$ and $e\tau_{had}$ channels to the precisely measured $Z \to ee$ and $Z \to \mu\mu$ production (also shown in table 6.2). All studies show a data to simulation ratio compatible to unity.

The quality of the tau energy scale simulation was measured in obtaining templates by varying the scale simultaneously in background an signal simulation and fitting the templates to the data. It has been found that the tau energy scale is close to unity, and has an uncertainty of 3%.

The misidentification rate ("fake rate") of (quark or gluon) jets has been measured in QCD multijet events, in a QCD $\mu$-enriched sample, as well as in $W$-boson events. Figure 6.2 shows the $\mathrm{P_T}$ dependency for the fake rate of jets for these different samples for data (filled markers) and simulation (open markers). Table 6.4 gives the expected integrated fake rates per jet for the different algorithms in these three samples in percent. In addition, the Data/MC ratio is shown. All in all, there is a good agreement of data to simulation, which is consistent for different data samples. The uncertainty is roughly 20%.

| Algorithm | Fit data | Expected MC | DATA/MC |
|---|---|---|---|
| HPS "loose" | $0.70 \pm 0.15$ | 0.70 | $1.00 \pm 0.24$ |
| HPS "medium" | $0.53 \pm 0.13$ | 0.53 | $1.01 \pm 0.26$ |
| HPS "tight" | $0.33 \pm 0.08$ | 0.36 | $0.93 \pm 0.25$ |
| TaNC "loose" | $0.76 \pm 0.20$ | 0.72 | $1.06 \pm 0.30$ |
| TaNC "medium" | $0.63 \pm 0.17$ | 0.66 | $0.96 \pm 0.27$ |
| TaNC "tight" | $0.55 \pm 0.15$ | 0.55 | $1.00 \pm 0.28$ |
| HPS "loose" | combined fit [94] | | $0.94 \pm 0.09$ |
| HPS "loose" | $\tau\tau$ to $\mu\mu, ee$ fit [94] | | $0.96 \pm 0.07$ |

Table 6.2: Efficiency for hadronic tau decays to pass TaNC and HPS tau identification criteria measured by fitting the $Z \to \tau^+\tau^-$ signal contribution.The errors of the fit represent statistical uncertainties. The last column represents the data to MC correction factors and their full uncertainties including statistical and systematic components. Data to Simulation (MC) ratios for the tau reconstruction efficiency measured using fits to the measured $Z$ production cross sections as described in [94] are also shown. From [93].

| Algorithm | TaNC | | | HPS | | |
|---|---|---|---|---|---|---|
| | "loose" | "medium" | "tight" | "loose" | "medium" | "tight" |
| Efficiency ($P_T^{\tau had} > 15$ GeV) | 53.6% | 43.1% | 30.4% | 45.9% | 33.8% | 22.9% |
| Efficiency ($P_T^{\tau had} > 20$ GeV) | 57.8% | 47.9% | 35.6% | 49.9% | 36.5% | 24.6% |

Table 6.3: Expected efficiency for hadronic tau decays to pass TaNC and HPS tau identification criteria estimated using simulated $Z \to \tau\tau$ events, as been studied in [93].

| Algorithm | QCD | | QCD$\mu$ | | W + jets | |
|---|---|---|---|---|---|---|
| | MC(%) | Data/MC | MC(%) | Data/MC | MC(%) | Data/MC |
| HPS "loose" | 1.0 | $1.00 \pm 0.04$ | 1.0 | $1.07 \pm 0.01$ | 1.5 | $0.99 \pm 0.04$ |
| HPS "medium" | 0.4 | $1.02 \pm 0.06$ | 0.4 | $1.05 \pm 0.02$ | 0.6 | $1.04 \pm 0.06$ |
| HPS "tight" | 0.2 | $0.94 \pm 0.09$ | 0.2 | $1.06 \pm 0.02$ | 0.3 | $1.08 \pm 0.09$ |
| TaNC "loose" | 2.1 | $1.05 \pm 0.04$ | 1.9 | $1.12 \pm 0.01$ | 3.0 | $1.02 \pm 0.05$ |
| TaNC "medium" | 1.3 | $1.05 \pm 0.05$ | 0.9 | $1.08 \pm 0.02$ | 1.6 | $0.98 \pm 0.07$ |
| TaNC "tight" | 0.5 | $0.98 \pm 0.07$ | 0.4 | $1.06 \pm 0.02$ | 0.8 | $0.95 \pm 0.09$ |

Table 6.4: Data/MC correction factors of the fake rate of jets for different working points of the HPS and TaNC reconstruction algorithms in different samples. Also shown are the expected fake rates per jet in percent. From [93].

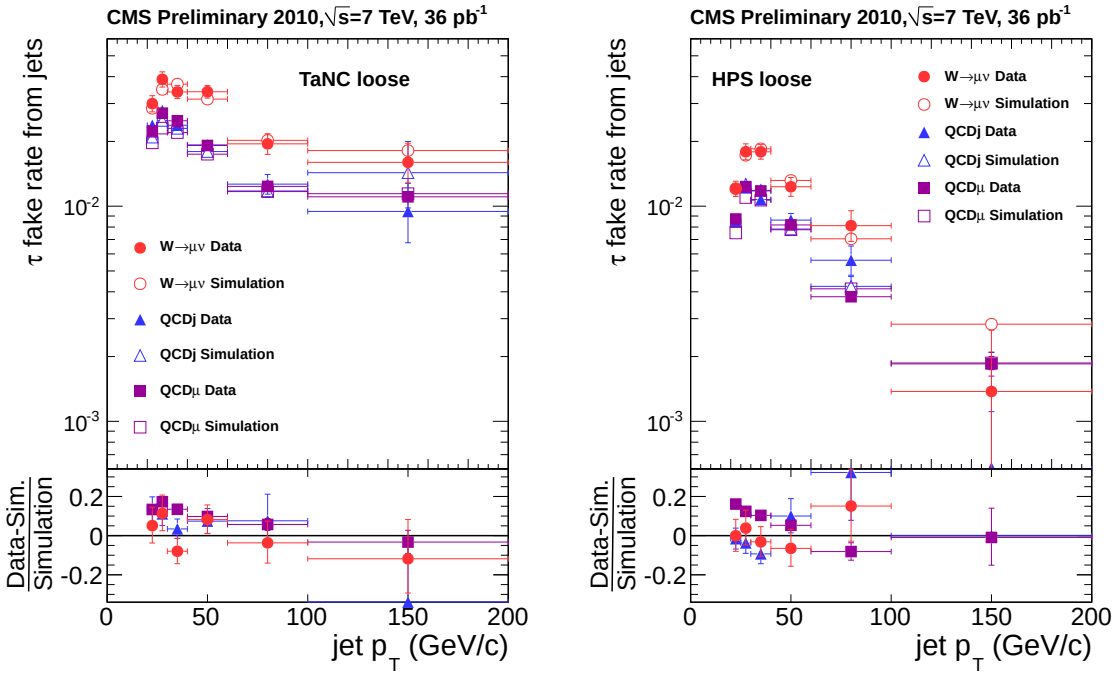


Figure 6.2: Probabilities of quark and gluon jets to pass the "loose" working points of the TaNC (left) and HPS (right) algorithms as a function of jet $P_T$ for QCD, QCD $\mu$-enriched and $W$ type events [93] for data (filled marker) and simulation (open marker).

# Chapter 7

# Event Selection

Due to cosmological arguments, in the cMSSM parameter space, the area near the co-annihilation region (see 2.2.1) is the region of most interest for searches with taus. With decreasing $m_0$, the stau mass becomes small and the stau is the NLSP, until the stau mass falls below the LSP mass. Because of this configuration, a large fraction of decay chains will include a decay via a stau. Decays into a smuon or an selectron is less frequent. In addition, light leptons coming from taus can be below the trigger threshold, as the momentum spectrum of the taus themselves is usually soft. The co-annihilation region is also a realm where high missing transverse momentum and hadronic activity is likely.
Note that this analysis has a similar event signature like fully hadronic searches. Due to the additional presence of a (hadronic) tau[1], the background composition may be different, and the requirements on event content like the missing transverse energy can be lowered. In object definition, this analysis follows closely [95].
In this thesis, 5 fb$^{-1}$ of data from the 2011 run at a center-of-mass energy of $\sqrt{s} = 7$ TeV was analyzed. The used dataset are listed in table 7.1 for completeness.

| Dataset name | type | run range | luminosity [pb$^{-1}$] |
|---|---|---|---|
| May10 | ReReco | 160431-163869 | 216.1 |
| V4 | Prompt | 165088-167913 | 957.2 |
| Aug05 | ReReco | 170826-172619 | 390.7 |
| V6 | Prompt | 172620-173692 | 708.1 |
| RunB | Prompt | 175860-178803 | 2720.0 |
| Sum | | | 4992.1 |

Table 7.1: The datasets and the corresponding run ranges and luminosities, as used in this study. In addition, it is listed whether the dataset was prompt reconstructed or already re-reconstructed (see section 4.1).

[1] If not otherwise noted, a "tau" always refers to an hadronically decaying tau in the following.

## 7.1 Object Definition

The Objects used for the selection and the background predictions are defined as follows:

- **Muons**: Muons are particle-flow candidates which satisfy the condition of being global muons (see 6.2), and also are isolated in $\Delta R = \sqrt{\eta^2 + \phi^2} < 0.3$ against other particles. The isolation is defined as the sum over the $P_T$ of all particle-flow candidates found in the isolation area, relative to the transverse momentum of the lepton. This value must not exceed 0.2. The normalized $\chi^2$ of the fit that links the hits of the muon in the tracker with the hits in the muon chambers has to be less than 10. In addition, muons are required to be central ($|\eta| < 2.4$) and have a transverse momentum of at least 10 GeV.

- **Electrons**: The used electrons are also identified by the particle-flow algorithm and isolated in $\Delta R < 0.3$ against other particles. This isolation is defined as for the muons. The electrons are restricted to $|\eta| < 2.5$ and $P_T > 10$ GeV has to be valid. The transition region $1.444 < |\eta| < 1.566$ has not been considered.

- **Jets**: Particle-flow jets are build up from a list of all resulting particle-flow objects. To avoid double counting, muons and electrons defined as above where removed from this list. In this list, not only particles produced by one hard proton-proton collision are present, but also particles coming from additional, softer collisions (Pile-Up). The charged component of this Pile-Up can be identified, as their tracks do not originate in the vertices of the hard process. Thus, charged particles identified as Pile-Up are subtracted from the list of input particles, leaving the jet only with a contamination of neutral Pile-Up particles.
  Due to detector resolution and rare effects like dead calorimeter cells, and physics effects like the decay of heavy flavor hadrons producing a neutrino, the measured energy of the jet is not the same as the energy of the hadrons forming the jet [96]. To account for this, jet energy corrections depending on the pseudorapidity and transverse momentum of the jet are applied.
  Each hadronic tau is also found in the list of jets. A cross cleaning of identified taus against jets has not been performed. Note that this cleaning would in principle improve the resolution of composite objects like $H_T$ and $\not{H}_T$ as the tau energy scale is close unity (see section 6.3.5), and thus, the corresponding jet will be overcorrected to a small amount.

- $H_T$: The transverse hadronic momentum ($H_T$) present in the event is an estimator of the overall energy scale of the event. In many SUSY scenarios, the decay chains can be long, producing many particles in the event. As the main production channel at a proton-proton collider is via the strong force, a lot of hadronic activity is expected. $H_T$ is defined as the scalar sum over transverse momentum of all jets with $P_T > 50$ GeV and $|\eta| < 2.5$:

$$H_T = \sum P_T^{jet} \tag{7.1}$$

The jet $P_T$-thresholds are chosen such that the influence of Pile-Up and soft QCD radiation is suppressed.

- $\not{H}_T$: In the Standard Model, the missing transverse momentum ($\not{H}_T$) can be caused by a neutrino or by missed or mis-measured objects, mainly jets. In SUSY, the two undetectable LSPs will cause missing energy in each event[2]. This $\not{H}_T$ can be large, if the LSP mass is small, which is often the case. Hence, $\not{H}_T$ is used as a discriminator against Standard Model background. It is defined as the transverse component of the negative vectorial sum over the momentum of all jets exceeding $P_T > 30$ GeV and in a pseudorapidity range of $|\eta| < 5$:

$$\not{H}_T = |-\sum \vec{P}_T^{\,jet}| \tag{7.2}$$

  Although particles coming from Pile-Up in an event are expected to produce no missing momentum overall, this is not true in practice due to measurement loss of particles out of acceptance. To avoid this to the most possible extent, the momentum threshold of the jets is chosen to be lower as for the definition of $H_T$, and the pseudorapidity region is broadened in order to collect as many jets as possible for an accurate description of $\not{H}_T$.

- **Taus**: The used taus are identified with the HPS algorithm (see 6.3). The working point Loose Isolation is used. The Discriminators "Against Electron Tight" and "Against Muon Tight" are applied. A tau has to have at least 15 GeV of transverse momentum and pseudorapidity must be in the range of $|\eta| < 2.1$.

## 7.2 Trigger

While there are dedicated single-tau trigger at CMS, the online momentum threshold is already at $\mathcal{O}(40$ GeV) at HLT. To avoid imposing such a high transverse momentum cut on taus in order to keep sensitivity in regions where their $P_T$ is usually small, instead a trigger on missing momentum was chosen. Its online threshold is 150 GeV at HLT. A study on the offline efficiency was done by [97] by choosing $t\bar{t}$ events, which have a similar $P_T$ distribution and activity as SUSY events. Following this study, the cut on the missing transverse momentum was set to $\not{H}_T > 250$ GeV. The efficiency at the plateau was found to be $98.2 \pm 2.5\%$.

## 7.3 Event Cleaning

Due to detector and machine effects, various sources of fake $\not{H}_T$ can arise. Several of them were identified and investigated during data taking in 2010 [98]. For the search for SUSY

[2] As said, R-Parity conserving Supersymmetry with an electromagnetically and strongly uncharged LSP is assumed.

in the all-hadronic channel [95], different event filters were developed, and are also applied here:

- **Beam Halo**: Collisions of beam particles outside the interaction point can produce muons entering the detector. These muons will be a source of $\not{H}_T$. The Cathode Strip Chambers are used to tag events where a muon not coming from the interaction point is found. These events are then vetoed.

- **Anomalous Signals**: Anomalous signals in the calorimeters are produced by particles hitting the readout system of the calorimeter cells. Once such a hit is identified, it is excluded from the reconstruction of higher level physics objects such as jets or $\not{H}_T$. If a large number of channels is effected, the event is vetoed.

- **HBHE Noise**: Another type of anomalous signals in the HCAL barrel and endcap is due to instrumental effects in the photodiodes which read out the scintillator light. This noise is either caused by ion feedback inside the photodiodes, electrical discharges or noise in the readout system of the photodiodes. It can be identified by the shape of the signal, and events containing this noise are rejected.

- **Good Primary Vertex**: The primary vertex is required to be not more than 24 cm away from the nominal interaction point in the beam direction, and not more than 2 cm in the radial direction. In addition, it has to have more than 4 degrees of freedom, which correspond to a weighted sum of tracks.

- **Beam Scraping**: Beam scraping is the effect of the beam hitting a part of the apparatus like a collimator. To remove events contaminated by particles produced by beam scraping, for each event kept, at least 10 tracks are required, with a minimum of 25% fulfilling high quality criteria.

- **Inconsistent Muon Filter**: In particle flow reconstruction, all particles, including muons, are used for jet reconstruction. Thus, a misidentified muon will cause fake missing momentum. The inconsistent muon filter removes all events where a muon is found for which the momentum measurement of the tracker alone and the momentum measurement of the combined tracker and muon system differs more than 10%.

- **Tracking Failure Filter**: In a small number of events, the tracking algorithm can fail due to a too large number of clusters. It can also happen, that the collision did not take place at the nominal interaction point. These events can cause entries in the $\not{H}_T$ tails, and are removed by a cut on the ratio between the number of tracks from the primary vertex and the sum of all transverse energy of the jets in the event.

- **"Ring of Fire"**: In the ECAL endcaps, this type of noise correlated to noise in the muon chambers, has been observed. Events affected by this are removed by a cut on the maximum number of ECAL hits in the endcap.

- **Particle Based Noise Rejection**: To suppress further noise, the particle based noise rejection was developed. An event containing a jet with a neutral hadron fraction or a photon fraction greater than 90% is rejected.

- **Dead ECAL filter**: In reconstruction, several ECAL crystals are masked, either because they are known to be noisy, or they correspond to Very Front End (VFE) cards or Front End (FE) cards with no data link. The number of channels ignored is about $\sim 1\%$. This can lead to significant contribution to the missing transverse momentum, if a jet includes one of these dead cells. To identify events with such a problematic $\not{H}_T$ contribution, either the trigger information or the surrounding cells are used to estimate the lost energy. If this energy exceeds a certain threshold, the event is rejected.

## 7.4 Selection

This analysis focuses on the single-tau channel, while the di-tau channel and the combination of a tau with a light lepton in the events is covered in [99]. Hence, exactly one tau is required and a veto on light leptons (e,$\mu$) is applied.
Two Selections have been used in this study. The Base-Line selection was chosen for testing the background estimations and consists of the trigger threshold cut on the missing transverse momentum and a second cut on the transverse hadronic momentum in the event, $H_T$. Figure 7.1 shows the contributions of Standard Model processes to the transverse hadronic momentum after all but the $H_T$ cut applied. For comparison, two SUSY benchmark models are shown. In most of the Standard Model events, low $H_T$ dominates, while the SUSY events have a longer tail towards higher values. Hence, the cut was set to $H_T > 350$ GeV, suppressing most of the background. The Full selection defines the search region for new physics with one tau. As the measurement of both $H_T$ as well as $\not{H}_T$ enables further background suppression, the cuts are increased to $H_T > 600$ GeV and $\not{H}_T > 400$ GeV, respectively. Figure 7.2 shows both distributions after all cuts except on the variable shown (N-1 Plots). Table 7.2 summarizes all cuts for the given selections.
Table 7.3 displays the event yields for both selections as predicted by simulation, in comparison to data. Two SUSY benchmark scenarios (LM2 and LM13; see section 2.2.1) are also listed. The dominating process left is the associated production of $W$ and jets for both Base-Line and Full selection. Considerably smaller contributions are coming from $t\bar{t}$ and QCD events. It is striking that simulation is clearly overestimating the data. For both selection, this is of roughly the same amount, i.e. 50%. Note that the uncertainty on the simulated statistics is not small in the Full selection, and the prediction is less that two sigma away from the data yield. The fact that simulation does not predicts the number of events accurately is not a problem of this analysis, as the final background will be estimated from data. The simulation-to-data comparison is shown here for illustration only.
Control plots for various distributions after the Base-Line selection are shown in figure 7.3, 7.4, 7.5 and 7.6 in comparison with data.

In figure 7.3, the cut distributions of $H_T$ and $\not{H}_T$ are shown. It can be seen that SUSY events tend to produce larger values. For $H_T$, the main background $W$ plus Jets accumulates at lower values, while cuts on $\not{H}_T$ are known to suppress QCD events effectively. Note that distributions of $H_T$ expand even beyond 1 TeV, reaching almost 2 TeV. These tails are difficult to describe in simulation, especially for $\not{H}_T$, and are another reason for estimating the background with data-driven methods. The third distribution shown is the number of jets with $P_T > 30$ GeV. In SUSY events, on average more jets are produced than in Standard Model events. It can also be seen that, while in an inclusive $W$ plus jets sample usually few jets are produced, the high $H_T$ and $\not{H}_T$ cuts lead to an equalization with respect to $t\bar{t}$, and in case of five jets, $W$-boson events are still the dominating process. The fourth variable shown is the $\Delta\Phi$ between the $\not{H}_T$ and the tau. For QCD events, the angle is expected to be flat, as both the $\not{H}_T$ (coming from mis-measurement of one or more jets) and the (fake) tau are independent from each other. For $W$-boson events on the other hand, the $\not{H}_T$ is real, as it comes from the neutrino. Both tau and neutrino are produced in the $W$-boson decay. The $W$-boson tends to be boosted because of the high $H_T$ requirement. Thus, the $\Delta\Phi$ peaks at smaller values. Note that the description of data by simulation is worst in this region. For SUSY events, the tau is still somewhat aligned with the $\not{H}_T$, as it is produced in the same chain as the LSP. However, there is a second LSP present in the event, smearing out the missing transverse momentum, and thus, the distribution is more flat.

The figures 7.4 and 7.5 display kinematic distributions of the tau and the first three leading jets (in case of $P_T^{jet} > 30$ GeV). These objects are produced quite centrally, as expected for an high-$H_T$ sample. For the tau, the $P_T$ distribution peaks at low values for the Standard Model background, but also for the SUSY benchmark scenarios, as expected in case of the co-annihilation region. For the jets, except for the leading jet, the SUSY distributions tend to be higher in transverse momentum than the background. For the first jet on the other hand, SUSY jets peak at equal or even lower values, but have a larger tail to higher transverse momentum. But also for Standard Model events, the highest values reach the TeV scale.

Finally, figure 7.6 shows angular distributions concerning the three leading jets and the $\not{H}_T$ in the event. These variables are only shown if the corresponding jets in the event have a transverse momentum exceeding 30 GeV. For Standard Model events, the $\Delta\Phi(jeti, jetj)$ with $i, j = 1, 2, 3$ and $i \neq j$ peak at large values, most pronounced for the angle between the first two leading jets. The SUSY distributions are more flat, as the jets are produced in long chains and are not necessarily correlated. The fourth variable shown is the minimal angle between the $\not{H}_T$ and one of the three leading jets, min $\Delta\Phi(jet123)$. Again, this variable is more flat for SUSY events than for Standard Model background, which accumulates at small values. For QCD, this is because usually one of the first three jets is causing the $\not{H}_T$ due to mis-measurement. In case of the $W$-boson events, also the tau can be counted as jet, and is then aligned with the neutrino. Note that here also the region of small values is described worst by the simulation.

| **Event selection** | |
|---|---|
| exactly one tau<br>electron and muon veto | |
| **Base-Line** | **Full** |
| $\not{H}_T$> 250 GeV | $\not{H}_T$> 400 GeV |
| $H_T$> 350 GeV | $H_T$> 600 GeV |

Table 7.2: Base-Line and Full selection cuts. The tau and lepton veto definition is valid for both selections.

| 5 fb$^{-1}$ | Signal region | | Simulated statistics | |
|---|---|---|---|---|
| | Base-Line | Full | Base-Line | Full |
| $t\bar{t}$ | $72 \pm 4$ | $1.8 \pm 0.6$ | 322 | 8 |
| $WW \to l\nu l\nu$ + Jets | $15 \pm 2$ | $0.5 \pm 0.3$ | 85 | 3 |
| $Z \to \nu\nu$ + Jets | $17 \pm 1$ | $1.2 \pm 0.3$ | 324 | 23 |
| $Z \to ll$ + Jets | $11 \pm 2$ | $0.8 \pm 0.6$ | 27 | 2 |
| $W \to l\nu$ | $473 \pm 30$ | $30.7 \pm 7.7$ | 246 | 16 |
| QCD | $59 \pm 13$ | $9.5 \pm 5.6$ | 74 | 21 |
| Sum | $648 \pm 33$ | $44.7 \pm 9.6$ | 1080 | 73 |
| Data | 444 | 28 | | |
| LM2 | $120 \pm 1$ | $50.2 \pm 0.6$ | 17719 | 7420 |
| LM13 | $857 \pm 20$ | $119.9 \pm 7.3$ | 1915 | 268 |

Table 7.3: Event yield for both Base-Line and Full selection for 5 fb$^{-1}$. Shown are the results for simulated events in comparison with data, as well as in comparison with two SUSY benchmark models. The denoted uncertainties are the uncertainties of the simulated statistics.

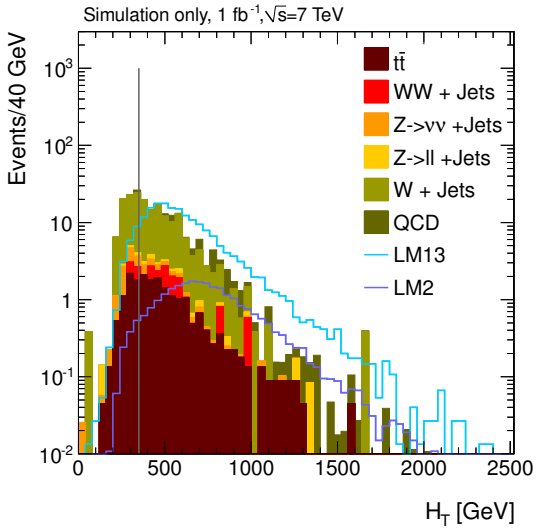


Figure 7.1: $H_T$ distribution after all Base-Line cuts but the $H_T$ cut applied normalized to 1 fb$^{-1}$ for simulated events. The cut on the hadronic transverse energy is marked with a line. Two SUSY benchmark models are shown for comparison.

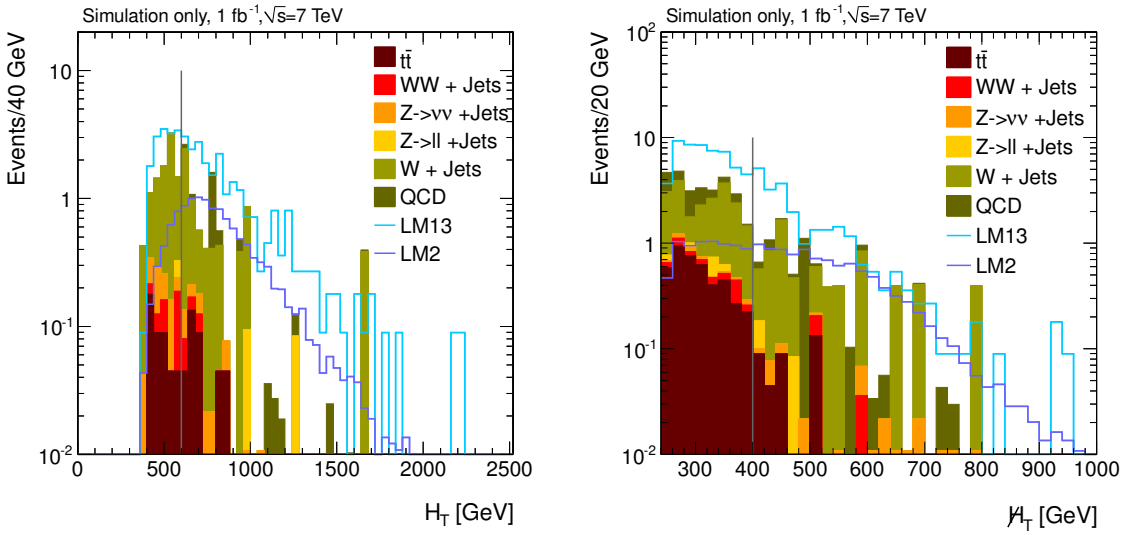


Figure 7.2: $\not{H}_T$ and $H_T$ distribution after Full selection cuts except the cut on the variable shown, marked with a line, normalized to 1 fb$^{-1}$ for simulated events. Two SUSY benchmark models are shown for comparison.

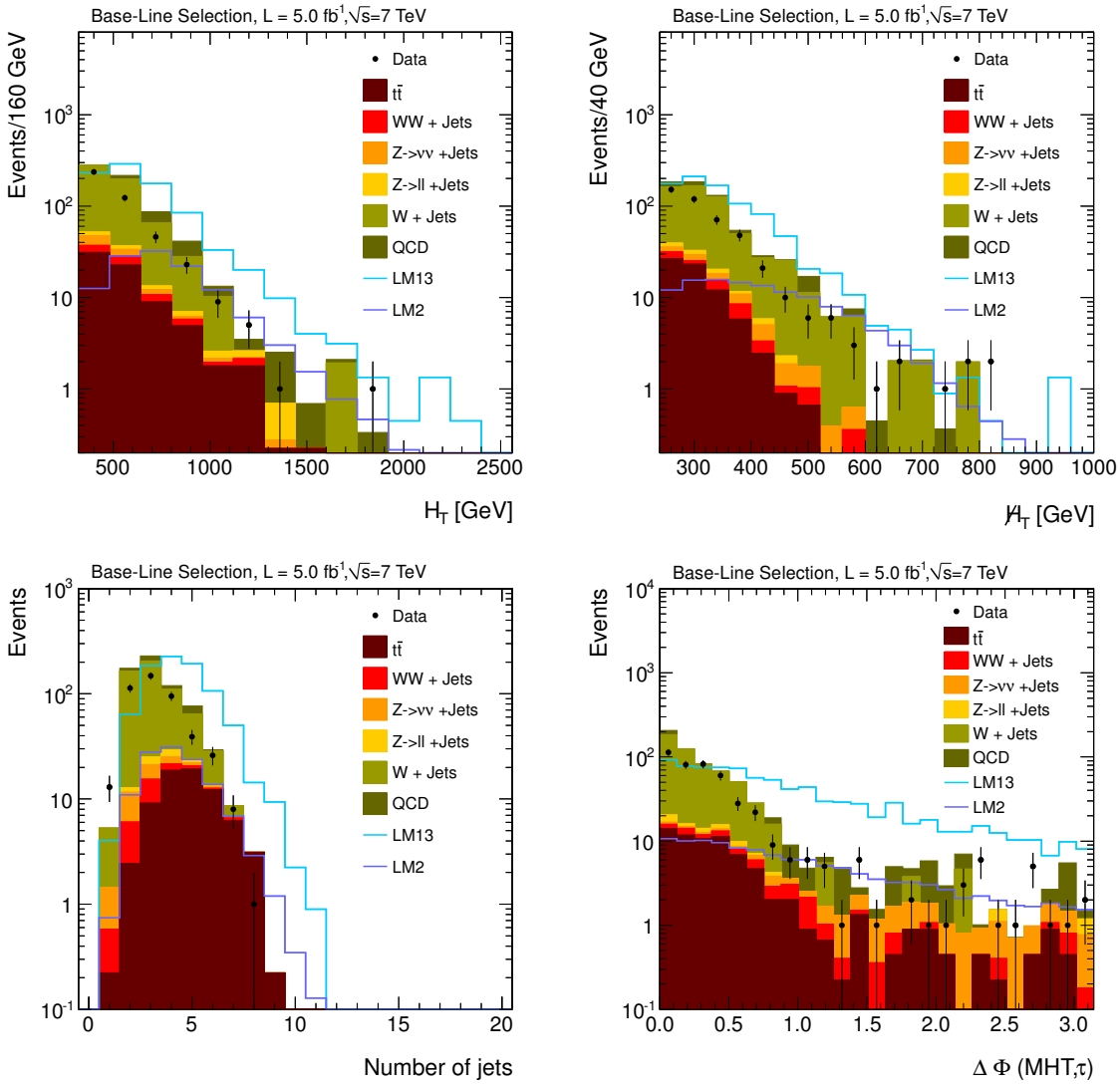


Figure 7.3: Control distributions after the Base-Line selection for 5 fb$^{-1}$: $H_T$ and $\not{H}_T$ (upper row), and number of jets with $P_T > 30$ GeV and $\Delta\Phi(\not{H}_T, \tau)$ (lower row). Shown are simulated events (filled space) and data (dots). Two SUSY benchmark models (lines) are displayed for comparison.

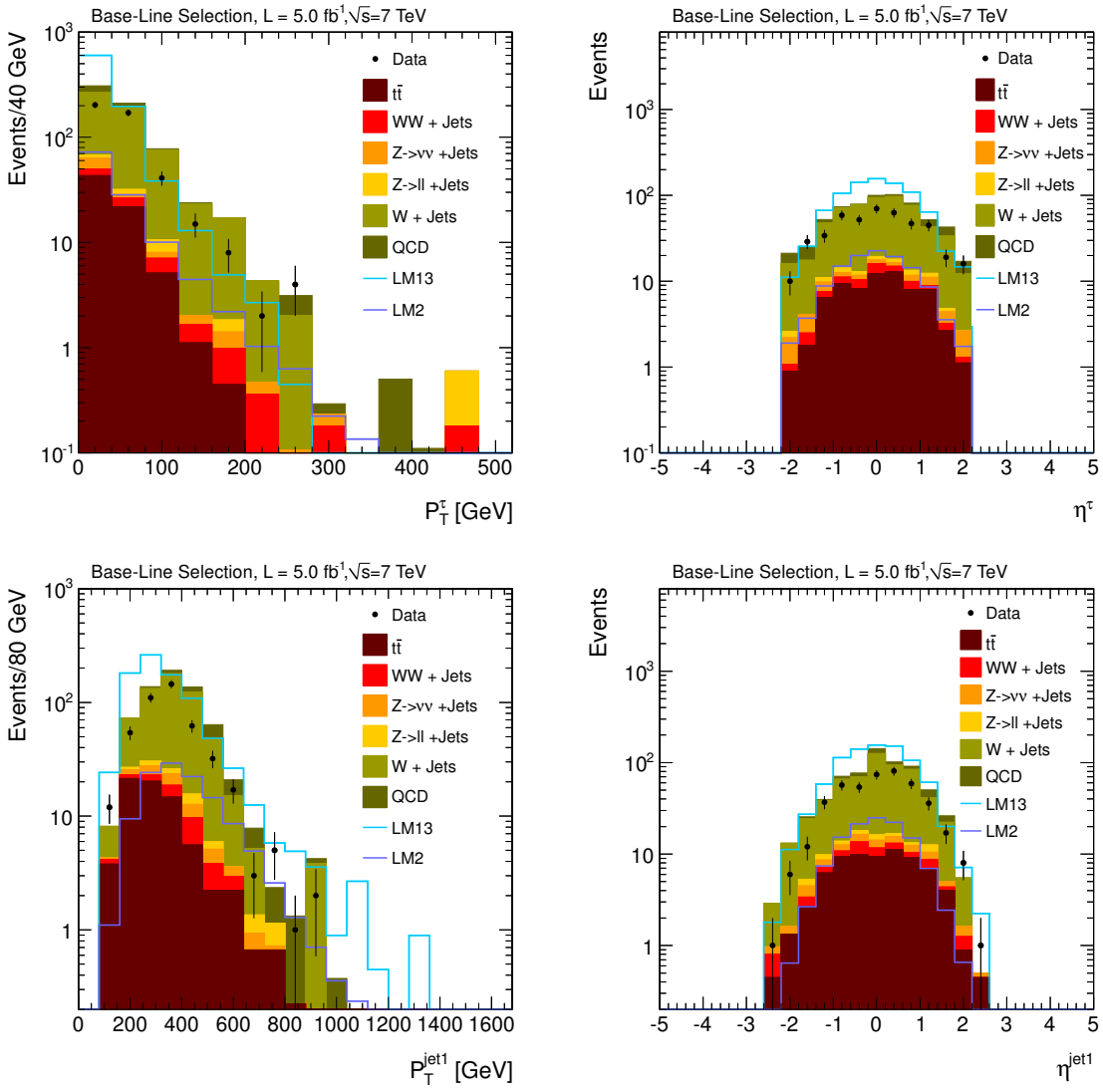


Figure 7.4: Control distributions after the Base-Line selection for 5 fb$^{-1}$: $P_T^{\tau}$ and $\eta^{\tau}$ (upper row), and $P_T^{jet}$ and $\eta^{jet}$ for the leading jet with at least 30 GeV of $P_T$ (lower row). Shown are simulated events (filled space) and data (dots). Two SUSY benchmark models (lines) are displayed for comparison.

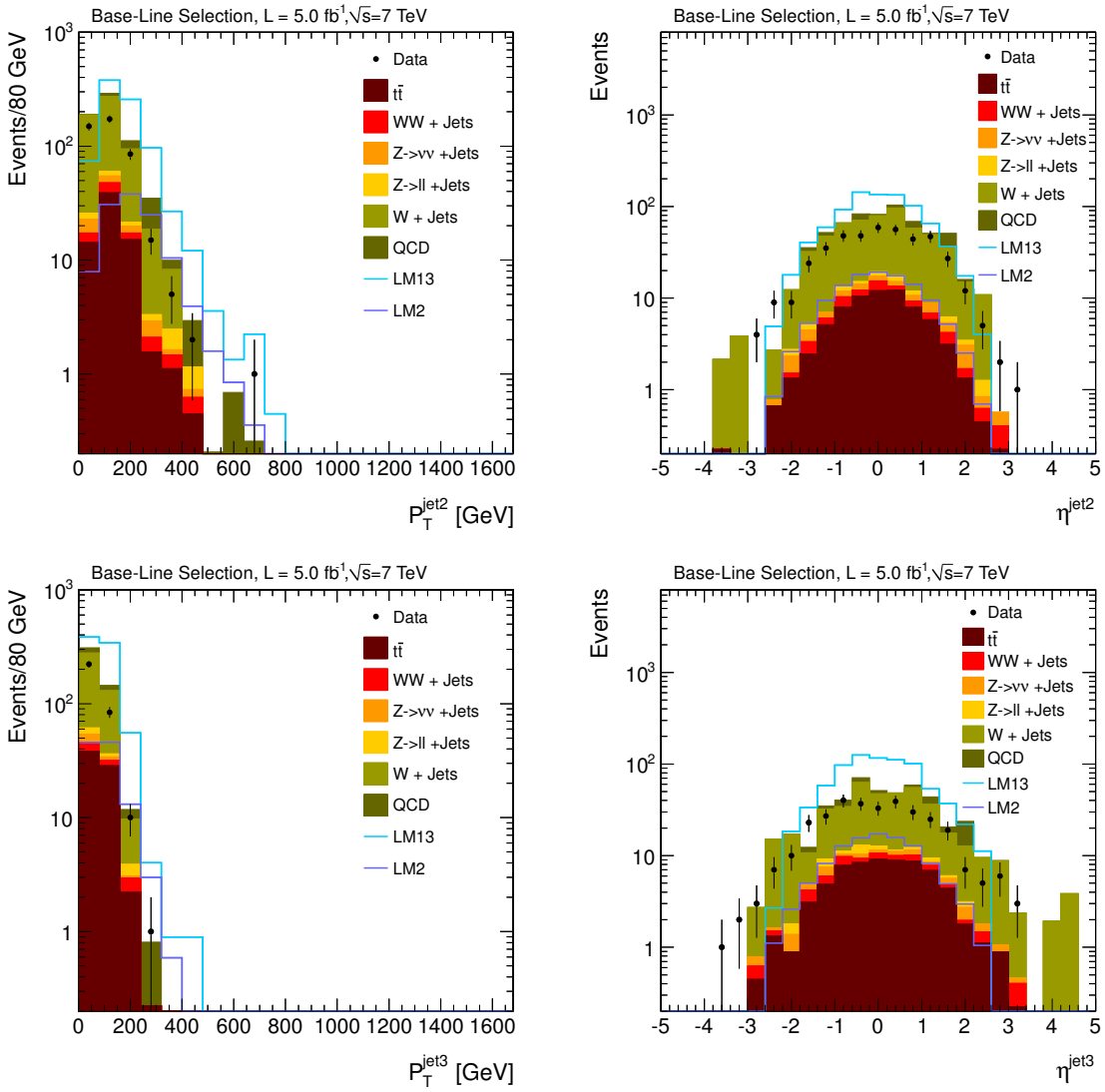


Figure 7.5: Control distributions after the Base-Line selection for 5 fb$^{-1}$: $P_T^{jet}$ and $\eta^{jet}$ for the second (upper row), and third (lower row) leading jet in case of $P_T^{jet} > 30$ GeV. Shown are simulated events (filled space) with data (dots). Two SUSY benchmark models (lines) are displayed for comparison.

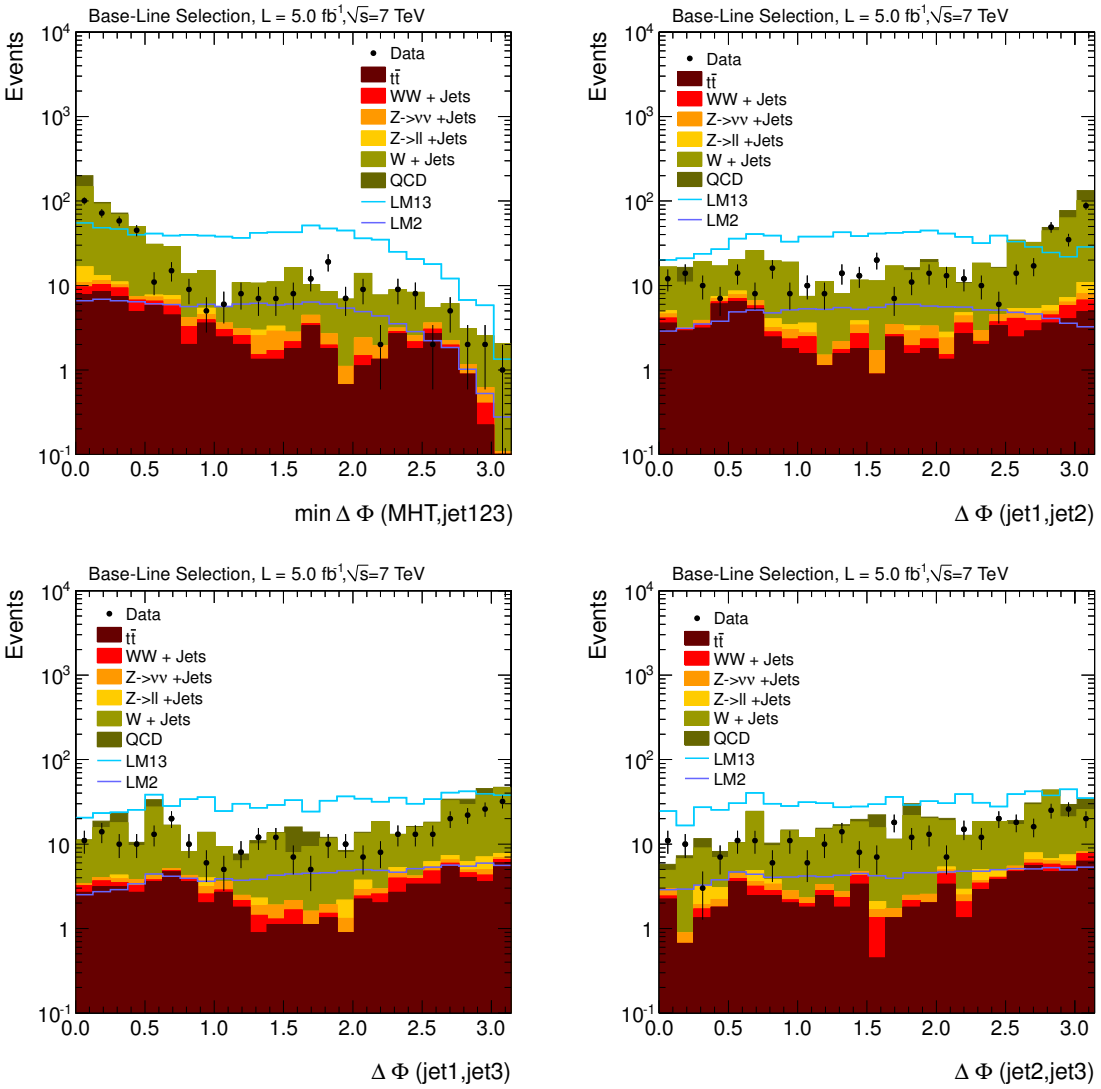


Figure 7.6: Control distributions after the Base-Line selection for 5 fb$^{-1}$: Minimal azimuthal angle between $\not{H}_T$ and the first leading jets $\min\Delta\Phi(\not{H}_T, jet(1,2,3))$ and $\Delta\Phi(jet1, jet2)$ (upper row), and $\Delta\Phi(jet1, jet3)$ and $\Delta\Phi(jet2, jet3)$ (lower row). The used jets are jets with at least 30 GeV of $P_T$. Shown are simulated events (filled space) with data (dots). Two SUSY benchmark models (lines) are displayed for comparison.

# Chapter 8

# Background Estimation

The event yield predicted by simulation overestimates the event yield observed in data, as shown in section 7.4. Especially high values of $\not{H}_T$ and $H_T$ are sensitive to inaccuracies of the simulation. Hence, in this study, background estimation based on data instead of simulation ("data-driven") was developed. The background was divided in two components. First, the production of real taus by standard model processes is considered. The production of $W$-bosons associated with jets is the main channel for true taus in the events, with a sizable contribution of $t\bar{t}$. Second, the mis-identification of quark or gluon jets as tau-jets. The probability of a single jet faking a tau is of the order of 1%, depending on its momentum and pseudorapidity. The huge cross-section of QCD, together with the requirement of a large $H_T$, which increases the average number of jets, leads to a non-vanishing contribution of fake-tau background. As said, the main background process here is QCD multi-jet production. There is also a contribution from $Z$-boson production, which due to decay into neutrinos produce real missing transverse momentum in the event.

## 8.1 Estimate of Real-Tau Background

In Standard Model processes, several possibilities exist to produce real taus. The main background in the examined search region is the associated production of a $W$-boson and jets. The $W$-boson can decay into a hadronic tau and a neutrino, yielding missing transverse momentum, and the jets are producing the required transverse energy.
Due to lepton universality, muons are produced in $W$-decays almost[1] as often as taus. The muon momentum is measured very precisely with respect to the hadronic decay products of the tau. As both the muon mass as well as the tau mass is much smaller than the $W$-boson mass, the spectrum of transverse momenta of both leptons is practically the same. This can be used to treat the muons as true taus, with only very small deviations due to mis-measurement of the reconstructed muons.
The method to estimate the real-tau background commits of several steps, which will be

[1]The difference in the branching fraction is small. It is measured to be $10.57 \pm 15$ % for muons and $11.25 \pm 20$% for taus [8].

explained in detail in the following. In short, they are:

- Select data events with exactly one muon and high $H_T$.
- Obtain a template for the reconstructed visible tau $P_T^{\tau,\text{reco}}$ as function of the generated tau $P_T^{\tau,\text{gen}}$.
- Replace the $P_T$ of the muon with a randomly chosen value form the template.
- Weight the event with the reconstruction efficiency of the tau, the probability of the muon being from a tau decay, etc.

Data events with muons suggest to use a muon trigger. Unfortunately, the threshold on $P_T$ for single muons on trigger level is already above the minimal tau $P_T$ of 15 GeV. As the muon shall be used to model the tau, and the region with soft taus is especially important, a muon trigger cannot be used. Instead, the $\not{H}_T$ trigger is used, and events which would pass the corresponding offline cut only after manipulating the muon described in the following are treated as systematic uncertainty.
The muon is defined as in section 7.1, except for a harder cut on the pseudorapidity, i.e. $|\eta| < 2.1$, to emulate the tau acceptance. A tau response template $P_T^{\tau,\text{reco}}/P_T^{\tau,\text{gen}}$ was derived on the full sample of simulated $W$-boson events (see section 5.1), which describes the visible reconstructed $P_T^{\tau,\text{reco}}$ of the tau-jet with respect to the original generated tau $P_T^{\tau,\text{gen}}$. Generated hadronically decaying taus are selected, and reconstructed taus are matched in $\Delta R = \sqrt{\eta^2 + \phi^2}$, with $\Delta R < 0.2$. No discriminators to identify the tau as a tau were used, as the identification efficiency is not close to one and both identified and not identified taus are needed for an accurate description of the response of the tau. The resulting template depends both on the transverse momentum of the generated tau as well as the number of reconstructed vertices $nV$ in the event in order to take Pile-Up into account (see figures 8.18.2 and 8.3). The $P_T$ of the muon is replaced by a randomly chosen value from the template to the $P_T$ distribution of the visible tau-jet. For each event in data, this is done once.

A reconstructed hadronically decaying tau will always be associated to a jet, for which several energy corrections will be applied. Hence, the corrected tau jet will be used for the computation of $H_T$ and $\not{H}_T$, if it passes the corresponding $P_T$ cuts. Similar corrections are applied to the "mimicry tau" derived by the muon method, before it is added to $H_T$ and $\not{H}_T$ . For the estimate, the mimicry tau, $H_T$ and $\not{H}_T$ have to pass the corresponding selections. Only events with exactly one muon were considered. The events also have to pass the electron veto. Several weighting factors have to be applied to the selected events, which are explained in the following. If not otherwise noted, all efficiencies and scaling factors are determined on simulated $W$ plus jets events, as this is the dominating background. The corrections used are the following:

- **Muon reconstruction efficiency**: The efficiency of the identification of a muon $\epsilon_\mu^{reco}$ is close to unity, and depends on the additional activity in the event. It is parameterized in $P_T$ and $\eta$ of the muon. It was derived on data from $Z$ plus jets data events and was taken from [100] (see appendix A).

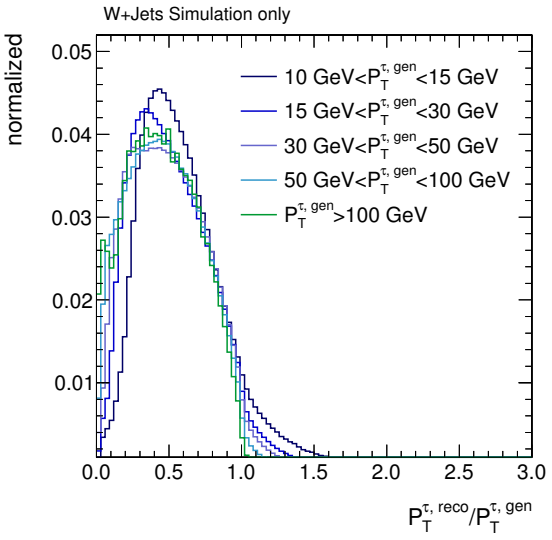


Figure 8.1: $P_T^{\tau,gen}$ dependence of the template. No requirement on the number of Vertices has been applied. It was obtained on simulated $W$ plus jets events and normalized to one.

- **Muon isolation efficiency**: Muon isolation is required to distinguish muons of prompt decays of gauge bosons from muons of heavy-flavor decays. In addition to the muon, in gauge boson decays, no further activity in the event is produced, except an additional lepton in case of a $Z$-boson. As the production of the heavy boson is usually accompanied with very few jets, it is likely to be isolated. In heavy-flavor decays, the muon is accompanied by further hadronic particles, and thus part of a jet. Due to further activity in the event unrelated to the gauge boson decay, the isolation requirement on the muon is not fully efficient. The applied correction to the isolation efficiency $\epsilon_\mu^{iso}$ is parameterized in $\Delta R = \sqrt{\Delta\eta^2 + \Delta\phi^2}$ to the next jet and $P_T^{rel} = \frac{P_T^\mu}{P_T^{nextjet}}$ and was also taken from [100] (see appendix A)

- **Muons produced in tau decays**: Around 17% of the taus decay into a muon and two neutrinos. Hence, the probability of a muon not being from a tau decay $p_\mu^W$ and thus the correction factor depends on $P_T$. The correction factor will also depend on the $\not{H}_T$ requirement of the event, because in this decay two additional neutrinos, hence, $\not{H}_T$ are produced (see figure 8.4, left). To take this effect into account, the correction factor depending on the $P_T$ of the muon, is taken from $W$ plus jets simulation with at least 250 GeV of $\not{H}_T$. It is used for both the Base-Line and Full selection, as the difference between the correction factor with $\not{H}_T > 250$ GeV (corresponding to the Base-Line selection) and $\not{H}_T > 400$ GeV (corresponding to the Full selection) is already within statistical uncertainty.
  Another dependence of this probability is on $H_T$. In events with a larger $H_T$, the $W$-bosons tend to be more boosted than with less $H_T$. This leads to a higher missing

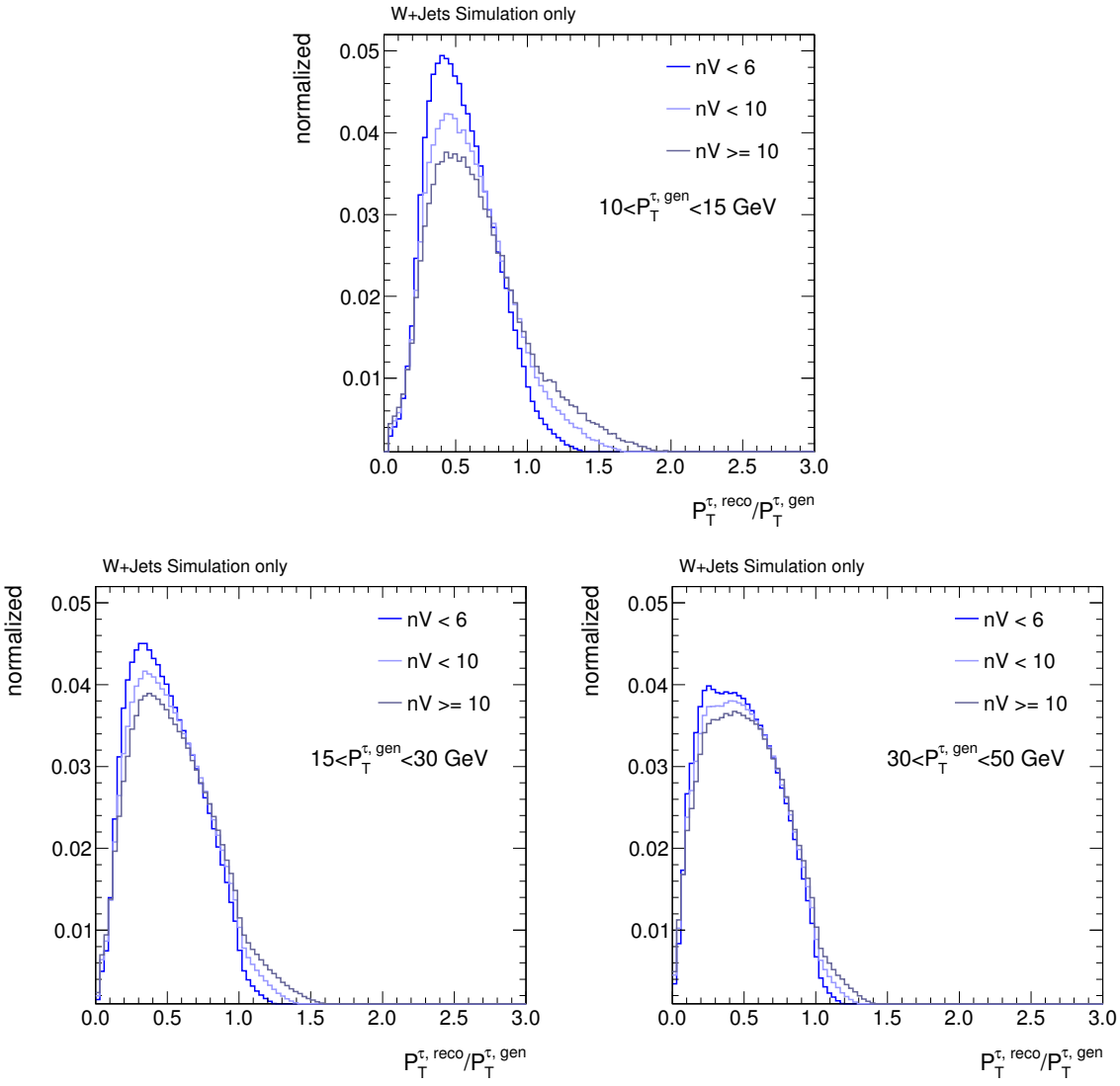


Figure 8.2: Dependence of the response on the number of reconstructed vertices for different intervals of $P_T^{\tau,gen}$. It was obtained on simulated $W$ plus jets events and normalized to one.

transverse momentum, and lessens the effect of preferring the selection of events with more neutrinos, i.e. events where the muon comes from a tau decay. Due to limited statistics in the simulated sample, the weighting factor cannot be parametrized in $H_T$ in addition to $\not{H}_T$. The difference between $p_\mu^W$ for a sample with $\not{H}_T > 250$ GeV and a sample with an additional requirement of $H_T > 350$ GeV is again within the statistical uncertainty, and thus, only the weight obtained in a sample with $\not{H}_T > 250$ GeV is used.

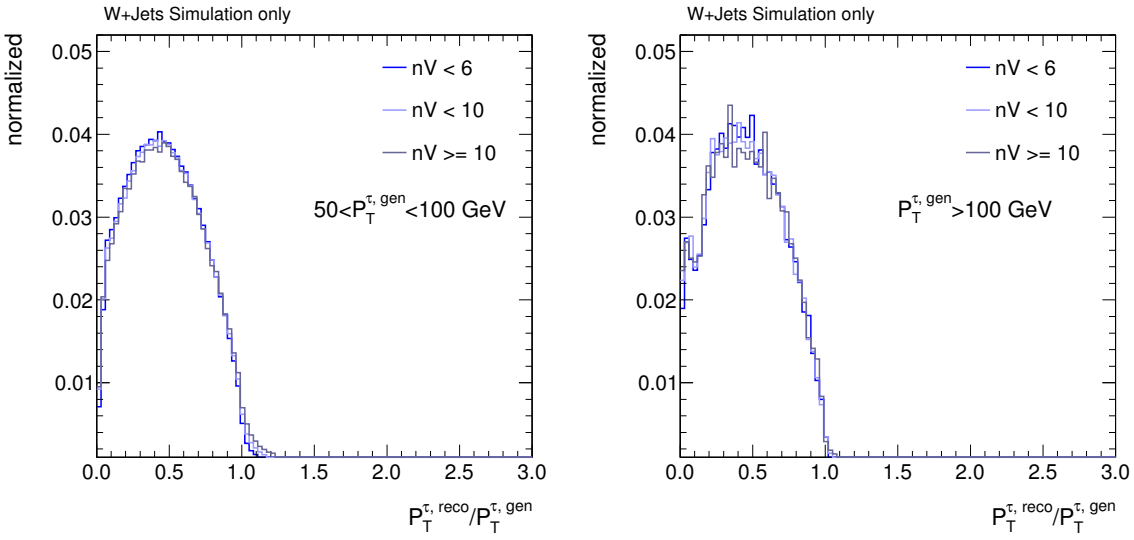


Figure 8.3: Dependence of the response on the number of reconstructed vertices for different intervals of $P_T^{\tau,gen}$. It was obtained on simulated $W$ plus jets events and normalized to one.

- **Tau reconstruction efficiency**: Not all of the hadronically decaying taus can be identified as such. The probability of a tau to be isolated depends on the number of particle flow candidates, i.e. photon candidates $N^G$ and charged hadron candidates $N^C$ with a minimum quality cut of $P_T > 0.5$ GeV applied, within the isolation area (see figure 8.5). To a smaller amount, it depends also on the objects visible transverse momentum $P_T^{\tau,vis}$. If parametrized in this way, the difference in reconstruction efficiency between the environments of $W$-boson production and $t\bar{t}$ can be suppressed (see figure 8.6 and 8.7).

- **Tau hadronic branching fraction**: As described in chapter 6.1, only 64.8% of the produced taus decay hadronically. As the muons mimic the originally produced taus, the selected events are scaled by this factor $f_\tau^{bf(hadr)}$.

Except for the tau hadronic branching fraction, the value of the correction factors differs in each event. They are combined to an overall weight applied to each event:

$$f_{event}^{corr} = \frac{p_\mu^W \times \epsilon_\tau^{ID} \times f_\tau^{bf(hadr)}}{\epsilon_\mu^{reco} \times \epsilon_\mu^{iso}} \tag{8.1}$$

A consistency test ("closure test") of the method is done by comparing the mimicked tau events described above with events containing a real tau, where both samples are coming from simulation. The uncertainty on this method is composed of the statistical

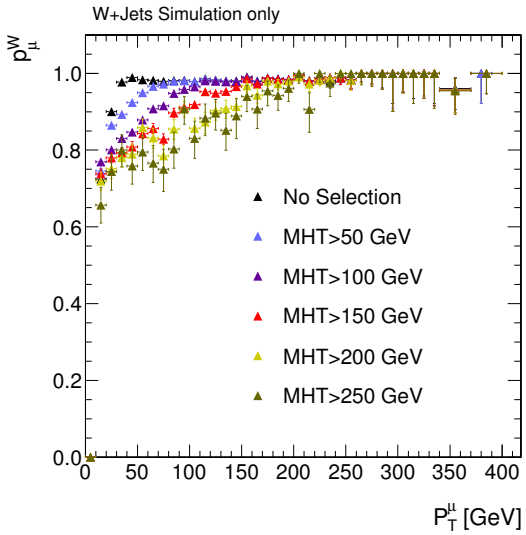


Figure 8.4: Probability $p_\mu^W$ of a muon being not produced in a tau decay for $W$-boson plus jets events, as a function pf the transverse momentum of the muon, for different region of $\not{H}_T$.

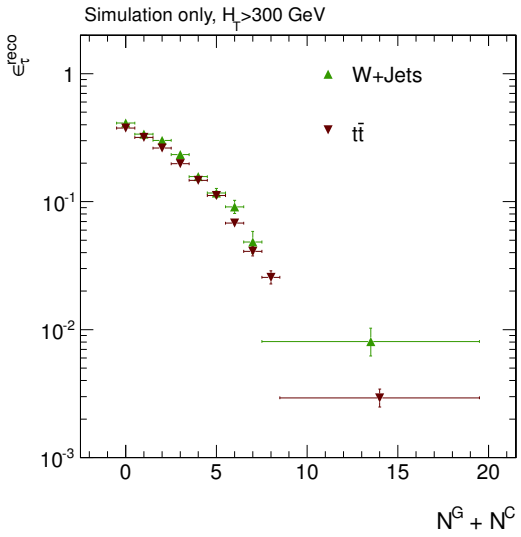


Figure 8.5: Tau reconstruction efficiency depending on the sum of the number of photon candidates $N^G$ and charged hadron candidates $N^C$ within the isolation cone. It is shown for the full range of transverse momentum in $W$-boson and $t\bar{t}$ events.

uncertainty of the muon sample used for the prediction. In addition, the statistical uncertainties of the tau reconstruction efficiency and the probability of the muon being from

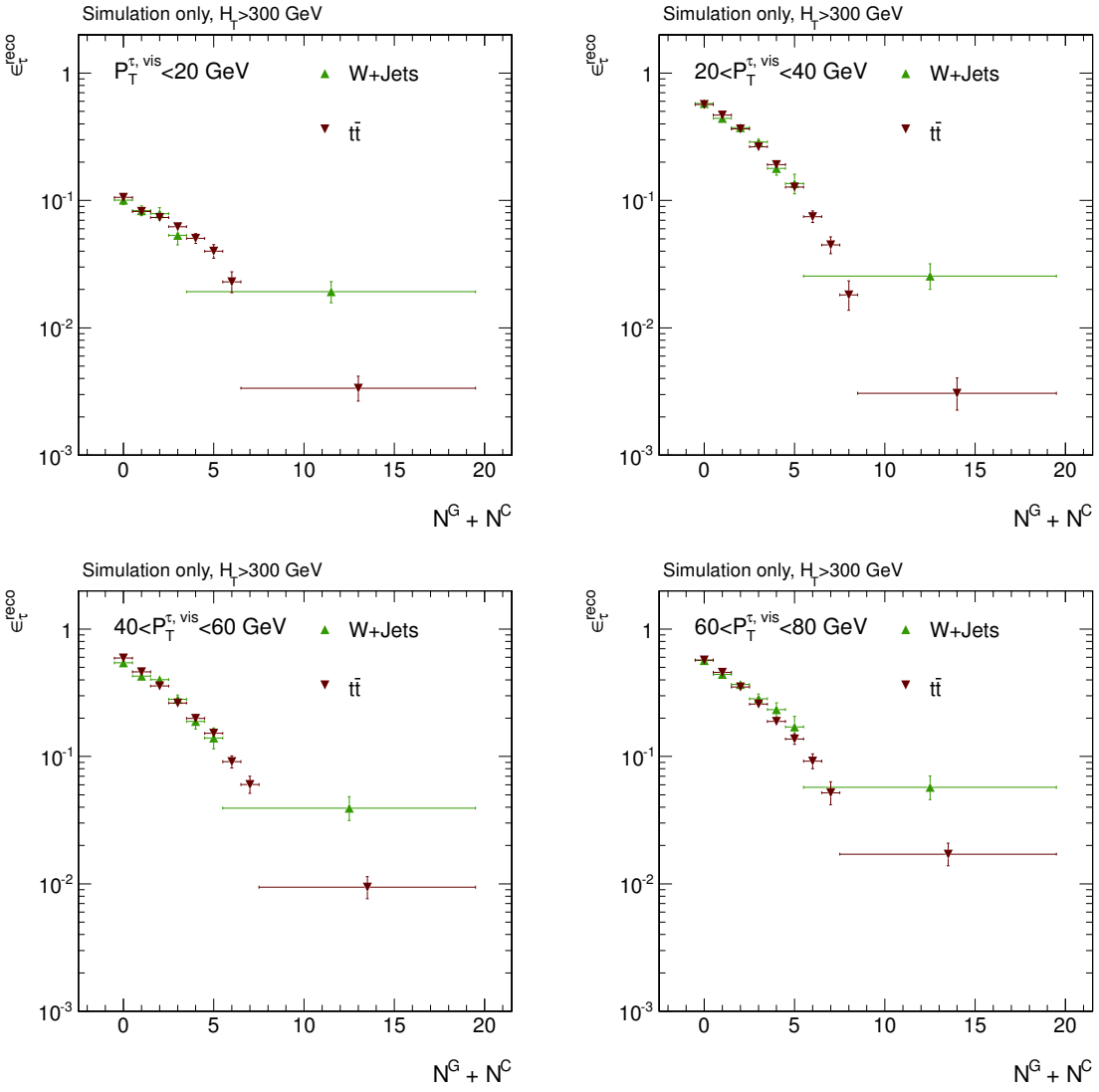


Figure 8.6: Tau reconstruction efficiency depending on the sum of the number of photon candidates $N^G$ and charged hadron candidates $N^C$ within the isolation cone. It is shown for the reconstruction efficiency in $W$-boson events and $t\bar{t}$ for different bins of transverse momentum.

a tau decay are taken into account. The influence of the statistical uncertainties on the muon reconstruction and isolation efficiencies as well as the uncertainty on the hadronic branching fraction of the tau are significantly smaller than 1%. All uncertainties considered are added up in quadrature.
Figure 8.8, 8.9, 8.10 and 8.11 show various distributions of tau events (black triangles), which have in addition the reconstructed tau matched to a generated tau on simulation level, compared to the events predicted with the muon method (green filled space), on sim-

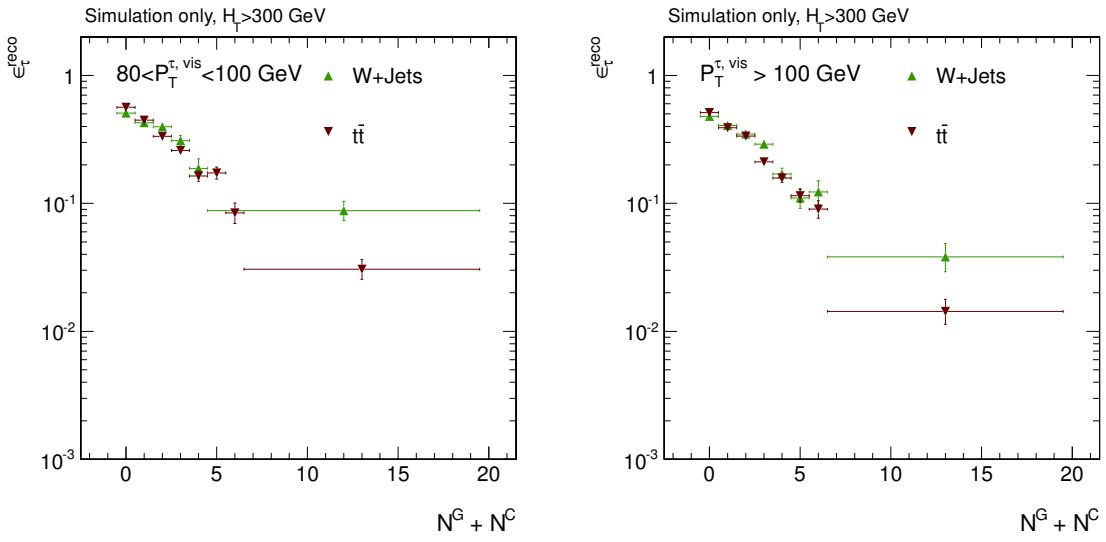


Figure 8.7: Tau reconstruction efficiency depending on the sum of the number of photon candidates $N^G$ and charged hadron candidates $N^C$ within the isolation cone. It is shown for the reconstruction efficiency in $W$-boson events and $t\bar{t}$ for different bins of transverse momentum.

ulated events of $W$-bosons and associated production of jets. The hatched areas indicate the uncertainty described above. The prediction via the muon sample describes the selected tau sample within the statistical fluctuations. Both $H_T$ and $\not{H}_T$ are well described by this method. Also, the transverse momentum and pseudorapidity of the tau and the first three jets (with at least 30 GeV of transverse momentum) can be modeled with the muon sample. Angular distributions like the smallest azimuthal angle between the $\not{H}_T$ and the first three leading jets $min(\Delta\Phi(\not{H}_T, jet123))$ and the azimuthal angle between the leading jets $\Delta\Phi(jeti, jetj)$ with $i, j = 1, 2, 3$ and $i \neq j$ are described as well. The description of the number of jets with $P_T > 30$ GeV is reasonable good.
For $W$-bosons, the azimuthal angle between $\not{H}_T$ and the tau, $\Delta\phi(\not{H}_T, \tau)$ seems to be described in an acceptable manner, although a small deviation in the tail can be seen. In $t\bar{t}$ events, this effect is pronounced more strongly (see figure 8.12). As the real tau decays into the hadronic decay products $\tau_h$ and a neutrino, there is a small azimuthal angle between the final reconstructed tau and the produced real tau. However, this angle is of the order of 0.01, and cannot account for this deviation. Instead, the reason for the muon events having a slightly smaller $\Delta\Phi$ between the $\not{H}_T$ and the tau is the presence of muons produced in tau decays in the sample. In case of a muon directly produced in $W$-boson decays, the template method mimics the one neutrino produced in a hadronic tau decay reasonable good, and the $\not{H}_T$ is modified in an acceptable manner. In case of a muon coming from a leptonic tau decay, two additional neutrino are produced, which are part of the $\not{H}_T$ in the event, and a third is mimicked by the template method. As the $W$-bosons in both $W$-boson

and $t\bar{t}$ production are lorentz boosted, this leads on average to a smaller angle between the muon and the $\not{H}_{\mathrm{T}}$. Figure 8.13 shows the $\Delta\phi(\not{H}_{\mathrm{T}}, \tau)$ for $W$-boson (upper row) and $t\bar{t}$ (lower row) events for hadronic tau decays (black triangles) and the real-tau prediction method with muons not produced in a leptonic tau decay (left) and muons produced in tau decays (right). The distributions were normalized in order to compare the shapes. It can be seen that the muons directly produced in $W$-boson decays describe the distribution of the tau events, but the muons produced in a tau decay clearly form a distribution with a too small $\Delta\Phi$. To account for this, one could parametrize the probability $p_{\mu}^{W}$ of a muon being from a tau decay in addition to the $\mathrm{P_T}$ of the muon in $\Delta\phi(\not{H}_{\mathrm{T}}, \tau)$. With the current simulated statistics of the $W$-boson sample, however, this is not possible. As this analysis is a cut-and-count analysis, and there is no cut imposed on this particular angle, this effect is not a problem for the final result.

$W$-boson and associated jet production is the most important, but not only source for single-muon events. The second most important contribution is $t\bar{t}$ production, where in one branch the $W$ decays into a well identified muon, but the other branch decays either hadronically or into an (unidentified) tau or into a light lepton which is lost. Standard Model processes containing a $Z$-boson or two $W$-bosons can also contain one muon, if the second lepton is lost. Muons from heavy-flavor-decays in processes not containing a heavy boson are negligible. The event yield of the accounting processes as predicted from simulation are summarized in table 8.1 for the Base-Line and in table 8.2 for the Full selection, normalized to 1 $\mathrm{fb}^{-1}$. Also shown for illustration are the number of muon events expected for 1 $\mathrm{fb}^{-1}$, as well as the number of simulated events in the muon sample as well as in the tau sample.
For the Base-Line selection, all backgrounds producing real taus are described well with this method. For the Full selection, this is also true, except for $t\bar{t}$, which shows an overprediction of 100%. This is due to the fact that in $t\bar{t}$ events, the probability of having many particles around the lepton is higher than for $W$-boson production. The reconstruction efficiency however was calculated on a simulated sample with limited statistics in this area (see figure 8.5). The presence of $t\bar{t}$ leads to an 4% overprediction overall. Still, the number of predicted events of all backgrounds in the Full selection agrees with the number of selected events within statistical uncertainties, and thus, the $t\bar{t}$ contribution was treated as systematic uncertainty.

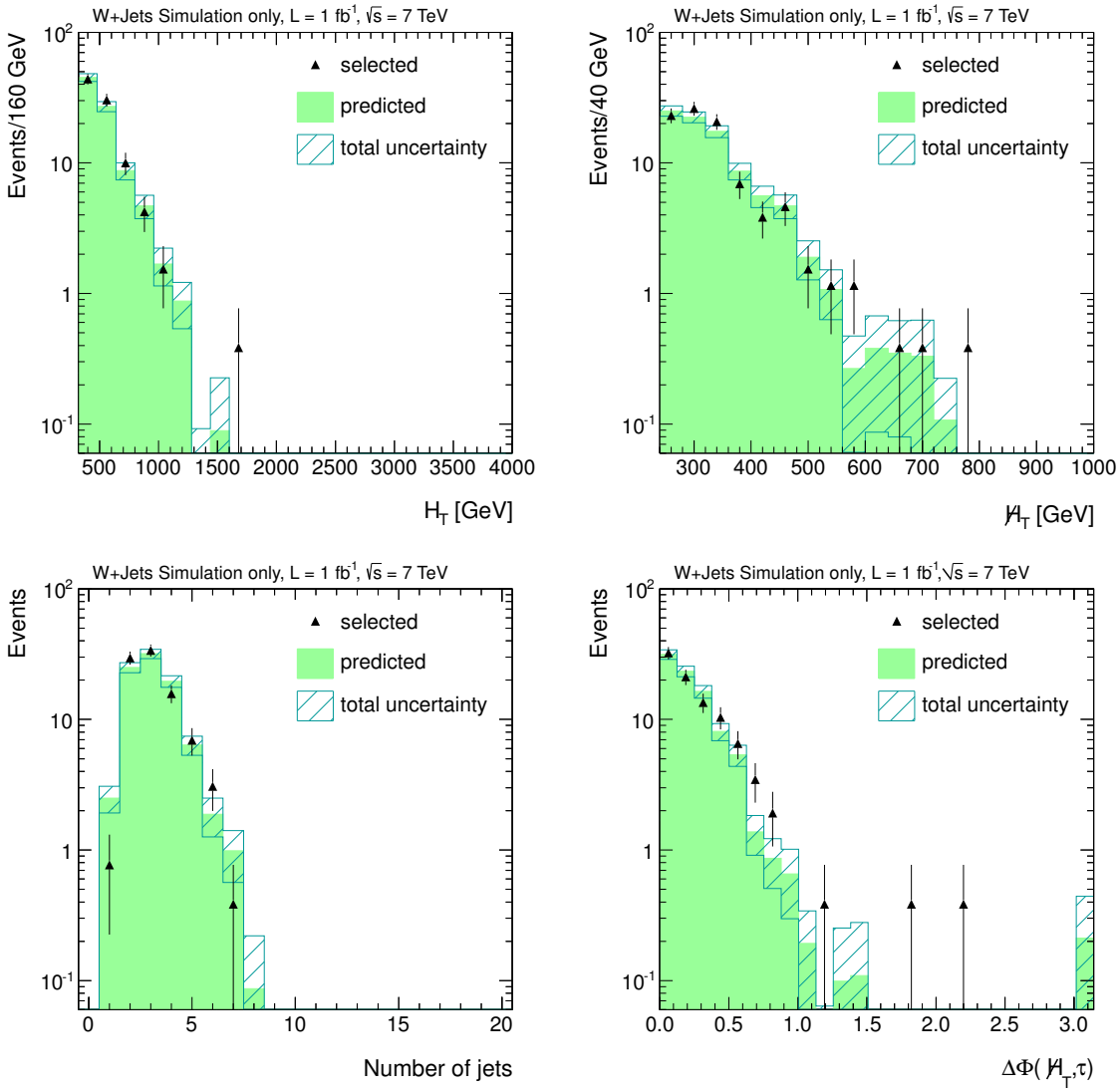


Figure 8.8: $H_T$ and $\not{H}_T$ (upper row), and number of Jets with $P_T > 30$ GeV and $\Delta\Phi(\not{H}_T, \tau)$ (lower row) distributions for the real-tau estimate in $W$ plus jets simulated events. The black triangles are the simulated events passing the Base-Line selection and having the reconstructed tau matched to a generated tau on simulation level. The filled green area gives the predicted events. The hatched areas are the uncertainties composed of the statistical uncertainties of the sample, as well as the systematic uncertainties. The events are normalized to 1 fb$^{-1}$ of luminosity.

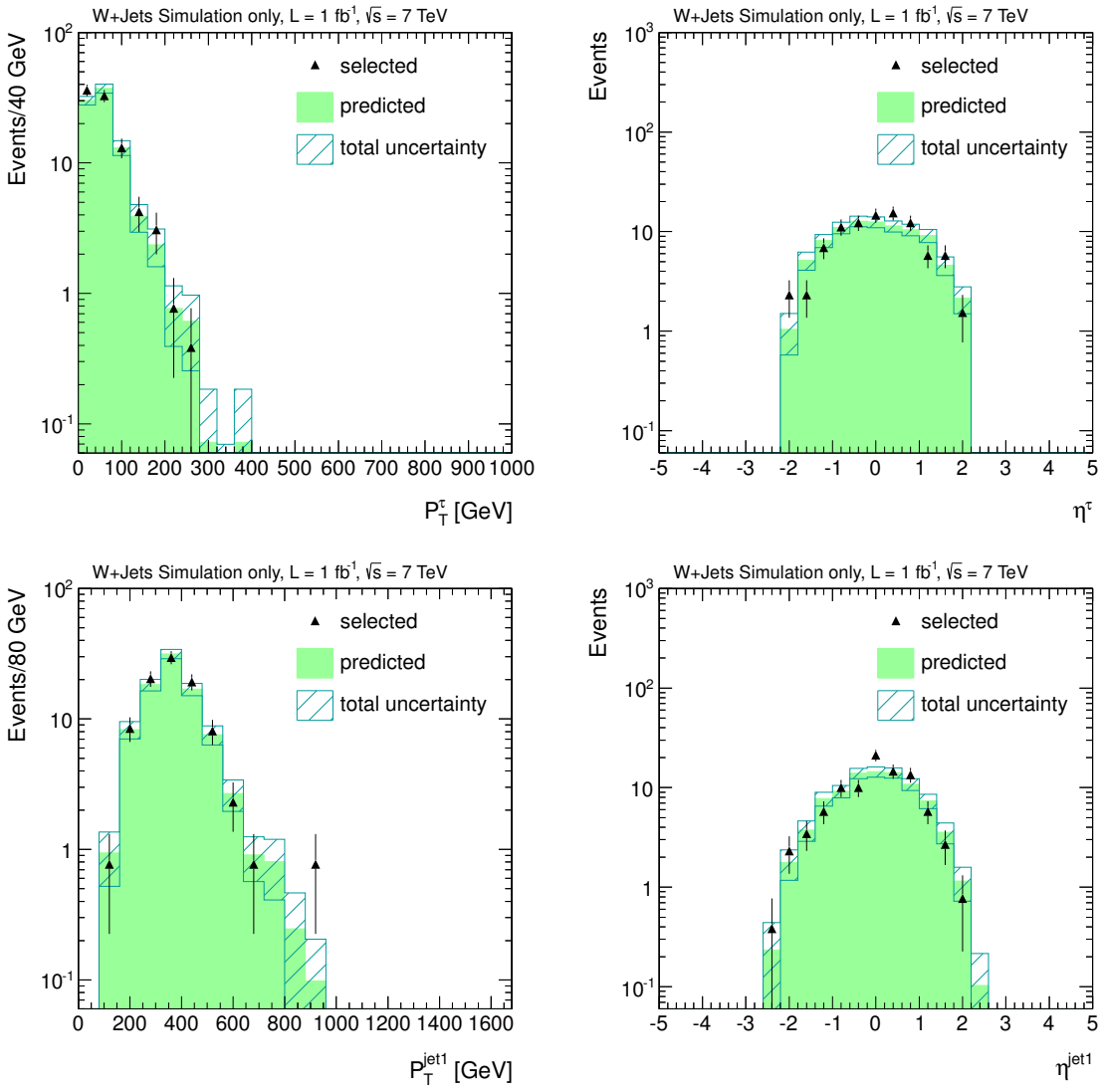


Figure 8.9: $P_T$ and $\eta$ of the tau (upper row), and the leading jet for the case of $P_T^{jet} > 30$ GeV (lower row) for the real-tau estimate in $W$ plus jets simulated events. See figure 8.8 for details.

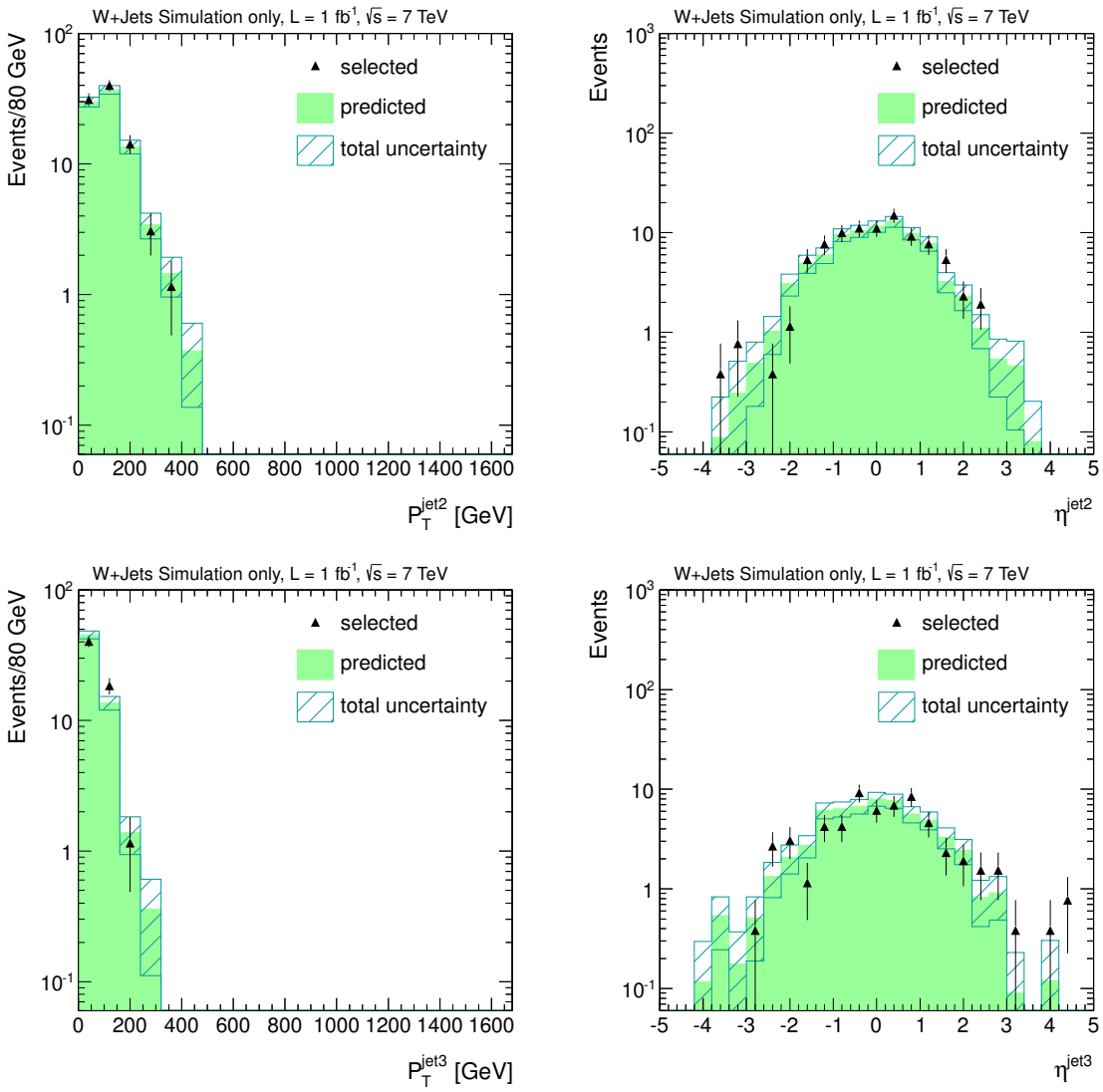


Figure 8.10: $P_T$ and $\eta$ of the second (upper row), and the third leading jet (lower row) in case of $P_T^{jet} > 30$ GeV for the real-tau estimate in $W$ plus jets simulated events. See figure 8.8 for details.

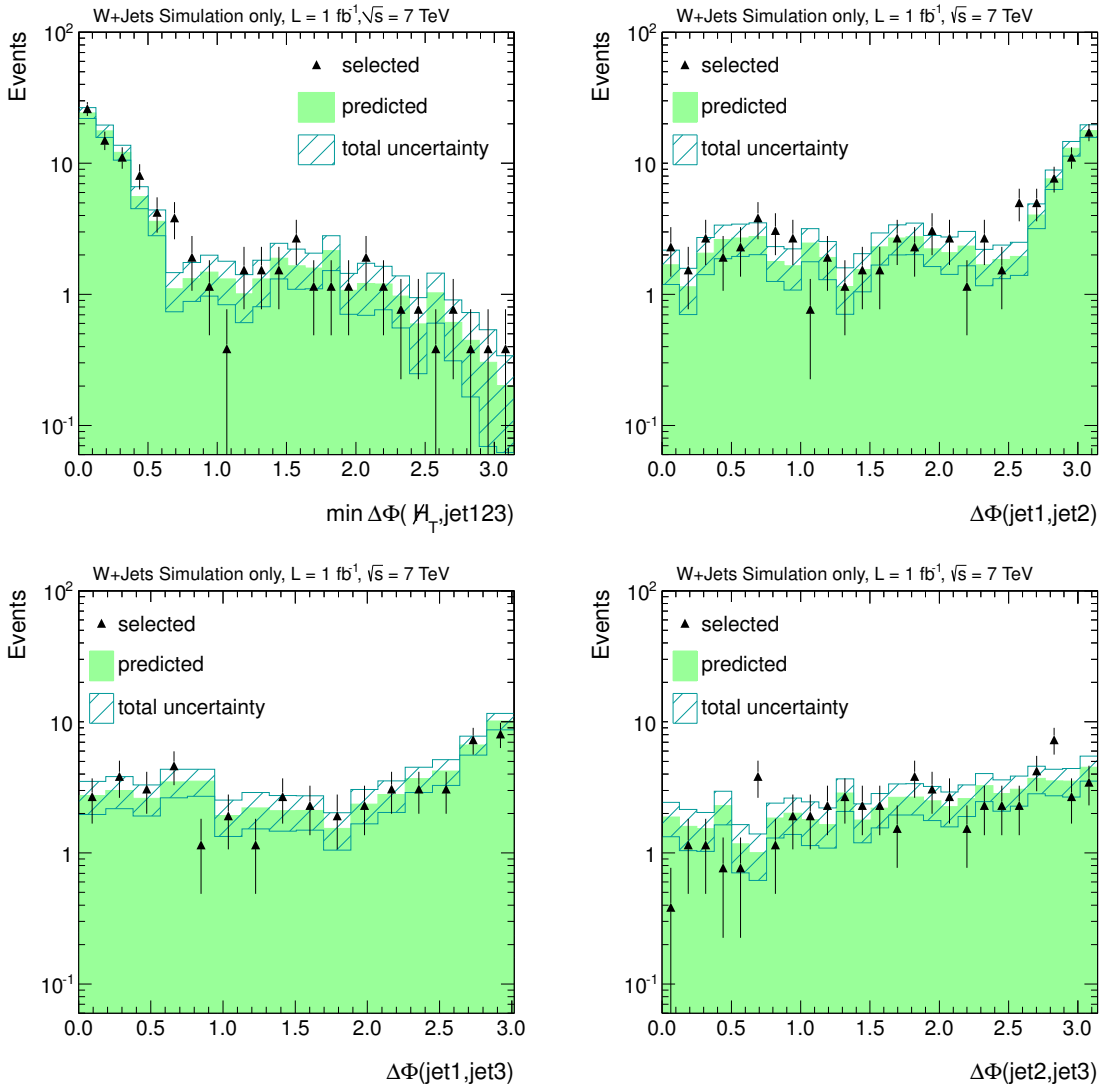


Figure 8.11: Minimal angle between $\not{H}_T$ and the first leading jets $\min\Delta\Phi(\not{H}_T, jet(1,2,3))$ and $\Delta\Phi(jet1, jet2)$ (upper row), and $\Delta\Phi(jet1, jet3)$ and $\Delta\Phi(jet2, jet3)$ (lower row) for the real-tau estimate in $W$ plus jets simulated events. The used jets have at least 30 GeV of $P_T$. See figure 8.8 for details.

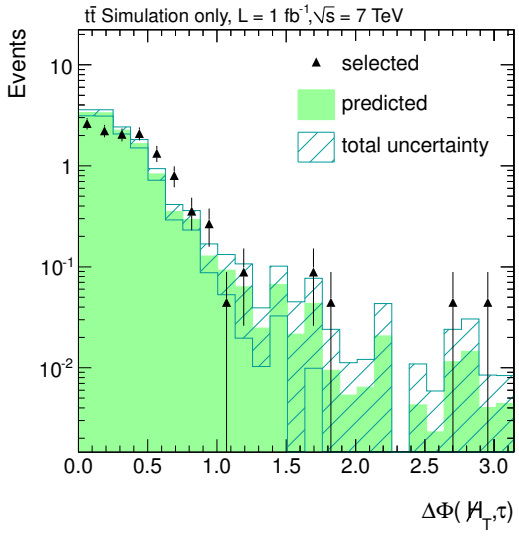


Figure 8.12: $\Delta\Phi(\not{H}_{\mathrm{T}}, \tau)$ for $t\bar{t}$ events. See figure 8.8 for details.

| Samples | L=1 fb$^{-1}$ | | | Simulated statistics | |
|---|---|---|---|---|---|
| | Selected | Predicted | Muon | Tau | Muon |
| $Z \to ll$ + Jets | $2.2 \pm 0.4$ | $1.7 \pm 0.3$ | 2.6 | 26 | 98 |
| $WW \to l\nu l\nu$ + Jets | $3.0 \pm 0.3$ | $2.9 \pm 0.2$ | 4.5 | 84 | 390 |
| $t\bar{t}$ | $12.1 \pm 0.7$ | $12.6 \pm 0.4$ | 19.5 | 272 | 2117 |
| $W \to l\nu$ | $90.5 \pm 5.9$ | $88.2 \pm 4.1$ | 136.2 | 235 | 1105 |
| Sum | $107.8 \pm 6.0$ | $105.4 \pm 4.1$ | 168.8 | 617 | 3710 |

Table 8.1: Event yield expected from different Standard Model processes for the real-tau estimate at a luminosity of 1 fb$^{-1}$ in the Base-Line selection. The selected events having the reconstructed tau matched to a tau at generator level. The predicted events are derived by the template method. Also shown for illustration are the number of muon events expected for 1 fb$^{-1}$, as well as the number of simulated events in the muon sample as well as in the tau sample.

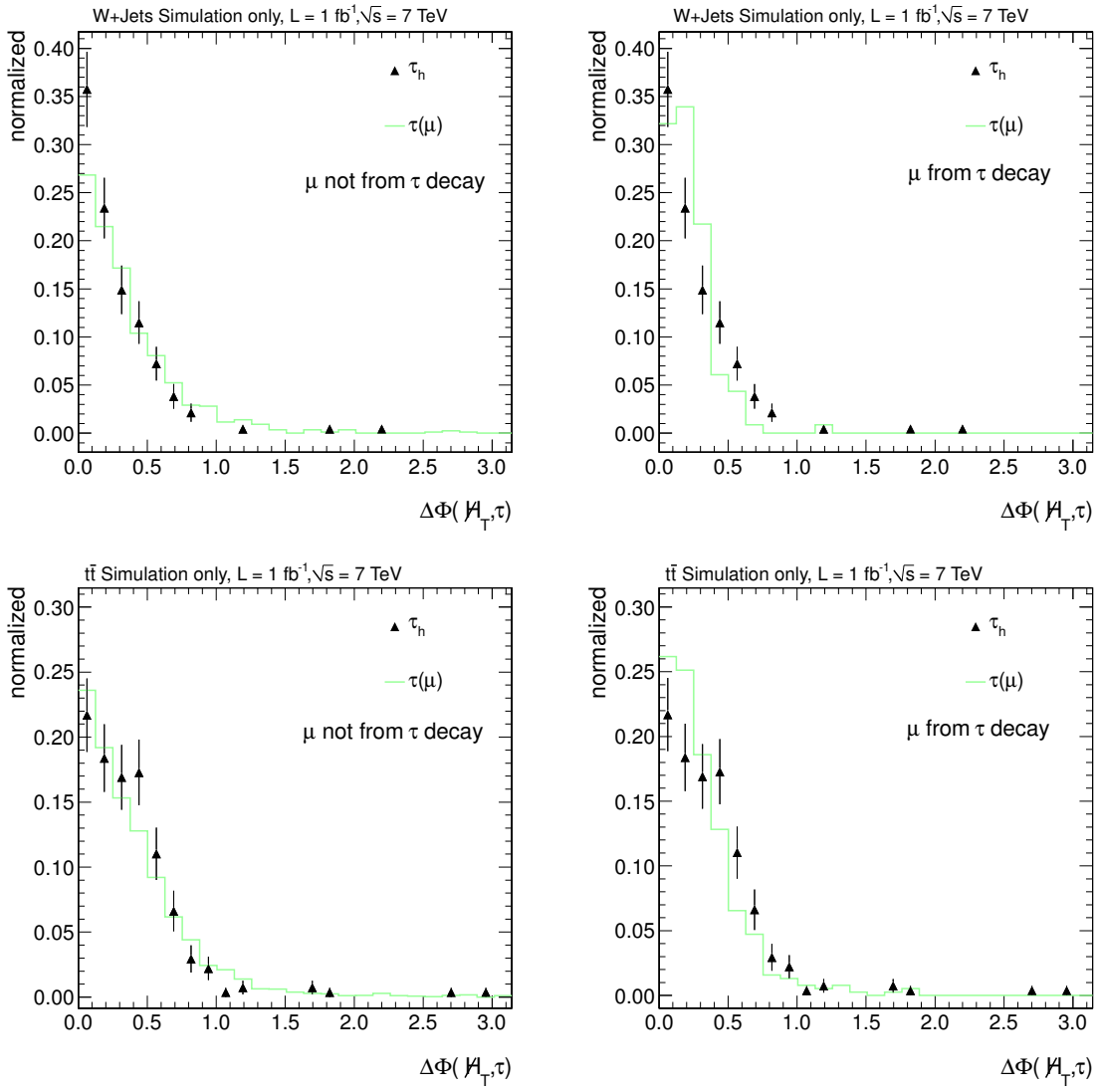


Figure 8.13: $\Delta\Phi(\not{H}_T, \tau)$ for hadronic taus $\tau_h$ (black triangles) and the real-tau prediction with muons $\tau(\mu)$ (green line). The distributions are shown for $W$-boson (upper row) and $t\bar{t}$ (lower row) events, divided for muons coming directly from a $W$-boson decay (left) and muons being produced in a leptonic tau decay (right). They were normalized to one in order to compare the shape.

| Samples | L=1 fb$^{-1}$ | | | Simulated statistics | |
|---|---|---|---|---|---|
| | Selected | Predicted | Muon | Tau | Muon |
| $Z \to ll$ + Jets | $0.2 \pm 0.1$ | $0.1 \pm 0.1$ | 0.1 | 2 | 4 |
| $WW \to l\nu l\nu$ + Jets | $0.1 \pm 0.1$ | $0.3 \pm 0.1$ | 0.4 | 3 | 38 |
| $t\bar{t}$ | $0.3 \pm 0.1$ | $0.6 \pm 0.1$ | 0.9 | 7 | 113 |
| $W \to l\nu$ | $5.8 \pm 1.5$ | $7.0 \pm 1.2$ | 10.8 | 15 | 83 |
| Sum | $6.4 \pm 1.5$ | $7.9 \pm 1.2$ | 12.2 | 27 | 238 |

Table 8.2: Event yield expected from different Standard Model processes for the real-tau estimate at a luminosity of 1 fb$^{-1}$ in the Full selection. See table 8.1 for details.

### 8.1.1 Estimate of Real-Tau Background in the presence of Supersymmetry

While in the Standard Model muons are produced as often as taus, and therefore can be used as a proxy to estimate the background, this is not generally true in supersymmetry. The number of muon events and the number of tau events produced at a given benchmark scenario can differ. If muon events are produced, they can contribute to the muon control sample, and then the background estimate not only consists of the event rate predicted by Standard Model events, but also of the event rate predicted by supersymmetry (this will be discussed further in section 9.2.1). To avoid this, an additional cut on

$$\mathrm{M_T} = \sqrt{2 \cdot \not{H}_\mathrm{T}^\mathrm{real} \cdot \mathrm{P}_\mathrm{T}^\mu \cdot (1 - \cos\Delta\Phi)} \tag{8.2}$$

can be introduced, i.e. $\mathrm{M_T} < 100$ GeV. $\mathrm{P}_\mathrm{T}^\mu$ is the transverse momentum of the muon in the event and $\Delta\Phi = \Delta\Phi(\not{H}_\mathrm{T}, \mu)$ is the azimuthal angle between the muon and the missing transverse momentum. Note that $\not{H}_\mathrm{T}^\mathrm{real}$ in this case is not the manipulated $\not{H}_\mathrm{T}$ in the prediction process described above, but the real missing transverse momentum of the event. Standard Model events, especially $W$-boson events, have a tendency of producing low $\mathrm{M_T}$, while supersymmetric events have larger tails (see figure 8.14). The number of Standard Model events removed from the control sample by this cut is estimated by simulation to be 3%. These events are lost to the prediction, and the result has to be scaled up by this number. An additional uncertainty of this 3% will be assumed on the final real-tau estimate in case the $\mathrm{M_T}$ cut is applied.

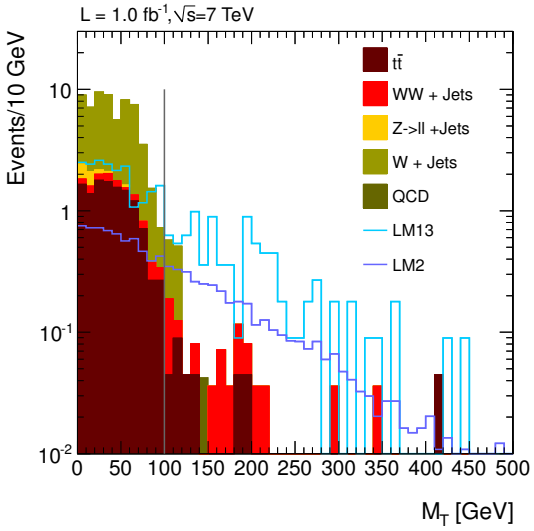


Figure 8.14: $\mathrm{M_T}$ for Standard Model processes (filled space) and supersymmetric events (lines) as predicted by simulated events. The cut on $\mathrm{M_T}$ is indicated with a gray line.

Table 8.3 and 8.4 show the resulting real-tau estimates with $M_T$ cut applied, scaled up by 3%. Note that is case of $WW \to l\nu l\nu$ + Jets events, the number of removed events from the muon control sample is of the order of 30%, and the prediction turns out to be too small in the Base-Line selection. However, as di-boson events are only a small background, and a 100% uncertainty on the $M_T$ cut is assumed, this effect is expected to be covered. Control plots of the real-tau estimate for $W$-boson events with the $M_T$ cut applied can be found in appendix B.
The application of this cut to suppress signal events in the control sample is not generally necessary in the whole supersymmetric parameter space, and depends on the properties of the given benchmark scenario. Also, new physics of other kind is only influenced by this procedure, if large tails beyond $M_T > 100$ GeV are produced.

| Samples | L=1 fb$^{-1}$ | | | Simulated statistics | |
|---|---|---|---|---|---|
| | Selected | Predicted | Muon | Tau | Muon |
| $Z \to ll$ + Jets | $2.2 \pm 0.4$ | $1.7 \pm 0.3$ | 2.6 | 26 | 95 |
| $WW \to l\nu l\nu$ + Jets | $3.0 \pm 0.3$ | $2.2 \pm 0.2$ | 3.3 | 84 | 281 |
| $t\bar{t}$ | $12.1 \pm 0.7$ | $12.3 \pm 0.4$ | 19.0 | 272 | 2026 |
| $W \to l\nu$ | $90.5 \pm 5.9$ | $87.8 \pm 4.1$ | 135.5 | 235 | 1080 |
| Sum | $107.8 \pm 6.0$ | $103.9 \pm 4.2$ | 1340.3 | 617 | 3482 |

Table 8.3: Event yield expected from different Standard Model processes for the real-tau estimate with $M_T < 100$ GeV applied at a luminosity of 1 fb$^{-1}$ in the Base-Line selection. The selected events having the reconstructed tau matched to a tau at generator level. The predicted events are derived by the template method. Also shown for illustration are the number of muon events expected for 1 fb$^{-1}$, as well as the number of simulated events in the muon sample as well as in the tau sample. The predicted number of events has been scaled up by 3%.

| Samples | L=1 fb$^{-1}$ | | | Simulated statistics | |
|---|---|---|---|---|---|
| | Selected | Predicted | Muon | Tau | Muon |
| $Z \to ll$ + Jets | $0.2 \pm 0.1$ | $0.1 \pm 0.1$ | 0.1 | 2 | 4 |
| $WW \to l\nu l\nu$ + Jets | $0.1 \pm 0.1$ | $0.2 \pm 0.1$ | 0.3 | 3 | 26 |
| $t\bar{t}$ | $0.3 \pm 0.1$ | $0.6 \pm 0.1$ | 0.9 | 7 | 104 |
| $W \to l\nu$ | $5.8 \pm 1.5$ | $6.6 \pm 1.1$ | 10.1 | 15 | 80 |
| Sum | $6.4 \pm 1.5$ | $7.4 \pm 1.1$ | 82.4 | 27 | 214 |

Table 8.4: Event yield expected from different Standard Model processes for the real-tau estimate with $M_T < 100$ GeV applied at a luminosity of 1 fb$^{-1}$ in the Full selection. See table 8.3 for details.

## 8.2 Estimate of Fake-Tau Background

To estimate the background induced by mis-identified jets and to test the method, the following steps are taken:

- Measurement of the fake rate in a QCD dominated region.
- Make a closure test in simulation: apply the fake rate to all jets in a control sample to estimate the fake tau background in simulated QCD events.
- Make a closure test in data: define control and tau region in events with lower $\not{H}_T$ with expected QCD domination, and repeat the closure method from step two.

In this chapter, an object named as a jet is not only defined like in section 7.1, but also has to fulfill additional requirements. A minimum quality cut of $P_T > 5$ GeV and $|\eta| < 2.5$ on the jets are applied. The jet is dropped if no tau candidate in $\Delta R < 0.1$ is found (see section 6.3). This tau candidate has to have at least $P_T > 15$ GeV and $|\eta| < 2.1$, to select jets which have already a possibility to fake a tau[2]. Only jets passing these criteria are used to measure the fake rate, as well as making the prediction in the end.
The fake rate, depending on $\eta$ and $P_T$ of the jets, is obtained from an event sample with $H_T > 350$ GeV and $40 < \not{H}_T < 60$ GeV. In this selection, the fraction of QCD events is expected by simulation to be 99%. On the other hand, missing transverse energy due to jet mis-measurement and heavy flavour decays is not suppressed. This sample is used to obtain a ratio between jets and jets faking a tau. It is not used to gain information about the number of events at a certain luminosity. Thus, it is not necessary to have a fully efficient trigger, and the offline threshold cut was set to be $H_T > 350$ GeV. Various prescales are applied to this trigger. However, as the trigger threshold does not change over the full luminosity range, the events are not weighted according to the prescale, to avoid high weights. The resulting fake rates are shown in figure 8.15, in comparison to simulated fake rates. The latter are calculated in the same event region, but have the additional requirement of having at least 100 GeV momentum transfer on generator level, again to avoid large individual event weighting factors.

For the closure tests, the fake rates $f_i$ of jet $i$ are used as individual events weights in the following form:

$$f_{event}^{corr} = 1 - \prod_i (1 - f_i), \tag{8.3}$$

where the product runs over the number of jets fulfilling the requirements stated above in each event. $f_i = f_i(P_T^i, \eta^i)$ is the fake rate depending on the jet $P_T^i$ and $\eta^i$ and $(1 - f_i)$ is the probability of a jet not faking a tau.
The closure test for the Base-Line and Full selection in simulation is shown in detail in table 8.5 and 8.6, with the additional contribution of the non-QCD Standard Model

[2]The transverse momentum of the tau candidate is not necessarily the same as the transverse momentum of the jet, and is usually smaller. The cut on the $P_T$ of the jet is used only for quality control.

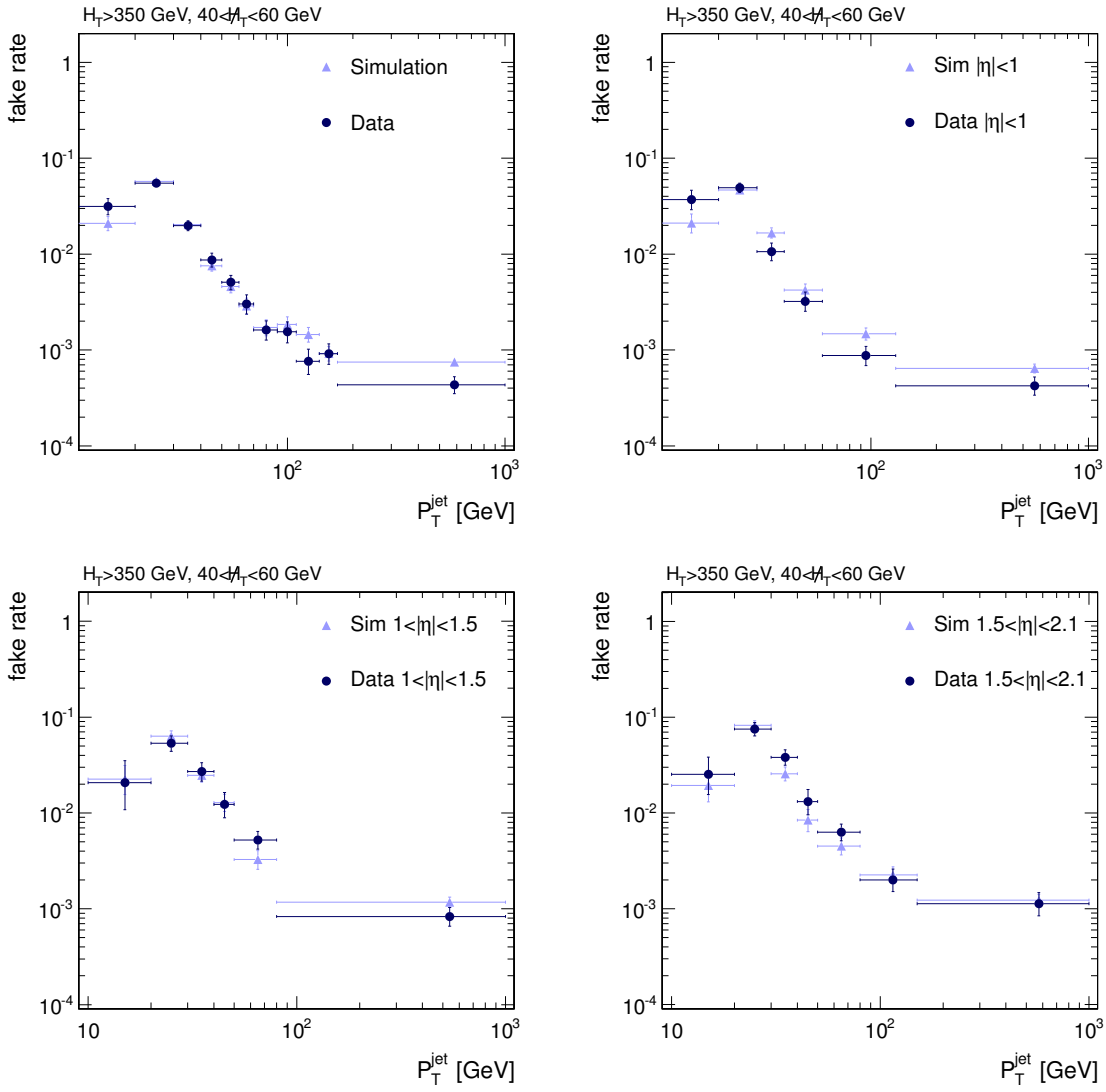


Figure 8.15: Tau reconstruction fake rates for simulation (blue triangles) and data (dark dots) for events with $H_T > 350$ GeV and $40 < \not{H}_T < 60$ GeV. The upper left plot shows the dependence of the fake rate with respect to the $P_T$ of the jet. The other three plots show the same for different exclusive $\eta$ bins.

backgrounds. The statistical fluctuation of the QCD sample is composed of the number of selected simulated events, as well as their individual event weights. Despite the fact that the fake rates where determined from QCD simulation, and a difference between fake rates of gluon-jets and quark-jets have been observed (see [101]), and the small presence of real taus in the veto-tau sample due to non-identification, the prediction for background other than QCD is reasonable good. An exception is $Z \to \nu\nu$ + Jets events. Here, the

method shows a discrepancy between the prediction and the selection of about $\sim 3.5\ \sigma$. For the sum of all contributions, it is a 5% difference, which will be treated as systematic uncertainty.

| Samples | L=1 fb$^{-1}$ | | | Simulated statistics | |
|---|---|---|---|---|---|
| | Selected | Predicted | !Tau | Tau | !Tau |
| QCD | $11.9 \pm 2.6$ | $9.6 \pm 0.5$ | 1654.6 | 74 | 12048 |
| $Z \to \nu\nu$ + Jets | $3.5 \pm 0.2$ | $2.98 \pm 0.03$ | 571.4 | 324 | 53234 |
| $Z \to ll$ + Jets | $0.1 \pm 0.1$ | $0.14 \pm 0.03$ | 8.0 | 1 | 95 |
| $WW \to l\nu l\nu$ + Jets | $0.04 \pm 0.04$ | $0.11 \pm 0.01$ | 9.2 | 1 | 256 |
| $t\bar{t}$ | $2.2 \pm 0.3$ | $2.1 \pm 0.1$ | 126.9 | 50 | 2847 |
| $W \to l\nu$ | $4.2 \pm 1.3$ | $5.4 \pm 0.3$ | 492.7 | 11 | 1280 |
| Sum | $22.0 \pm 2.9$ | $20.3 \pm 0.6$ | 2862.8 | 461 | 69760 |

Table 8.5: Contributions of Standard Model background to the fake-tau estimate at a luminosity of 1 fb$^{-1}$ for the Base-Line selection. The selected events are the events passing the selection and, in addition, having no match of the reconstructed tau with a generated tau. Also shown are the number of events in the control sample (!Tau) expected by simulation for 1 fb$^{-1}$, and the number of simulated events used in both the tau and the control sample.

| Samples | L=1 fb$^{-1}$ | | | Simulated statistics | |
|---|---|---|---|---|---|
| | Selected | Predicted | !Tau | Tau | !Tau |
| QCD | $1.91 \pm 1.13$ | $0.79 \pm 0.07$ | 136.4 | 21 | 3294 |
| $Z \to \nu\nu$ + Jets | $0.25 \pm 0.05$ | $0.21 \pm 0.01$ | 38.0 | 23 | 3544 |
| $Z \to ll$ + Jets | $- \pm -$ | $0.003 \pm 0.002$ | 0.4 | 0 | 5 |
| $WW \to l\nu l\nu$ + Jets | $- \pm -$ | $0.006 \pm 0.002$ | 0.9 | 0 | 24 |
| $t\bar{t}$ | $0.04 \pm 0.04$ | $0.12 \pm 0.02$ | 8.2 | 1 | 184 |
| $W \to l\nu$ | $0.38 \pm 0.38$ | $0.34 \pm 0.08$ | 33.9 | 1 | 88 |
| Sum | $2.59 \pm 1.2$ | $1.47 \pm 0.1$ | 217.8 | 46 | 7139 |

Table 8.6: Contributions of Standard Model background to the fake-tau estimate at a luminosity of 1 fb$^{-1}$ for the Full selection. For details, see table 8.5.

The fake-tau estimation method focuses at predicting QCD, as it is the main source of fake-taus. Thus, for a closure test, the control distributions for this background are especially interesting. They are shown for the Base-Line selection in figure 8.16, 8.17, 8.18, and 8.19, respectively. The selected events are indicated with black triangles, the blue filled region gives the predicted events, and the hatched areas indicate the uncertainty.

These are composed of the statistical uncertainty on the sample used for the prediction, and the uncertainty on the event weight build up by the fake rates. For $H_T$ and $\not{H}_T$, the tau and jet kinematics, and the angular distributions, the prediction agrees reasonable well with the selection, although some fluctuations can be seen and the uncertainties are large. $\not{H}_T$ shows an exponential decrease, as expected, for the main source of missing transverse momentum in QCD events is coming from the Gaussian distributed mis-measurement of jets. The azimuthal angle $\Delta\Phi$ between the $\not{H}_T$ and the tau is approximately flat, leading to the conclusion that there is no correlation between the mismeasurement of jets leading to missing transverse momentum, and the mis-identification of a jet as a tau. The minimal azimuthal angle of the $\not{H}_T$ with one of the three leading jets $\min\Delta\Phi(\not{H}_T, jet123)$ peaks at small values, indicating that in $\not{H}_T$ production, single jet fluctuations dominate. In addition, the azimuthal angle between the first two leading jets, $\Delta\Phi(jet1, jet2)$ shows a preference of large values, as expected for a QCD sample mainly composed of di-jet events.

The prediction was also tested in data events. For this, two different $\not{H}_T$ regions were selected. Each of these regions have the $H_T > 350(600)$ GeV cut applied, and the $\not{H}_T$ is exclusively binned: 60-80 GeV, and 80-100 GeV, respectively. Each of this regions is dominated by QCD which contributes more than 90%. The prediction is made then for each of these regions with the fake rate obtained from the $40 < \not{H}_T < 60$ GeV sample, for the prediction in data on data events, and for the prediction in QCD simulation in simulated events. The results for both data and simulation, as well as the fraction of QCD are shown in table 8.7. For the simulated events, the events stated as "selected" are events passing the corresponding selection, but in addition have the tau candidate not matched to a generator level tau. In addition, the results in simulated events for the Base-Line and Full selections are shown. The results for both data and simulation are compatible with unity. They are stable over the $\not{H}_T$ range tested. This is also true for the Base-Line and Full selection, although the uncertainties are large. The systematic uncertainty of the fake rate method was taken from two closure test regions: the region with $60 < \not{H}_T < 80$ GeV and the region with $80 < \not{H}_T < 100$ GeV, where both samples also satisfy $H_T > 600$ GeV. The high $H_T$ region was chosen, as the fake rate is dependent on the number of jets in the event, and $H_T$ and the number of jets are expected to be correlated. The weighted average of both scaling factors selected/predicted is $1.07 \pm 0.21$, leading to 21% uncertainty of the method.

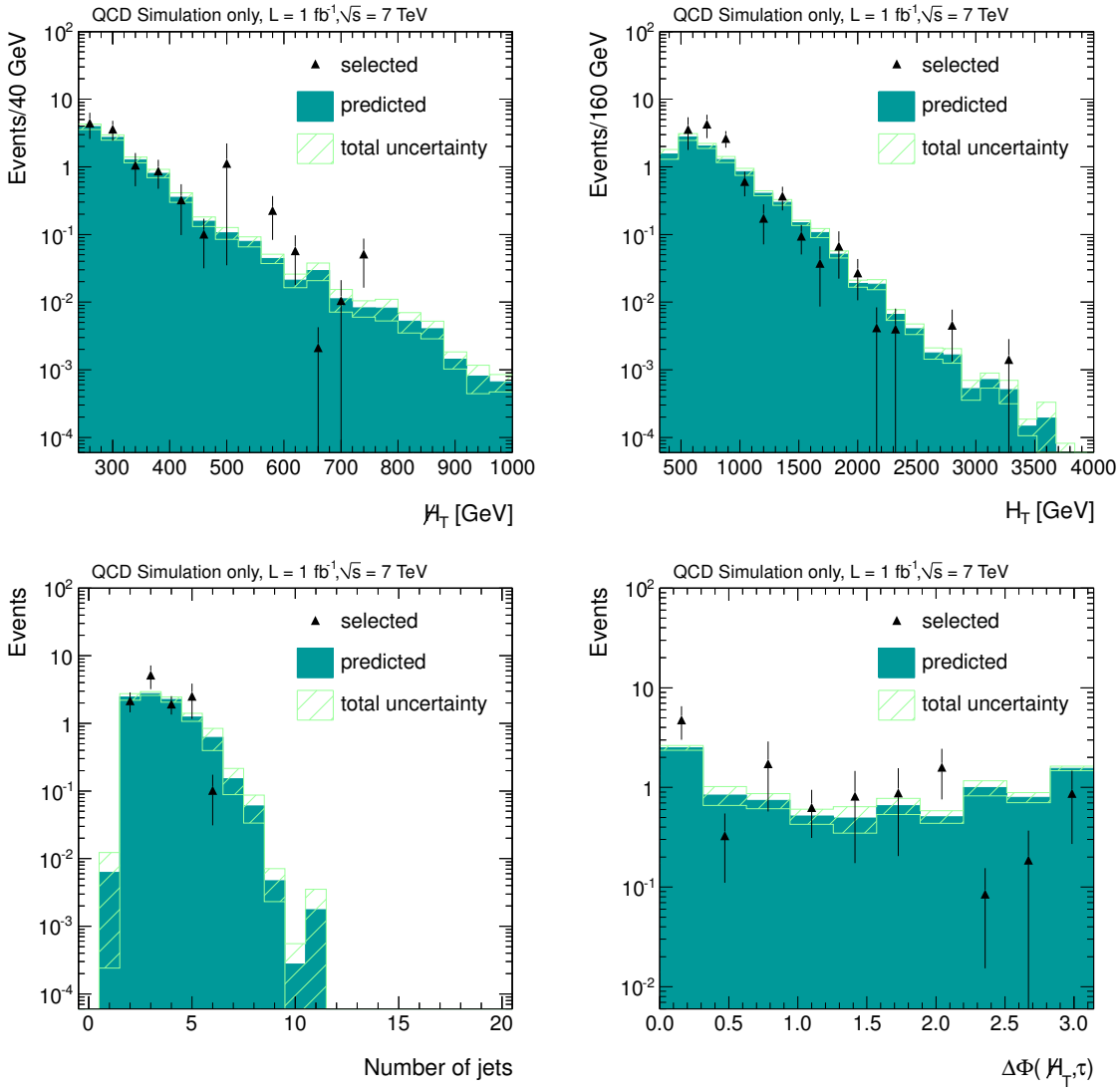


Figure 8.16: $H_T$ and $\not{H}_T$ (upper row), and number of Jets with $P_T > 30$ GeV and $\Delta\Phi(\not{H}_T, \tau)$ (lower row) distributions for the fake-tau estimate in simulated events in the Base-Line selection. The black triangles are the events passing the selection, the filled blue area gives the predicted events. The hatched area are the uncertainties, composed of the statistical uncertainty of the sample as well as the systematic uncertainty coming from the statistical uncertainty of the fake rates.

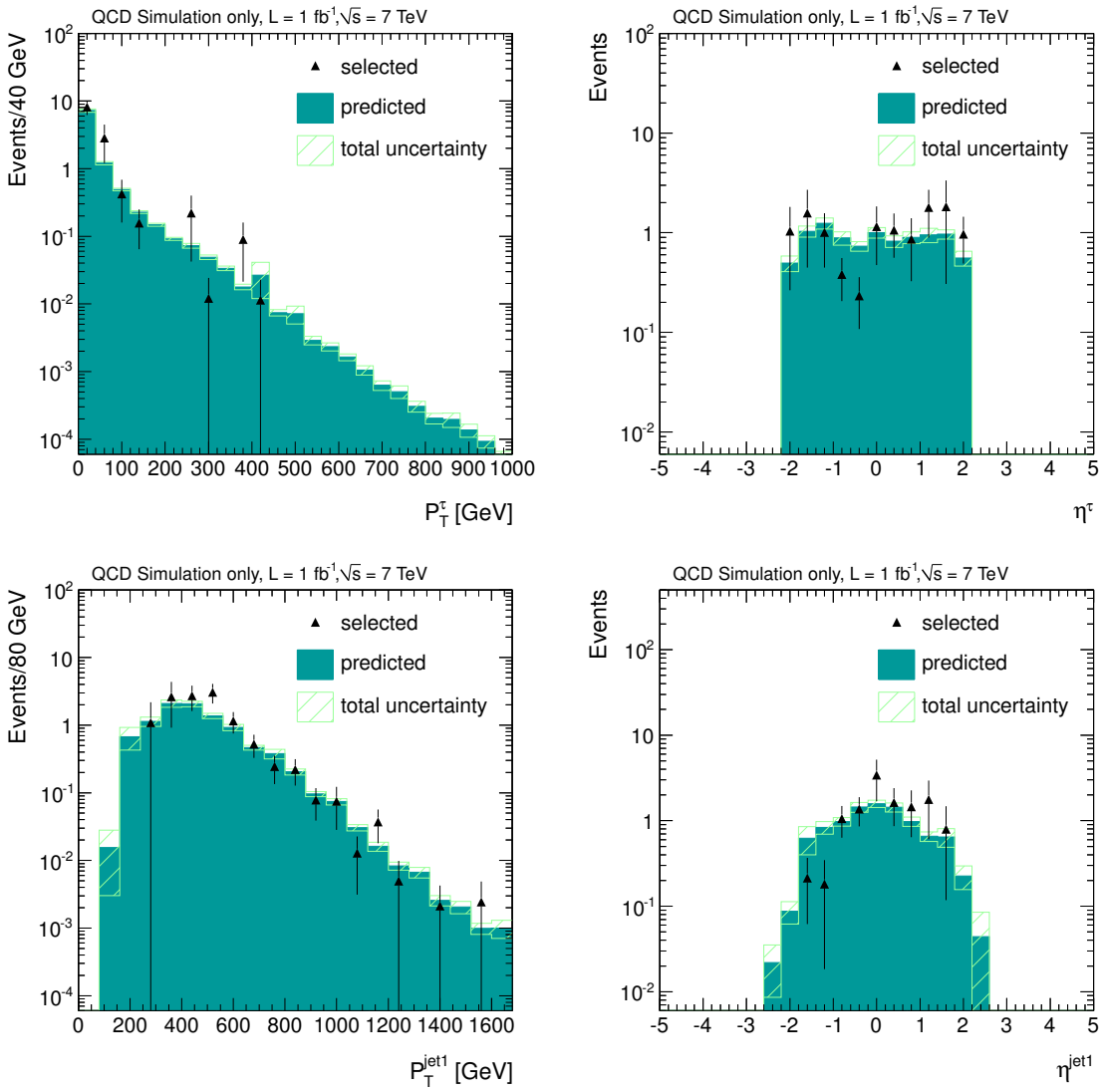


Figure 8.17: $P_T$ and $\eta$ of the tau (upper row), and the leading jet in case of $P_T^{jet} > 30$ GeV(lower row) for the fake-tau estimate in simulated events in the Base-Line selection. For details, see figure 8.16.

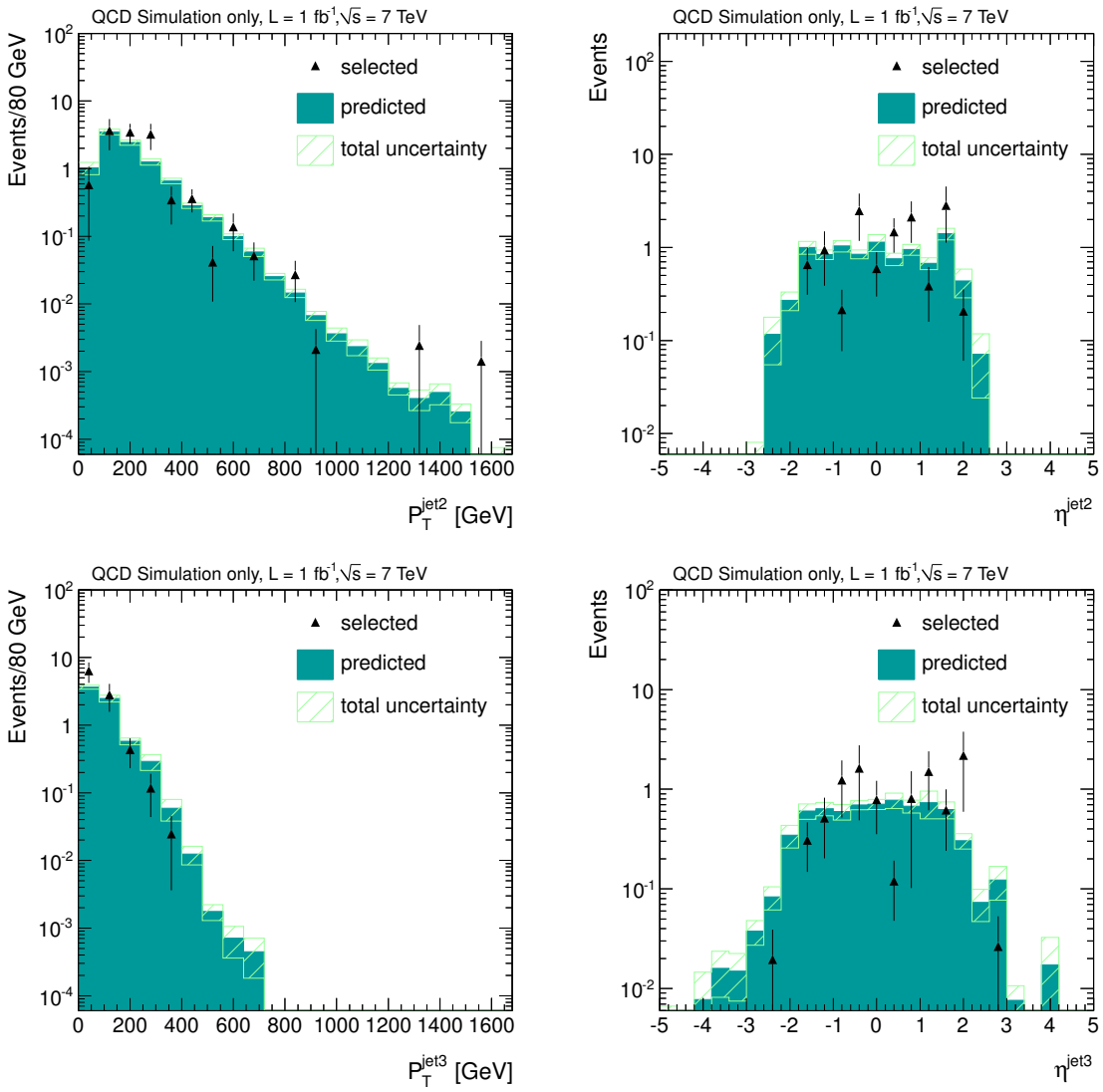


Figure 8.18: $P_T$ and $\eta$ of the second (upper row), and the third leading jet (lower row) in case of $P_T^{jet} > 30$ GeV for the fake-tau estimate in simulated events in the Base-Line selection. For details, see figure 8.16.

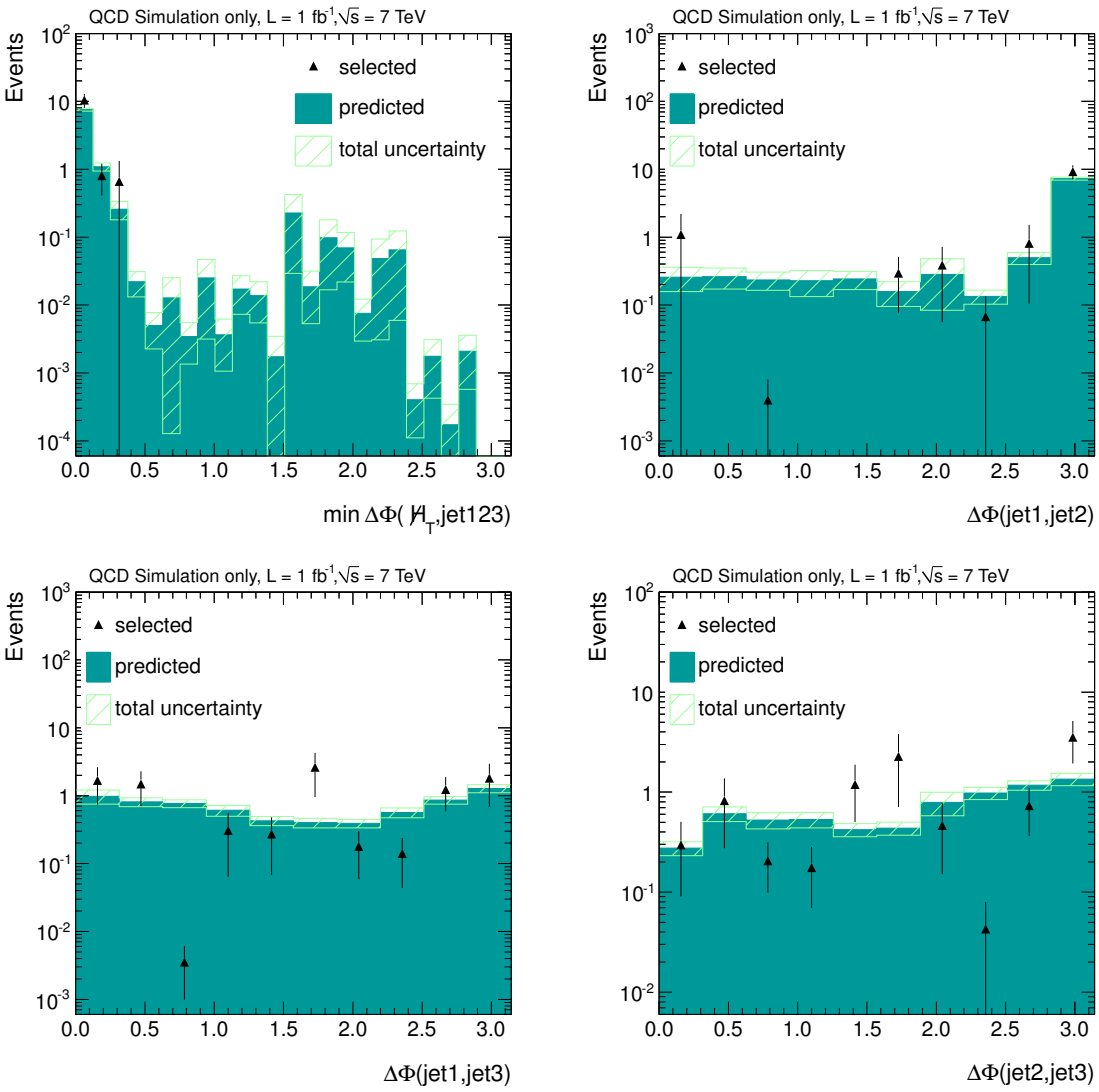


Figure 8.19: min$\Delta\Phi(\not{H}_T, jet123)$ and $\Delta\Phi(jet1, jet2)$ (upper row), and $\Delta\Phi(jet1, jet3)$ and $\Delta\Phi(jet2, jet3)$ (lower row) for the fake-tau estimate in simulated events in the Base-Line selection. The used jets have at least 30 GeV of $P_T$. For details, see figure 8.16.

| | $\not{H}_T$ [GeV] | | |
|---|---|---|---|
| $H_T > 350$ GeV | 60-80 | 80-100 | $> 250$ |
| QCD fraction | 97% | 93% | 6% |
| selected/predicted (sim) | $0.98 \pm 0.06$ | $0.96 \pm 0.07$ | $1.24 \pm 0.28$ |
| selected/predicted (data) | $1.01 \pm 0.08$ | $0.88 \pm 0.13$ | – |
| $H_T > 600$ GeV | | | $> 400$ |
| QCD fraction | 96% | 93% | 17% |
| selected/predicted (sim) | $0.94 \pm 0.09$ | $0.85 \pm 0.09$ | $2.43 \pm 1.45$ |
| selected/predicted (data) | $1.14 \pm 0.26$ | $0.97 \pm 0.37$ | – |

Table 8.7: Test of the fake rate method in different QCD dominated regions. Shown is the QCD fraction of the individual $\not{H}_T$ samples, as well as the fraction of selected over predicted events obtained in that region for both data and simulation (QCD only). Also displayed is the result for simulated events in the signal region. The uncertainties are the statistical uncertainties of the selected and predicted sample, as well as the uncertainty coming from the statistical uncertainty of the fake rates.

## 8.3 Uncertainties

In addition to the statistical uncertainty on the measurement $\sqrt{N_{meas}}$, systematic uncertainties may arise. Possible sources are biases in the measurement, theoretical uncertainties on the assumed model, or statistical fluctuations of applied weighting factors. Both statistical as well as systematic uncertainties have to be examined in order to evaluate possible deviations from the prediction of the Standard Model.

### 8.3.1 Systematic Uncertainties

Statistical uncertainties on weighting factors are propagated to the prediction in varying the corresponding factor by its uncertainty. Each bin of each weighting factor is propagated independently, and in the end summed up quadratically with the other bins, as the statistical uncertainty in each bin is independent from the others, and therefore uncorrelated. A summary of the discussed systematic uncertainties can be found in table 8.8.
Global uncertainties considered are:

- **Light Lepton Fakes**: Prompt light leptons $(e, \mu)$ that are missed by the global event lepton veto as well as the electron and muon discriminators of the tau identification (see section 6.3) are sources for tau fakes, as electrons and muons can easily be misidentified as one-prong taus. The number of events passing the selections with a light lepton faking the identified tau has been estimated in simulation to be 1% of all selected events.

#### Real-Tau Estimate

The following systematic uncertainties specific to the prediction of real tau events have been identified:

- $t\bar{t}$ **contribution**: $t\bar{t}$ events in the muon control sample used for the prediction are predicted well for the Base-Line selection, and lead to an overprediction of 4% in the Full selection.

- **Statistics of the muon sample**: The number of muon events has a statistical uncertainty, which translates to a systematic uncertainty of the prediction. It has been found to be 3% for the Base-Line and 10% for the Full selection at 5 $\text{fb}^{-1}$.

- **Tau reconstruction efficiency**: The tau reconstruction efficiency is taken from simulation. Simulation has shown to represent data well, with an uncertainty of 7% (see section 6.3.5). In addition, the statistical uncertainties on to the number of simulated events used propagate to a prediction uncertainty of 2% for the Base-Line and 3% for the Full selection.

- **Correction for muons from tau decay**: The number of muons is taken from simulated $W$ plus jets events, binned in $\text{P}_\text{T}$ of the muon. The statistical uncertainty

on this quantity propagates to a prediction uncertainty of 1% for the Base-Line and Full selection.

- **Trigger inefficiency due to muon smearing**: For the estimate, muon events are selected after the offline cut on the $\not{H}_T$ trigger is placed. Then, the muon, and thus, the $\not{H}_T$, is manipulated. In principle, events not passing the $\not{H}_T$ selection can fulfill the cut on the manipulated $\not{H}_T$ afterward because of the added smeared muon. Due to the trigger cut, these kind of events are not available for the prediction. The fraction of these events has been estimated in simulation to be about 1% in the Base-Line selection. Due to the increased $\not{H}_T$ cut the Full selection does not include these kind of events.

- **Muon reconstruction and isolation efficiencies**: The muon reconstruction and isolation efficiencies have been taken from fits on $Z$ plus jets events in data. The uncertainties on the fits are propagated to prediction uncertainties of 0.2% for the isolation and less than 0.1% for the reconstruction efficiency .

- **Hadronic Branching Fraction**: The uncertainty for a decay of a tau into a light lepton is 0.04% for both muon and electron [8].

- **Stability of the method against Pile-Up**: The stability of the method against Pile-Up has been tested in simulation. For this, the closure test has been done where both the muon as well as the tau sample were restricted to events with few vertices ($n_{vertex} < 6$). A second test was done where the number of vertices was required to be high ($n_{vertex} \geqslant 10$). In both cases, the number of selected tau events was well predicted by the method. Hence, no uncertainty due to Pile-Up has been applied.

- **Template Statistics**: In principle, the statistical fluctuations of the template is another source of systematic uncertainty. As the template was produced of the full simulated $W$-boson sample, which statistic is of orders of magnitude higher than the number of data events finally used for the prediction, the resulting systematic uncertainty is very small compared to the statistical uncertainty of the data. Thus, no additional uncertainty has been applied.

- $M_T$ **cut**: In case the $M_T$ cut is applied on the muon events of the control sample, the resulting prediction has to be scaled. The additional uncertainty is then 3%.

**Fake-Tau Estimate**

Systematic uncertainties specific to the fake tau estimate are the following:

- **Fake Rate**: The fake rate per jet is obtained on data events. The corresponding statistical variations lead to an uncertainty of 2% for the Base-Line, and 3% upwards and 2% downwards for the Full selection.

- **Method uncertainty**: The method uncertainty was estimated to be 21%, as discussed in section 8.2.
- $Z \to \nu\nu$ **+ Jets contribution**: The presence $Z \to \nu\nu$ + Jets events is accounted for with 5% uncertainty.
- **Pile-Up stability**: Similar to the Real Tau method, the influence of Pile-Up has been tested on simulation. Again it has been found that selected events with few (high) number of vertices are well described by the prediction made with events with few (high) number of vertices. Thus, no uncertainty due to Pile-Up has been applied.
- **Statistics of the Non-tau sample**: The statistical uncertainty of the sample used for the fake rate method leads to an uncertainty of 2% for the Base-Line, and 12% for the Full selection.

| | Base-Line | Full |
|---|---|---|
| Statistical uncertainty on selection | 5% | 19% |
| | Uncertainties in Real-Tau Estimate | |
| $M_T$ cut | 3% | |
| Pile-Up | 0% | |
| Tau Template statistics | 0% | |
| Muon reconstruction efficiency | $< 1\%$ | |
| Muon isolation efficiency | $< 1\%$ | |
| Correction on muons from tau decay | 1% | |
| Tau hadronic branching fraction | $< 1\%$ | |
| Tau $\epsilon_\tau^{reco}$ (Data/Sim) | 7% | |
| Tau $\epsilon_\tau^{reco}$ (stat. uncertainties) | 2% | 3% |
| $t\bar{t}$ contribution | 0% | 4% |
| Trigger inefficiency due to muon smearing | 1% | 0% |
| Statistical uncertainty of muon sample | 3% | 10% |
| | Uncertainties in Fake-Tau Estimate | |
| Pile-Up | 0% | |
| Method uncertainty | 21% | |
| $Z \to \nu\nu$ + Jets contribution | 5% | |
| Tau fake rate (stat. uncertainties) | 2% | 3% |
| Statistical uncertainty of control sample | 2% | 12% |
| | Additional uncertainties | |
| Tau fake rate (light leptons) | 1% | |
| Combined Syst. uncertainty | 8% | 12% |

Table 8.8: Summary of the uncertainties specific to the two different background estimates, as well as the combination. Note that for the case of the application of the $M_T$ cut, the statistical uncertainty of the muon sample and the final combined systematic uncertainty does not change.

# Chapter 9

# Results

## 9.1 Kinematic Distributions

The analysis has been performed on 5 $fb^{-1}$ of CMS data. Both the estimate of background containing a real tau, as well as background containing a fake tau was performed on data. The only components coming from simulation were the tau $P_T$ response, the reconstruction efficiency of the tau and the probability of the muon being from a tau decay. As this analysis focuses on the search for supersymmetry, the results shown here are for the $M_T$ cut applied on the muon control sample of the real-tau prediction. The prediction for the real-tau background contribution was scaled upwards by 3% as discussed in 8.1.1. The corresponding event yields and control distributions for the estimate without this cut applied are shown in appendix C.
In the Base-Line Selection, 444 data events have been found, 413 $\pm$ 10 (stat) $\pm$ 31 (syst) were predicted by the real-tau and fake-tau estimates. 28 data events survived the Full selection, compared to 28.5 $\pm$ 2.6 (stat) $\pm$ 2.4 (syst) predicted. The results are summarized in table 9.1. For the fake-tau estimate, 7651 (Base-Line) and 386 (Full) events have been used. For the real-tau estimate, the muon sample consisted of 1762 (Base-Line) and 119 (Full) events. The number of data events in both selections are well described by the prediction within the uncertainties. No deviation from the Standard Model has been observed.
The figures 9.1, 9.2, 9.3, and 9.4 show some control distributions of data and the two background predictions. For illustration, two additional signal samples, LM2 and LM13 (see section 2.2.1) are shown.
Again $H_T$, $\not{H}_T$, and the number of jets with $P_T > 30$ GeV are reasonably well described within the uncertainties. The azimuthal angle between the $\not{H}_T$ and the tau $\Delta\Phi(\not{H}_T, \tau)$ shows some disagreement between data events and the corresponding prediction. This has already been observed in the simulation closure of the real tau prediction method in case of the presence of muons from tau decays in the event (see section 8.1). The $P_T$ and $\eta$ distributions of the tau as well as the first three leading jets (shown for jets with $P_T > 30$ GeV) agree with the prediction within the uncertainties. Also, the minimal azimuthal

angle between the $\not{H}_T$ and the first three leading jets $\min\Delta\Phi(\not{H}_T, jet(1,2,3))$ as well as the individual angles between these jets $\Delta\Phi(jet1, jet2)$, $\Delta\Phi(jet1, jet3)$, and $\Delta\Phi(jet2, jet3)$ agree reasonable well with the prediction.
Event displays of the five events with the highest $\not{H}_T$ can be found in appendix D.

| 5 fb$^{-1}$ | Base-Line | Full |
|---|---|---|
| Fake-Tau Est. | $67 \pm 2$ (stat) $\pm 15$ (syst) | $3.4 \pm 0.4$ (stat) $\pm 0.7$ (syst) |
| Real-Tau Est. | $346 \pm 9$ (stat) $\pm 28$ (syst) | $25.2 \pm 2.5$ (stat) $\pm 2.3$ (syst) |
| Sum | $413 \pm 10$ (stat) $\pm 31$ (syst) | $28.5 \pm 2.6$ (stat) $\pm 2.4$ (syst) |
| Data | 444 | 28 |

Table 9.1: Event yield and prediction for Base-Line and Full selected events with $M_T < 100$ GeV applied on the muon control sample for 5 fb$^{-1}$ of CMS data.

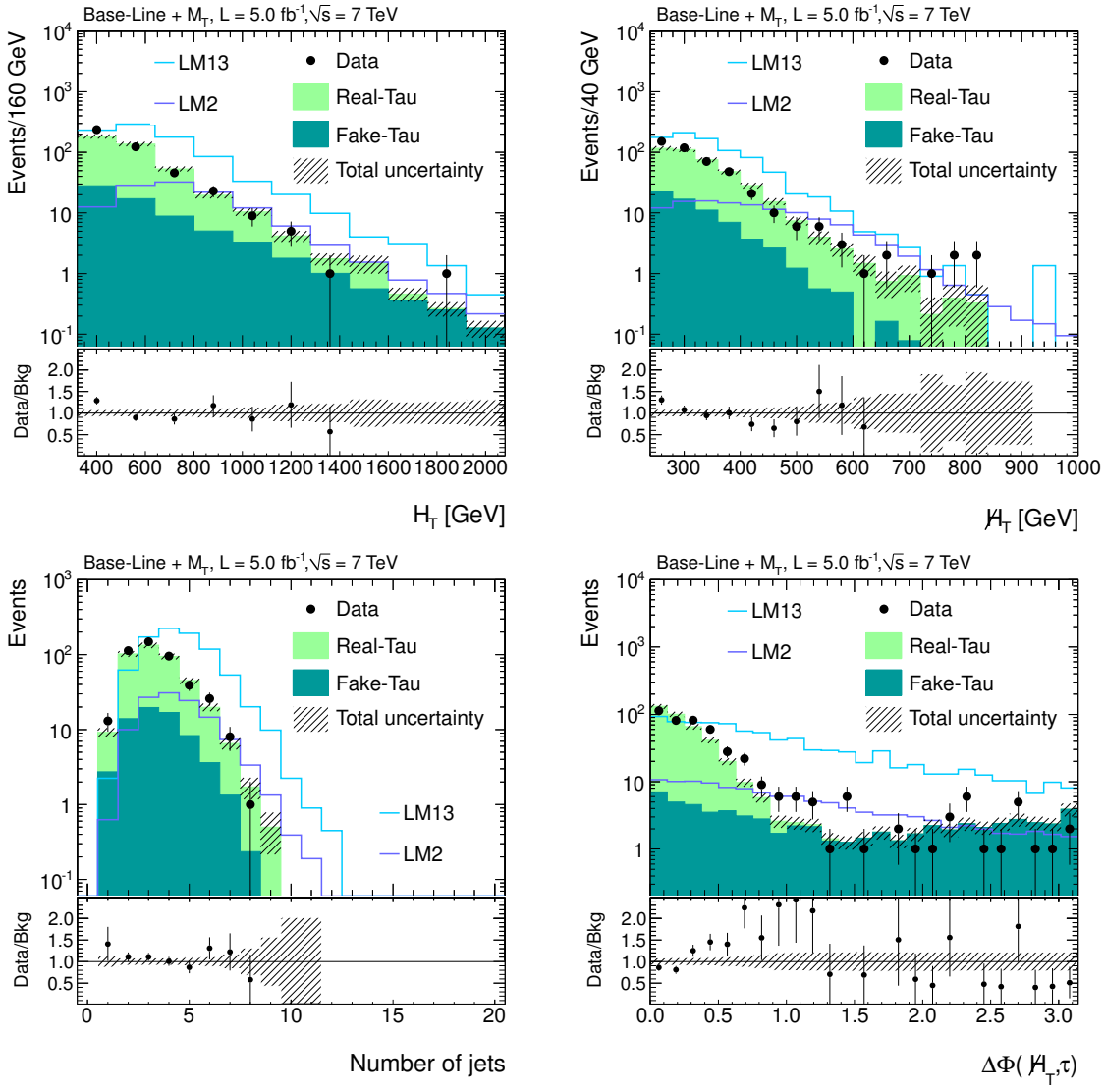


Figure 9.1: $H_T$ and $\not{H}_T$ (upper row), and number of Jets with $P_T > 30$ GeV and $\Delta\Phi(\not{H}_T, \tau)$ (lower row) distributions for 5 fb$^{-1}$ of data. The black dots are the data events passing the Base-Line selection. The filled green (light) area gives the predicted background containing a real tau, the filled blue (dark) area describes the predicted background with fake taus. The hatched area indicates the total uncertainty of the background prediction. The $M_T$ cut has been applied on the muon control sample of the real-tau estimate.

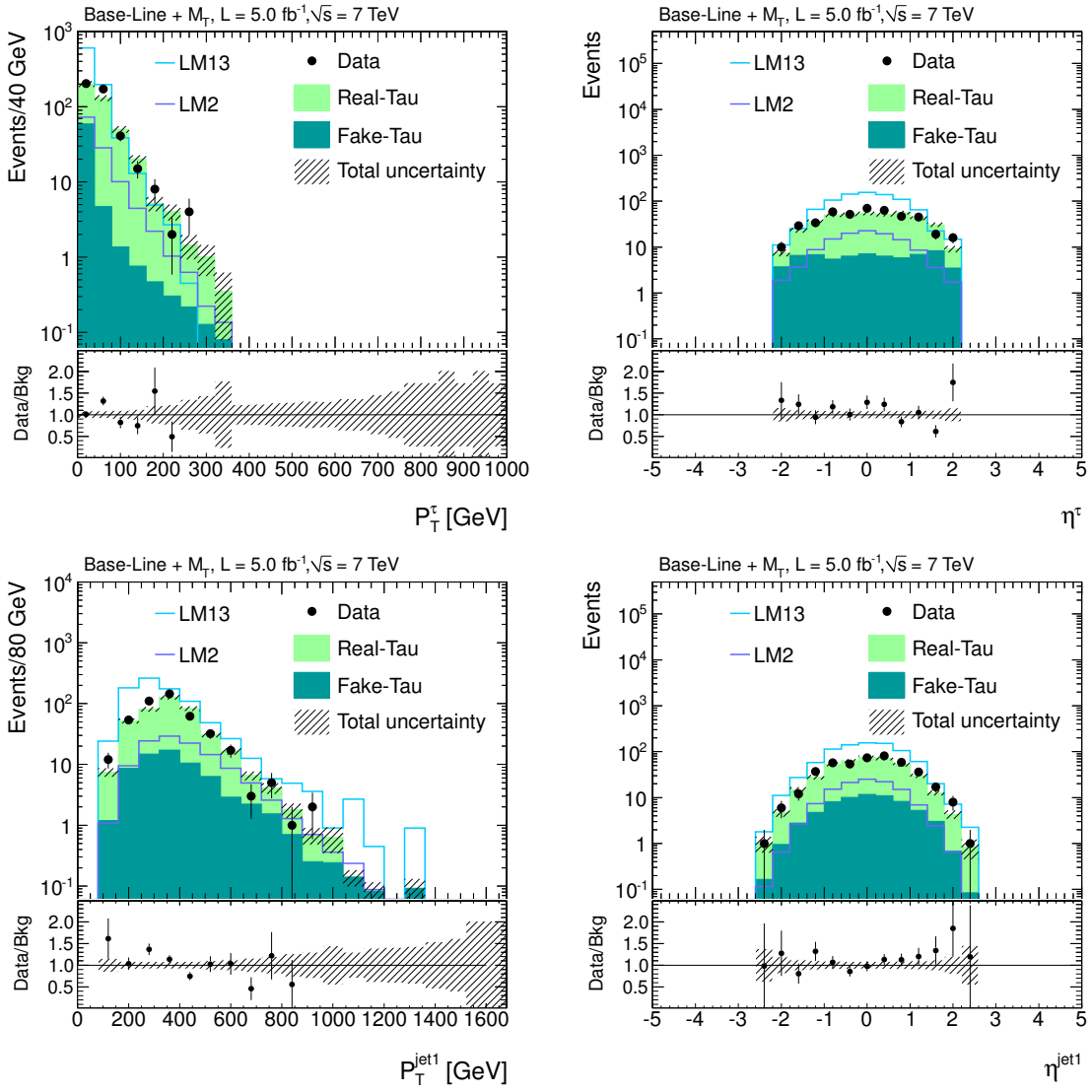


Figure 9.2: $P_T$ and $\eta$ of the tau (upper row), and the leading jet for the case of $P_T^{jet} > 30$ GeV (lower row) for 5 fb$^{-1}$ of data. For details, see figure 9.1.

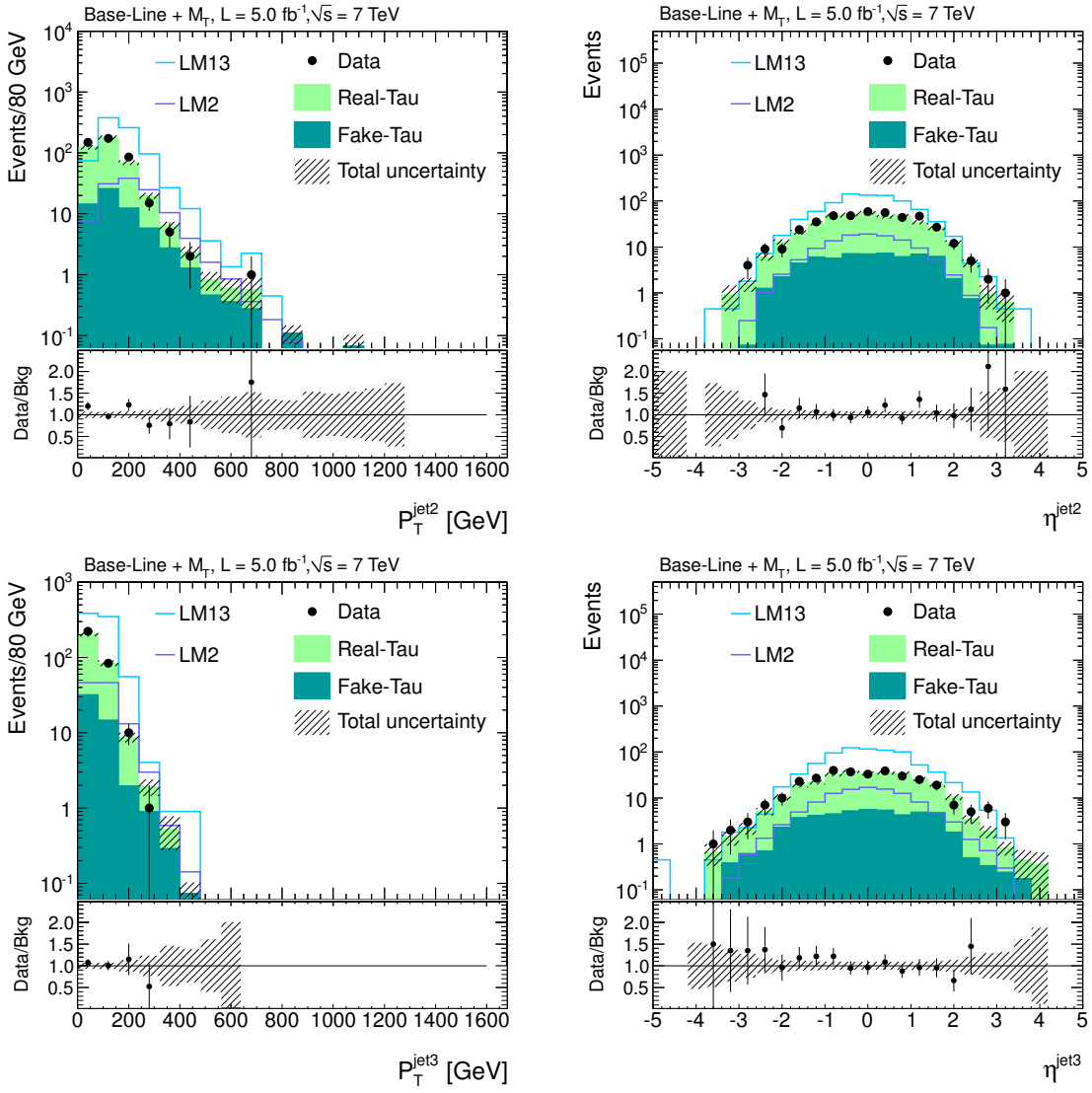


Figure 9.3: $P_T$ and $\eta$ of the second (upper row), and the third leading jet (lower row) in case of $P_T^{jet} > 30$ GeV for 5 fb$^{-1}$ of data. For details, see figure 9.1.

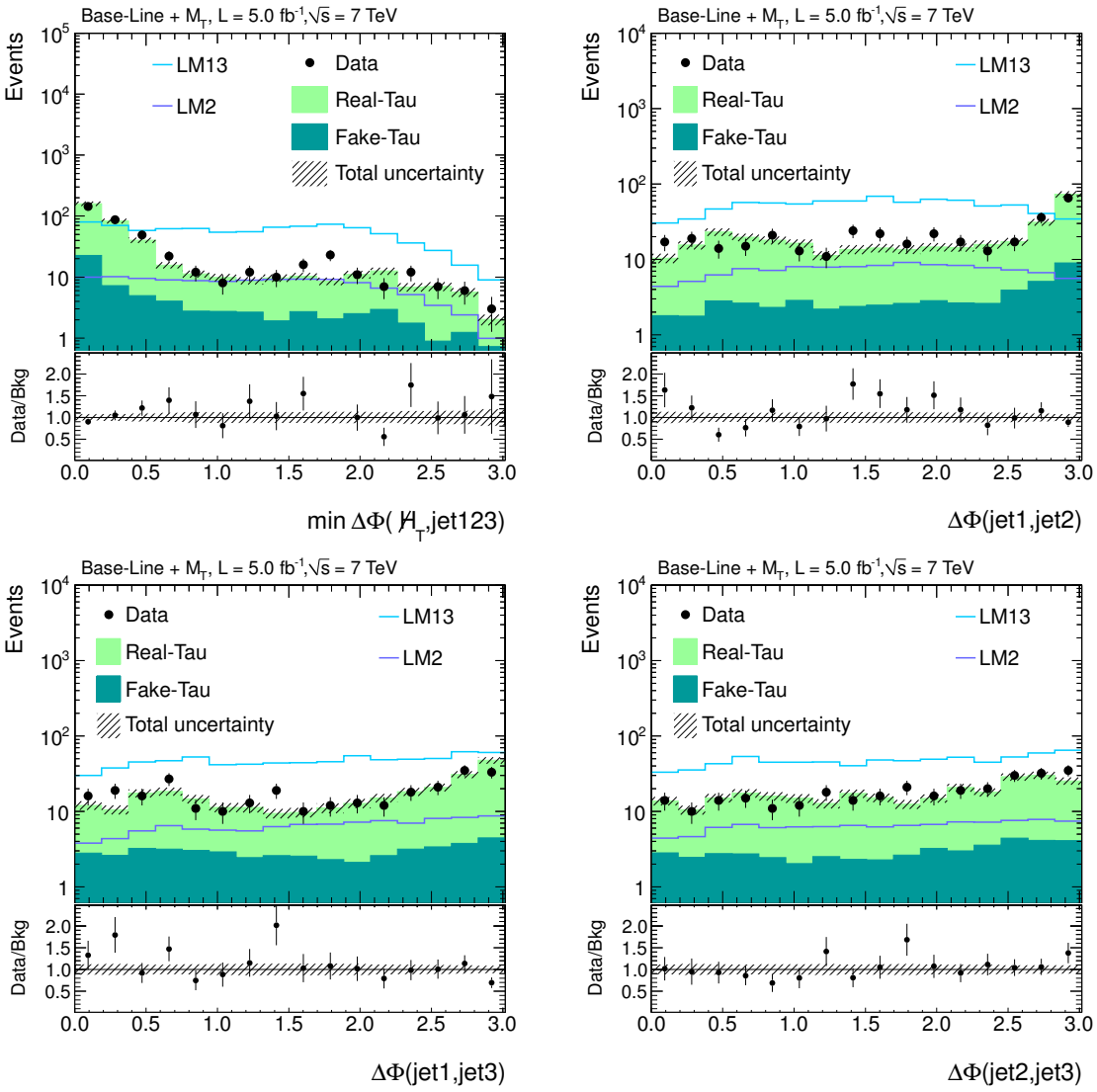


Figure 9.4: Minimal angle between $\not{H}_T$ and the first leading jets $\min\Delta\Phi(\not{H}_T, jet(1,2,3))$ and $\Delta\Phi(jet1, jet2)$ (upper row), and $\Delta\Phi(jet1, jet3)$ and $\Delta\Phi(jet2, jet3)$ (lower row) for 5 fb$^{-1}$ of data. For details, see figure 9.1.

## 9.2 Interpretation of the Result in the cMSSM

No sign of a signal has been found. Thus, exclusion limits for a given model can be set, in this case the cMSSM. The stau-LSP co-annihilation region becomes enhanced at large $\tan\beta$, thus, a scan of the cMSSM with $\tan\beta = 40$ was chosen[1]. This scan of the cMSSM parameter space was defined in $m_0$ and $m_{1/2}$. Each benchmark point consisted of 10000 simulated events (see section 5.1), which were weighted according to realistic Pile-Up taken from data. Only the Full selection has been used to set the limits. The acceptance of a point is then the number of simulated events passing the selection divided by the number of all events simulated. Figure 9.5 shows the resulting acceptance, the NLO cross section, the expected event rate and the number of simulated events surviving the Full selection for each point. Points left white are points where no events were passing the selection, or where no events were simulated at all. The preference of the co-annihilation region can clearly be seen in the signal acceptance, which is of the order of 1-3% in the named region. Depending on the cross section, the number of events predicted by simulation can be of the order of 100 events. For low $m_{1/2}$, the number of selected simulated events is less than 10 events, which leads to large statistical uncertainty in this region.

Note that, as the sensitivity of this search does not allow to probe the entire range of $m_0$ in this scan yet, all following distributions will be shown restricted to $m_0 < 1000$ GeV.

### 9.2.1 Signal Contamination

Ideally, in case a particular benchmark point is realized in nature, the number of events passing the selection, $N^{pass}_{SUSY}$, is the number of events seen experimentally as an excess of data over the background prediction, $N^{exp}_{SUSY}$. However, in general, supersymmetric events will also be present in the control samples of the background estimation method, leading to an additional contribution for the background estimation. In this analysis, depending on the number of single muon events produced in supersymmetric decays, the real-tau background will grow by $N^{real-tau}_{SUSY,cont}$, and, depending on the number of SUSY events in the jets-only control sample, the fake-tau background gets an additional contribution of $N^{fake-tau}_{SUSY,cont}$. This is called the "signal contamination". The final experimentally accessible number of supersymmetric events measured would be then

$$N^{exp}_{SUSY} = N^{pass}_{SUSY} - N^{fake-tau}_{SUSY,cont} - N^{real-tau}_{SUSY,cont}. \tag{9.1}$$

Figure 9.6 shows the signal contamination for fake-tau (left) and real tau (right) background estimation relative to the number of events selected $N^{pass}_{SUSY}$. The co-annihilation region again behaves differently from the other regions. For the fake-tau background, the signal contamination within the co-annihilation region is smaller than 10%, while it is of the order of 20-30% for other regions, because the number of events with taus drops. In

[1]Note that the co-annihilation region is still present at $\tan\beta = 10$, but not as strongly as for large values of $\tan\beta$.

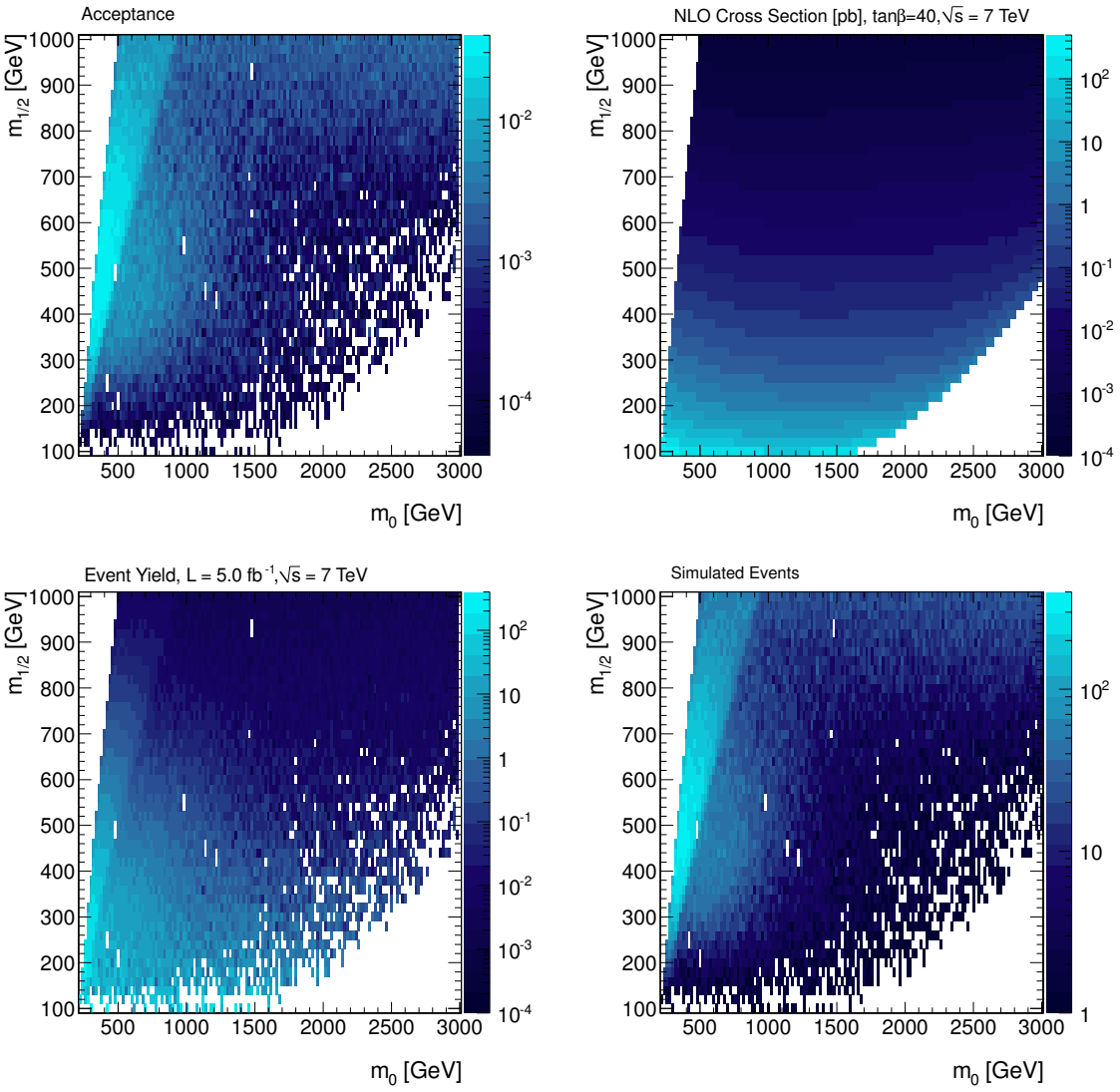


Figure 9.5: Acceptance (upper left), NLO cross section (upper right), event rate $N_{SUSY}^{pass}$ (lower left) and number of simulated events (lower right) for the cMSSM at $\tan\beta = 40$ for the Full selection in the plane of $m_0$ versus $m_{1/2}$.

case of the real-tau estimate, the predicted background due to supersymmetric events in the muon control sample is also less than 10% of the selected events in the co-annihilation region. In other regions, it can be 50% and more, as the number of taus produced decreases and the number of events with muons can increase, meaning that these benchmark scenarios are difficult or impossible to be found by this search, unless the signal contamination in the real-tau estimate is sufficiently suppressed. For this, the cut of the $M_T$ distribution of the muon events was introduced (section 8.1.1). The signal contamination for a real-tau

prediction with $M_T$ cut applied is shown in figure 9.7. It was significantly reduced to a level of $< 10^{-3}$ throughout the entire scan region. Note that the bin size has been increased, as for many benchmark scenarios, no muon events were left within the control sample. Neighboring points were combinded, to give a measure on the relative signal contamination after the $M_T$ cut has been used. The Full selection with this cut applied was used for the limit calculation, to allow for reasonable results also outside of the co-annihilation region.

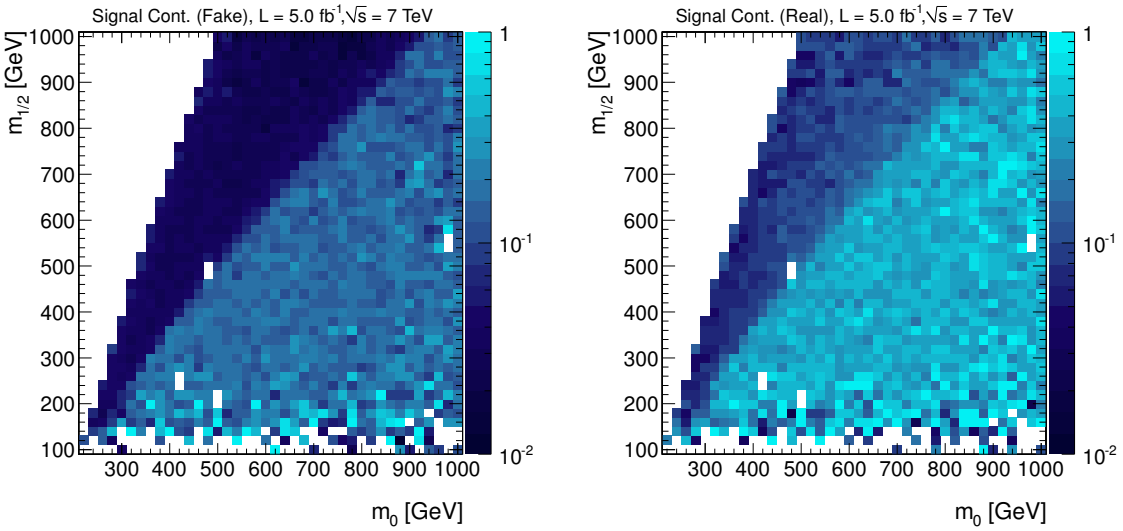


Figure 9.6: Signal Contamination for the fake-tau (left) and the real-tau (right) background estimations relative to the number of selected events $N_{SUSY}^{pass}$.

### 9.2.2 Signal Uncertainties

Secondary to the systematic uncertainties considered for the data-driven background estimate of the selected data events, for the simulated signal events, additional uncertainties have to be taken into account.
The following uncertainties are common for all signal models:

- **Luminosity measurement**: The uncertainty introduced by the luminosity measurement is 2.2%, as found in [102].
- **Trigger Uncertainty**: The trigger uncertainty is found to be 2.5%, according to [97].
- **Missing TAUOLA in Scan Simulation**: The cMSSM scan was not simulated with TAUOLA. This can have an influence, as different polarization states of the tau can have different detector responses. This effect is of the order of 1-2% [103].

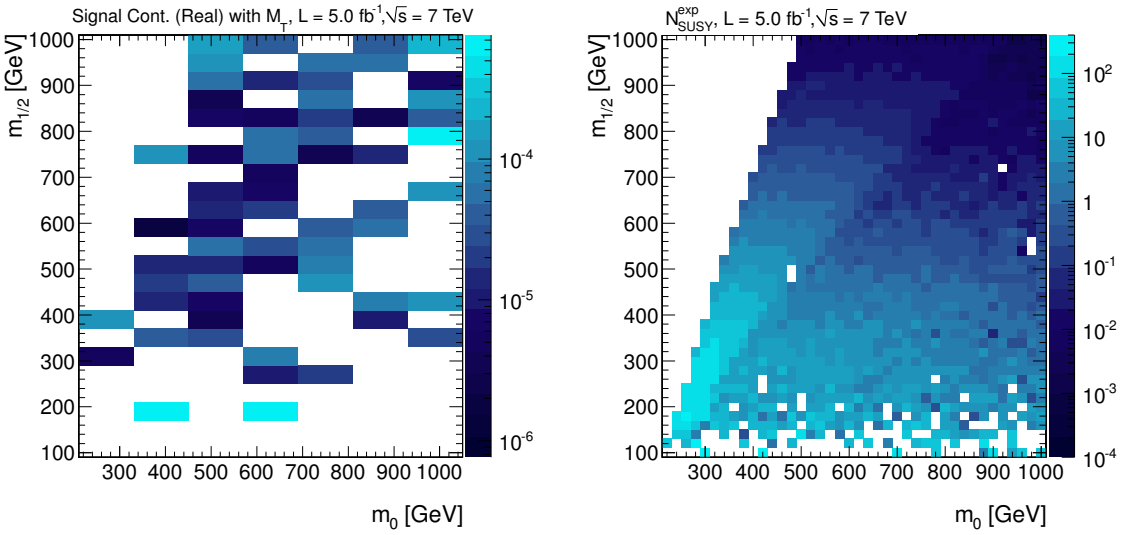


Figure 9.7: Left: Signal Contamination for the real-tau background estimation relative to the number of selected events $N_{SUSY}^{pass}$ in case of the $M_T$ cut applied on the muon sample. Right: $N_{SUSY}^{exp}$ after subtraction of the signal contamination of the fake-tau and the real-tau estimate with the $M_T$ cut applied.

Other uncertainties may vary depending on the signal characteristics:

- **Theoretical Uncertainties on the Cross Section**: The theoretical uncertainties on the calculation of the NLO cross section and the influence of the uncertainty of the particle density functions (PDF) [104] of the proton on the cross section. Combined, they are on the order of 10%.

- **PDF**: The uncertainty on the measurement of the PDF of the proton translates to an uncertainty on the event kinematics of roughly 20%, and is similar over the probed scan range.

- **Lepton Isolation**: The uncertainty on the selection introduced by the uncertainty on the electron and muon isolations. These are taken from [100] and propagate to an uncertainty of approximately 1% for the muon veto and 2% for the electron veto in the co-annihilation region.

- **Jet Energy Corrections**: The uncertainty on the simulated jet energies are 2-5% depending on the transverse momentum and pseudorapidity of the jet [96], and translate to an uncertainty on the selection of 4-10% within the co-annihilation region.

- **Tau Energy Scale**: The tau energy scale has an uncertainty of 3% [101]. This translated to an uncertainty of 1-3%, again for the favoured co-annihilation region.

The resulting combined experimental and combined theoretical uncertainties are shown in figure 9.8. The combined experimental is around 22% for most of the parameter space. The theoretical uncertainties are calculated for $\tan\beta = 10$. This is not a problem, as these uncertainties are approximately the same for $\tan\beta = 40$, and the difference is smaller than the experimental uncertainties.
Figures showing the individual uncertainties listed above for each signal point can be found in appendix E.

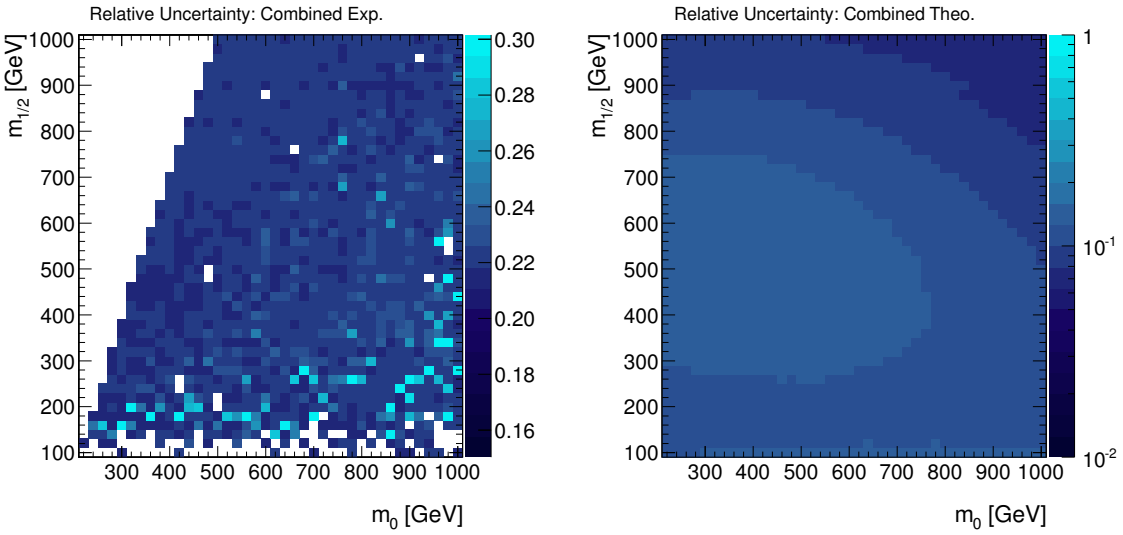


Figure 9.8: Combined experimental (left) and combined theoretical (right) uncertainties for the cMSSM at $\tan\beta = 40$ for the Full selection.

### 9.2.3 cMSSM Exclusion Limits

The limits have been calculated with the $CL_S$ method [105][106][107] implemented in RooStats [108] for a confidence level of 95%. The $CL_S$ method is used to test one hypothesis against another, typically the hypothesis of Standard Model physics together with the presence of a signal "$s+b$" against the hypothesis of Standard Model background only "$b$". In addition, a "confidence level" is defined, giving a measure of the trust one has in the exclusion of a given signal model.
The resulting exclusion limit is shown in figure 9.9. The observed limit is displayed as red, the expected limit is shown as blue straight line. The blue band gives the combined experimental uncertainties on the expected limit. The dotted lines give the theoretical uncertainties on the observed (red) and expected limit (blue), respectively.
As expected, the limit is strongest in the co-annihilation region. In the region still allowed by cosmological constraints, a $m_{1/2}$ mass lower than 520 GeV is excluded. This corresponds to $m_{\tilde{\tau}_1} \approx 280$ GeV and $m_{\tilde{q}} \approx 1100$ GeV for the first two generation of squarks. The limit

drops at the edge where the stau mass becomes larger than the $\chi_0^2/\chi_1^+$ masses, and is no longer part of the predominant decay chain. With increasing $m_0$ and decreasing $m_{1/2}$, the limit enters the region of small simulated statistics, leading to a larger uncertainty. Due to the same reason, at very low $m_{1/2}$, the limit becomes unreliable, which is why it is not shown in this region.
The filled green area is excluded due to the direct search for chargino production at LEP2. The yellow area indicates the limit on direct slepton searches also at LEP2. The gray region denoted with "$\tilde{\tau}$ = LSP" is theoretically excluded because the charged stau would be the sparticle with the lightest mass. Also indicated in light gray are the isolines of equal squark ($\tilde{q}$) and equal gluino ($\tilde{g}$) masses. The region labeled with $0.101 < \Omega_{\mathrm{DM}} < 0.123$ (pink dots) denote the regions where the measured relic density is within a 3 $\sigma$ tolerance. It is the still allowed region, i.e. the co-annihilation region, as discussed in section 2.2.1. All these constraints were taken from [109].
The DØ experiment [110] at the Tevatron [111] has published a search for Supersymmetry with jets, missing transverse energy, and taus [112] with approximately 1 fb$^{-1}$ of data at $\sqrt{s}$ = 1.96 TeV. In the mSugra framework[2] with $\tan\beta = 15$, $A_0 = -2m_0$ and $\mu < 0$, they excluded those parts of the stau-LSP co-annihilation region with $m_{1/2} \lesssim 140$ GeV. In combination with another search done by DØ, which used the fully hadronic channel [113], the excluded mass increased to $m_{1/2} \lesssim 175$ GeV. Note that this tau search also allowed signatures with more than one tau and was not restricted to the single-tau channel.
ATLAS had published a search for Supersymmetry in the single-tau [114] and in the di-tau [115] channel with 2 fb$^{-1}$. They concentrate on gauge-mediated breaking scenarios (see section 2.2.1), and do not provide limits in the cMSSM.
To compare the single-tau limit obtained in this analysis with limits set by other CMS studies, figure 9.10 shows two very recent results, done with roughly the full dataset of 2011[3]. Note that both figures have different ranges in both the $x$- as well as the $y$-axis. Note also that these limits are shown for $\tan\beta = 10$ and $A_0 = 0$, and that such a comparison is only valid if the limits do not strongly depend on $\tan\beta$ and $A_0$, which is not true for the single-tau analysis.
The left figure shows the observed limits for the "Razor" analysis [117]. This analysis combines all objects in the event to two "megajets", which are used to approximate the center-of-mass frame (named the "Razor" frame), and which behave differently for signal and background. The events are grouped in either the leptonic channel, with events with at least one light lepton ($e$, $\mu$), or into the hadronic channel. Also shown is the combination of these two channels, as well as the expected combined limit. Two additional features can be seen in this figure. The first is a region which is excluded because no electroweak symmetry breaking is possible (light gray). The second is a region where the renormalization group equations, which are needed to get a meaningful supersymmetric mass spectrum, do not converge (light blue). This region is not excluded, but unreliable in terms of superpartner

[2]The minimal Supergravity model (mSugra) is very similar to the cMSSM and is treated as equal in this comparison for simplicity.

[3]The luminosity cited in these analyses were taken from the old luminosity measurement [116], where 4.7 fb$^{-1}$ corresponds to the new 5 fb$^{-1}$.

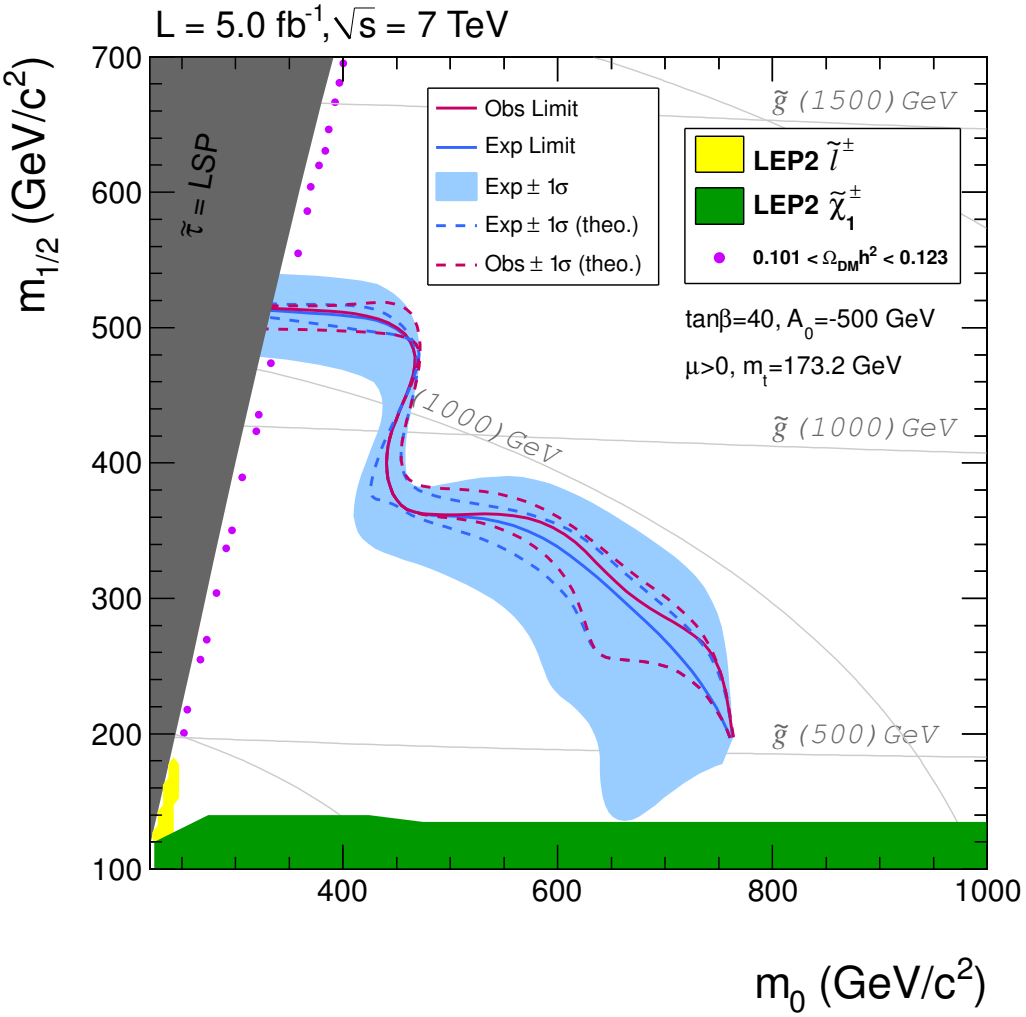


Figure 9.9: cMSSM Exclusion limit at 95% confidence level, done with the $CL_S$ method. The selection used was the Full selection. The red straight line gives the observed limit, whereas the blue straight line indicates the expected limit. The experimental uncertainty on the expected limit are shown as a filled blue band. The dotted lines give the theoretical uncertainty on the cross section for the expected (blue) and the observed (red) limit. Other features of this figure are described in the text.

masses. Both features are also taken from [109]. The Razor analysis provides the most stringent CMS limit of the cMSSM to date. This is due to the fact that, in general, the hadronic branching fractions for supersymmetric events are larger than for events with a leptonic component. Events with hadronic taus only are also part of these hadronic events. It excludes masses of $m_{1/2}$ smaller than $\approx$ 640 GeV at low $m_0$, and masses smaller than $\approx$ 300 GeV at high $m_0$.

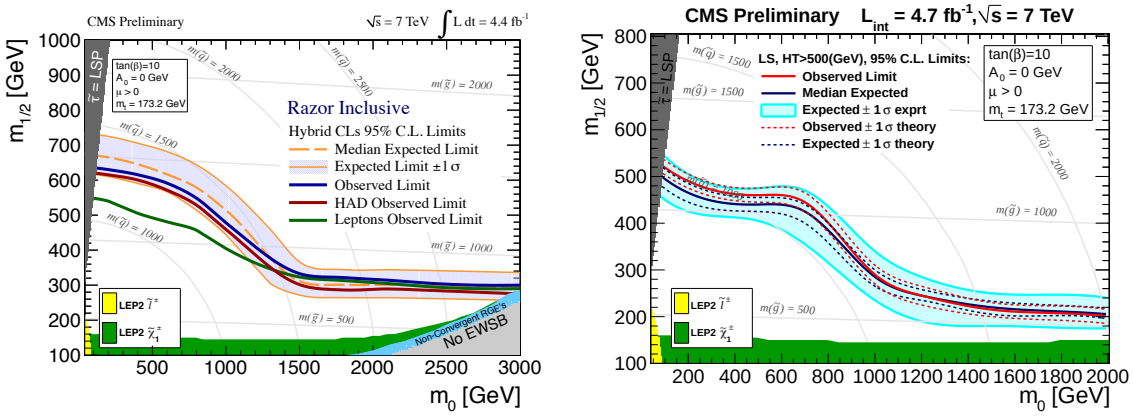


Figure 9.10: Left: Expected and observed limits set by the Razor analysis [117], for the hadronic and leptonic channel. Right: Expected and observed limits set by the Single Lepton analysis [118]. Both studies are done in CMS.

The figure on the right displays the expected and observed limit in the single lepton ($e$, $\mu$) channel [118]. This analysis is using two different search strategies, the Lepton Spectrum Method ("LS"), and the Lepton Projection Method ("LP"). Both methods use the fact that, for single leptons produced in a $W$-decay, the $P_T$ of the lepton is correlated with the missing transverse energy produced by the neutrino. The limits shown are for the LS-method with $H_T > 500$ GeV. Note that this analysis provides limits for several $H_T$ bins, and a combination was not available yet. The Single Lepton searches exclude masses of $m_{1/2}$ up to roughly 520 GeV for small $m_0$, and at large $m_0$, masses lower than approximately 200 GeV.

In comparison to the single-tau search, two aspects of these limits attract attention. The first is the reach of the Razor and Single Lepton up to large $m_0$. The main reason is the high $\not{H}_T$ requirement of the single-tau analysis, while the other limits also include search region with lower $\not{H}_T$. At higher $m_0$, more particles are produced in the decay chain, and the $P_T$ of the LSPs, and thus, the $\not{H}_T$, tends to be small. Another, minor, reason is the increased presence of (light) leptons in the event due to enhanced slepton production.

The second aspect is the fact that the single-tau analysis at large $m_{1/2}$ and smaller $m_0$ is competitive or even slightly stronger than the leptonic search branch of the Razor analysis, as well as the Single Lepton search. This is remarkable, as the light leptons have a much higher identification efficiency than the tau, and also have a higher background suppression ability in for fakes. This shows that the single-tau analysis is not simply an additional search channel to be combined with other limits to gain a small increase of sensitivity, but provides strong limits of its own.

The limits of the hadronic searches are based on the branching fraction of fully hadronic events, and, in addition, the branching fraction of hadronic tau events. In case a supersymmetric benchmark point is realized where in each event at least one tau is present, these hadronic searches are still sensitive to this model. In addition, they do not suffer

from a low tau identification efficiency, such that the signal efficiency would be higher than for a dedicated tau search. The sensitivity depends also on the background suppression ability of the cut variables. Because of this, a general comparison of hadronic and tau searches is difficult. In case of the co-annihilation region, which is close to the ideal case of at least one tau in each event, the hadronic search shows a higher sensitivity than the tau search. However, as soon Supersymmetry (or any other new physics) is found in the hadronic channel, the number of taus identified is of major interest for further analysis of new phenomena.

# Chapter 10

# Conclusion

This thesis was divided in two parts. The first part was performed in the field of computing. The second part was done in analyzing 7 TeV CMS data for the search for physics beyond the Standard Model.
The LHC computing structure is of highly distributed nature. While all data is taken centrally at the detectors, the sheer amount of data does not allow it to be analyzed centrally. Instead, the data is allocated to different computing centers distributed over the world, which have the task of either long-time storing of data (Tier 1 centers), or of appropriation of computing power for the physics analyst (Tier 2 centers). A smooth data flow is highly important for CMS, as broken components can significantly slow down or even prevent the process of producing physics results. Thus, monitoring the system is crucial. Web-based tools are used individually for the different components. This bears the problem of being elaborate and also difficult to interpret for the single computing site. The HappyFace Project provides a framework for collecting and displaying monitoring information already present, conditioned to the site in question. The technical aspect of this thesis was the development of HappyFace modules tailored to the specific needs of a CMS Tier 2 center, namely the center located at DESY. It lead to a less time-consuming monitoring without reduction of site availability.
The analysis part of this thesis was performed using a luminosity of 5 $\text{fb}^{-1}$ of CMS data taken in 2011, and consists of the search for physics beyond the Standard Model in the channel with a single tau, jets, and $\not{H}_{\text{T}}$. It is motivated by the combination of cosmological observations with a certain supersymmetric model, the cMSSM, but is not restricted to it. Combining the cMSSM with the observation of the relic density leads to few regions still allowed by cosmology. One of these regions is the tau producing region. In the mass scheme of the super partners of the Standard Model, the stau becomes the second lightest sparticle, and thus on average, several taus are present in the decay chain. As the hadronic branching fraction of a tau is 65%, and the identification efficiency of a hadronic tau is of $\mathcal{O}(40\%)$, these events often contribute to the single tau channel. This work at hand is the first search for supersymmetry with CMS data in the single tau channel.
Two types of Standard Model background have been identified. Events containing a real tau are the dominating background. The main production channel in this case is the pro-

duction of $W$-bosons associated with jets, but also $t\bar{t}$ events are contributing. The second type of background are events where an ordinary quark or gluon jet is mis-identified as a tau jet. Due to their large cross section, QCD processes are the largest source of fake taus. Both background types have been estimated in a data-driven approach. The real-tau background has been modeled with the tau template method, where muon events are used to mimic tau events, utilizing lepton universality. The main uncertainty here (10%) is coming from the statistical uncertainty of the muon sample. The fake-tau background has been estimated by applying jet fake rates obtained in an independent data sample to all jets in a jet-only control sample, which resembles the topology of the selected fake-tau events. The main uncertainty is the method uncertainty of 21%, but as the fake-tau background is only a small contribution, the uncertainty on the final result is much smaller.
The final selection yields 28 events. The combined Standard Model background was estimated to be $28.5 \pm 2.6(\text{stat}) \pm 2.4(\text{syst})$, and is thus compatible with the observation. As a result, exclusion limits have been set in the cMSSM. They are strongest in the region of enhanced tau production, as expected.
Compared to other leptonic searches in CMS, within the cosmological favored region, the single tau search give competitive or even stronger limits. The hadronic searches give stronger limits than the tau search, but in case of a discovery, this analysis will provide invaluable information about the object content of new physics.
In future analyses, the method of tau embedding could be used instead of the template method used in this work. In it, muons measured in data are replaced with a generated tau with the same kinematics. As the decay of the tau can be generated quite accurately, the real data events are overlaid with simulated tau on hit level. By this, the influence of the differences in event topology on the tau identification efficiency are included in a natural way.
Another possibility to improve this analysis would be the inclusion of other signal regions, to get less specialized on the co-annihilation region. Also, while the focus in this thesis lies on the cMSSM, other models like the gauge-mediated breaking model are known to include tau producing scenarios.
Also, an analysis that includes also the quality of the shape agreement of interesting distributions like $\not{H}_T$ could improve this already successful counting analysis further.
In 2012, The LHC will run at a center-of-mass energy of 8 TeV. The cross section of Supersymmetric events would grow by more than one and a half, which is more than for the background, and thus increase the sensitivity of all searches. In addition, 15 $\text{fb}^{-1}$ are expected during this one-year run, i.e. three times more than used in this thesis. The most important result expected however, will be the discovery or exclusion of a light mass higgs boson. An exclusion of a light higgs boson would impose strong constraints on Supersymmetry models, while a discovery would be compatible with most of the scenarios. All in all, further regions of the supersymmetric phase space will be probed, such that exciting results for 2012 are to be expected.

# Appendix A

# Muon Reconstruction and Isolation Efficiencies

This appendix shows the muon reconstruction and isolation efficiencies obtained in $Z$-boson events. For the reconstruction, the efficiency depends on the muon $\mathrm{P_T}$ and $\eta$. In case of isolation, it is parametrized in $\Delta R^{nextjet} = \sqrt{\Delta\eta^2 + \Delta\phi^2}$ to the next jet and the relative transverse momentum $\mathrm{P_T^{rel}} = \frac{\mathrm{P_T^{\mu}}}{\mathrm{P_T^{nextjet}}}$ to this jet. From [100].

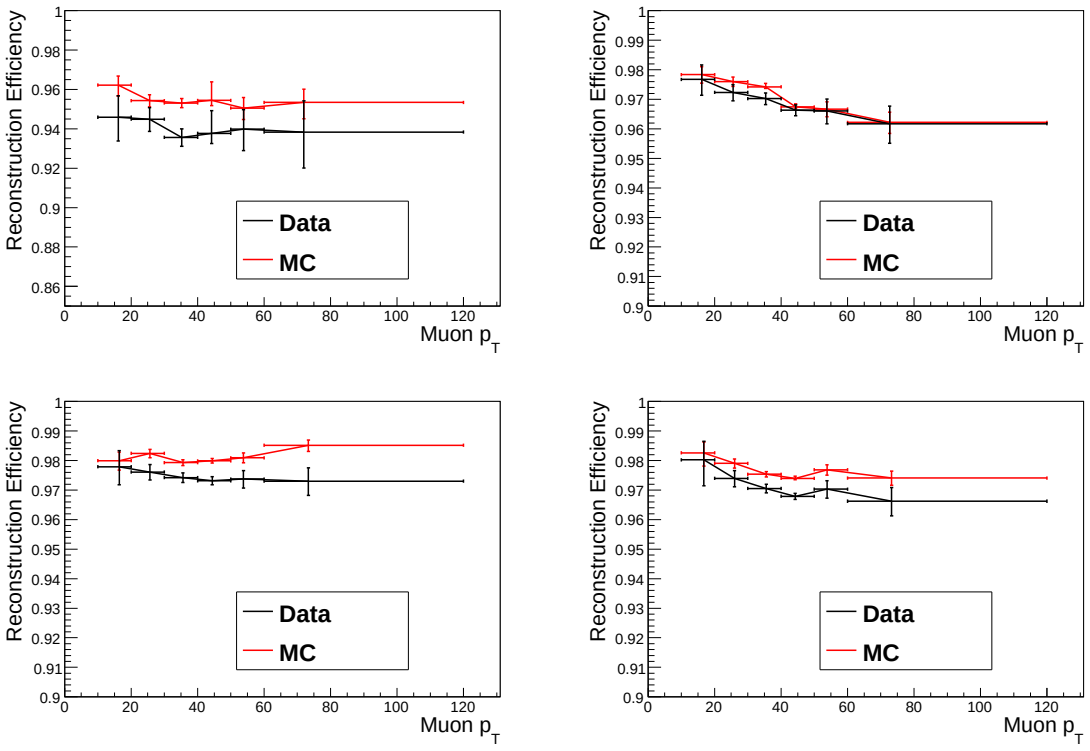


Figure A.1: Muon reconstruction efficiency depending on muon $P_T$ in $-2.4 < \eta < -2.1$ (upper left), $-2.1 < \eta < -1.4$ (upper right), $-1.4 < \eta < -0.7$ (lower left), and $-0.7 < \eta < 0$ (lower right). From [100].

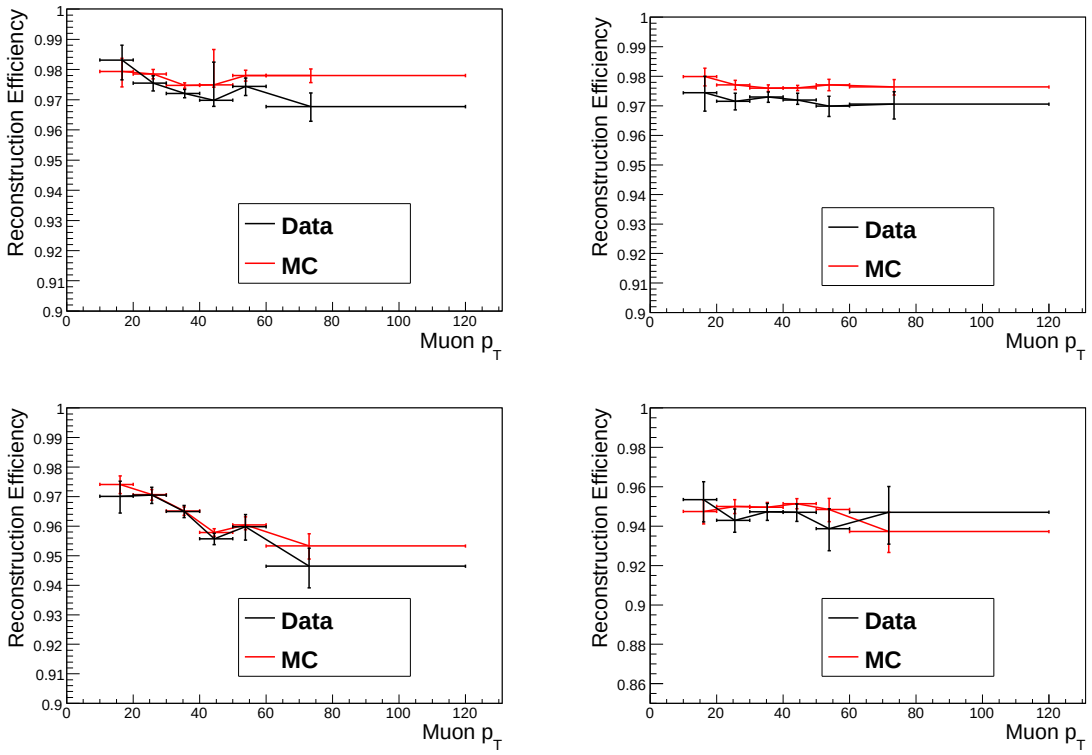


Figure A.2: Muon reconstruction efficiency depending on muon $P_T$ in $0 < \eta < 0.7$ (upper left), $0.7 < \eta < 1.4$ (upper right), $1.4 < \eta < 2.1$ (lower left), and $2.1 < \eta < 2.4$ (lower right). From [100].

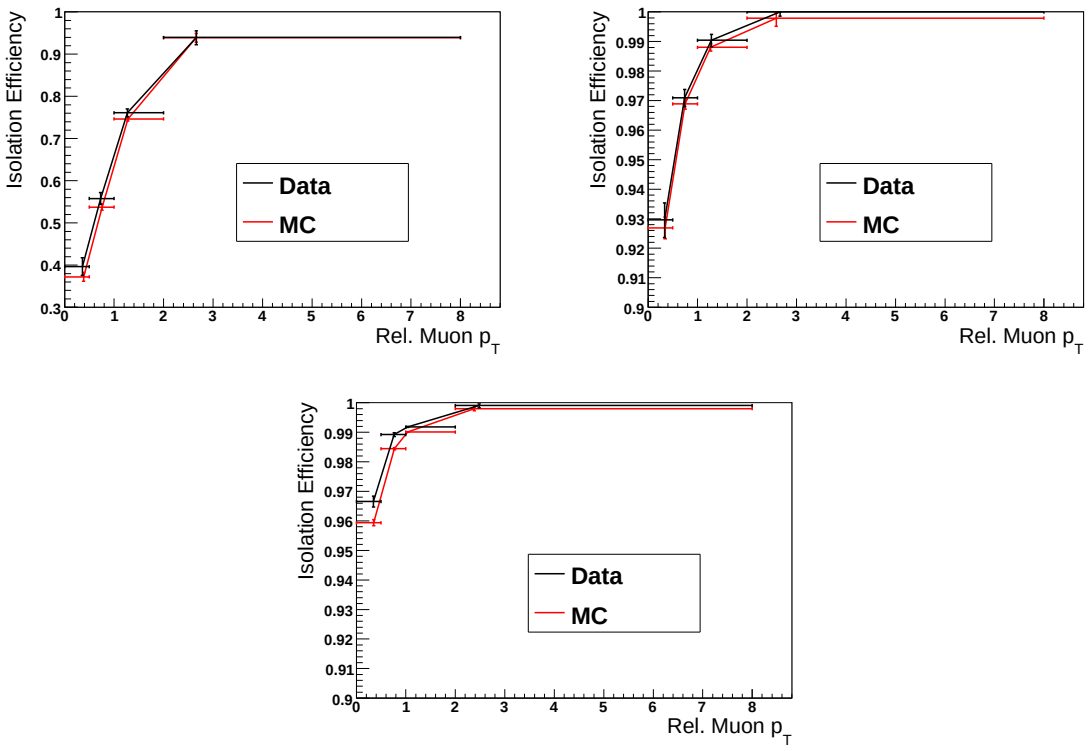


Figure A.3: Muon isolation efficiency depending on muon $P_T^{rel}$ with $\Delta R^{nextjet} < 0.5$ (upper left), $0.5 < \Delta R^{nextjet} < 1$ (upper right), and $1 < \Delta R^{nextjet} < 5$ (lower left). From [100].

# Appendix B

# Real-Tau Estimate with $\mathrm{M_T}$ cut

In this chapter, the closure distributions in simulated $W$-boson events for the real-tau estimate with $\mathrm{M_T} < 100$ GeV applied on the muon sample are shown in figure B.1, B.2, B.3, and B.4. The prediction was scaled upwards by 3%.

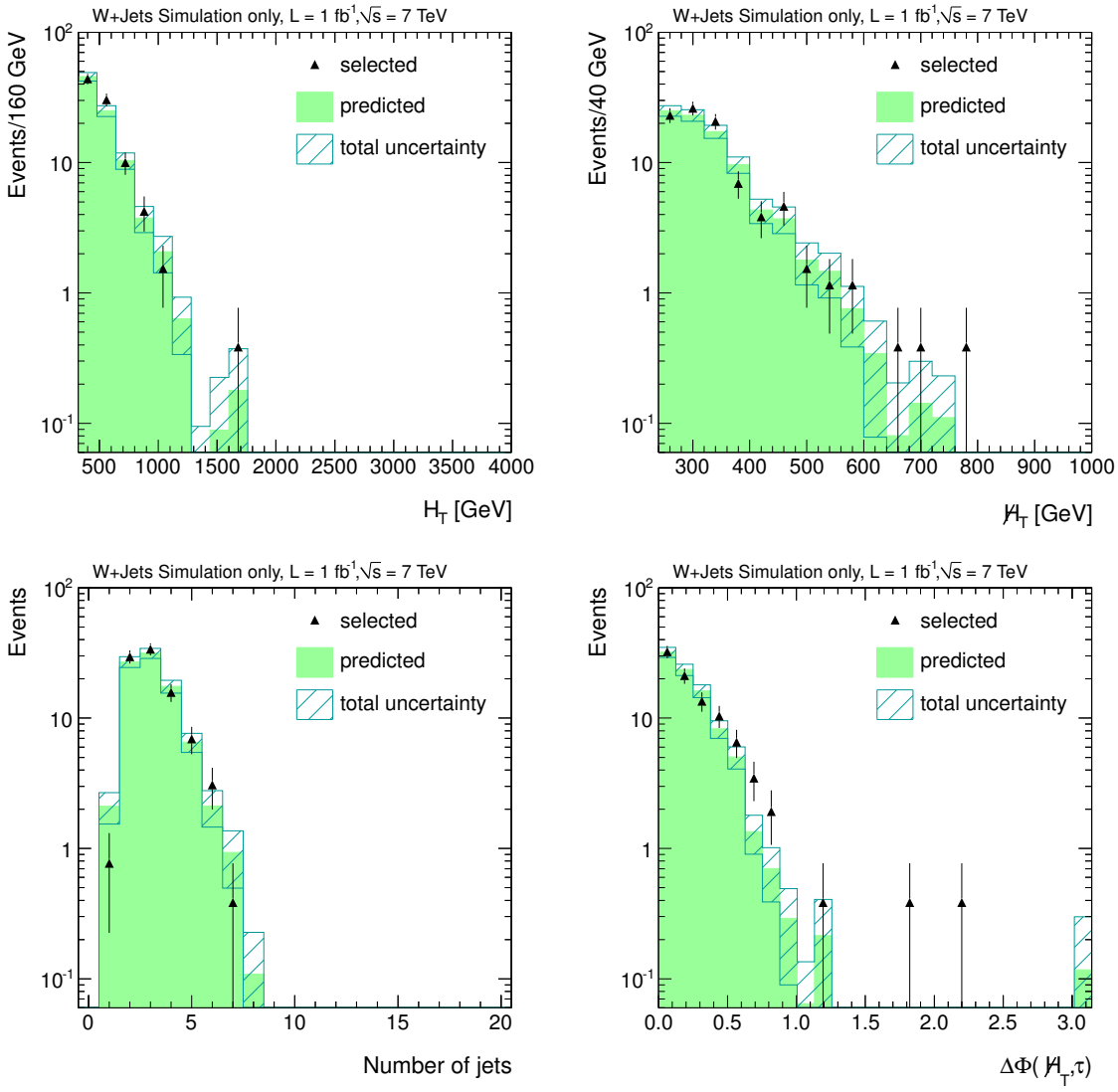


Figure B.1: $H_T$ and $\not\!\!H_T$ (upper row), and number of Jets with $P_T > 30$ GeV and $\Delta\Phi(\not\!\!H_T, \tau)$ (lower row) distributions for the real-tau estimate in $W$ plus jets simulated events. The black triangles are the simulated events passing the Base-Line selection and having the reconstructed tau matched to a generated tau on simulation level. The filled green area gives the predicted events. The hatched areas are the uncertainties composed of the statistical uncertainties of the sample, as well as the systematic uncertainties. The events are normalized to 1 fb$^{-1}$ of luminosity.

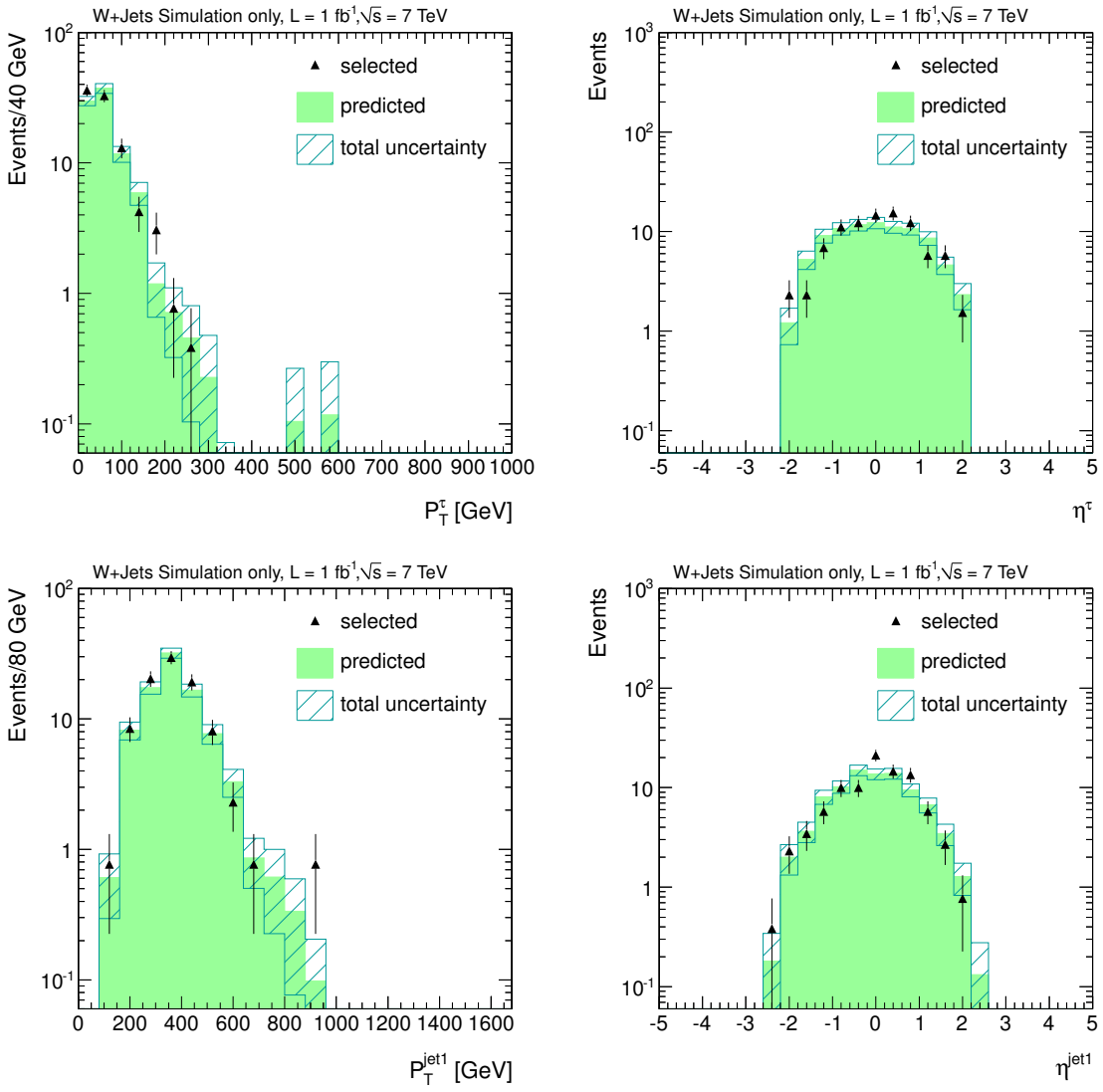


Figure B.2: $P_T$ and $\eta$ of the tau (upper row), and the leading jet for the case of $P_T^{jet} > 30$ GeV (lower row) for the real-tau estimate in $W$ plus jets simulated events. See figure 8.8 for details.

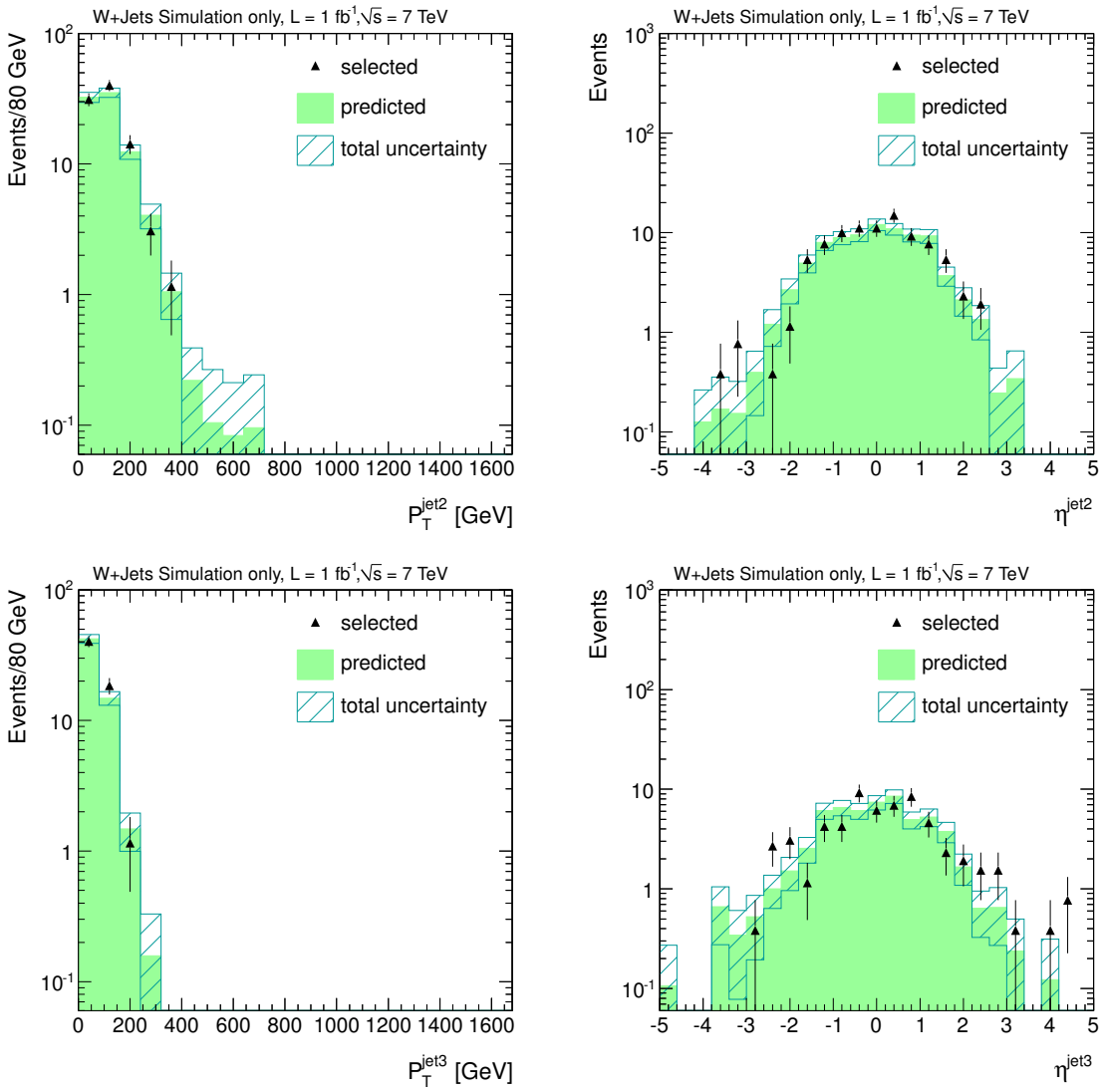


Figure B.3: $P_T$ and $\eta$ of the second (upper row), and the third leading jet (lower row) in case of $P_T^{jet} > 30$ GeV for the real-tau estimate in $W$ plus jets simulated events. See figure 8.8 for details.

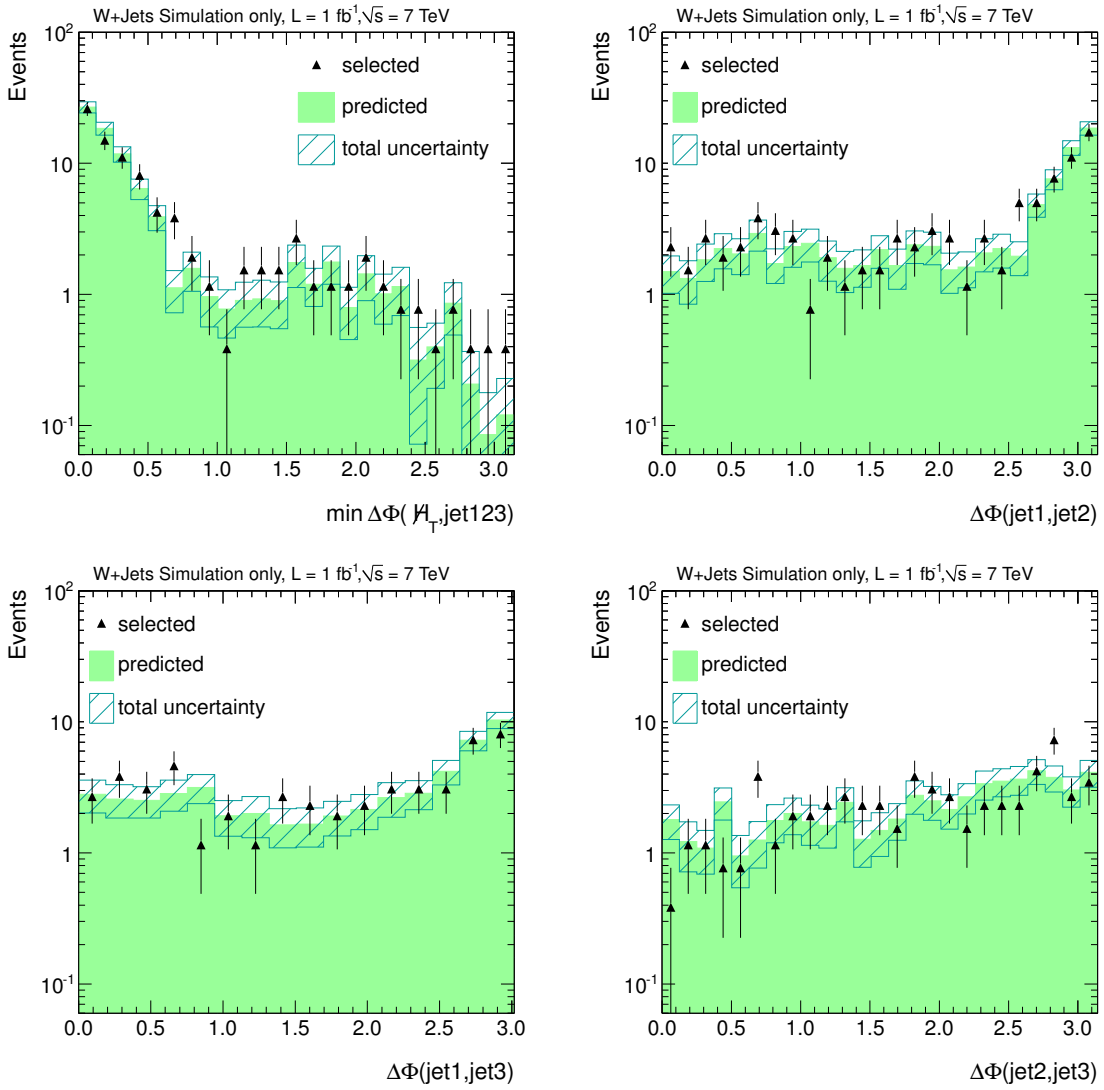


Figure B.4: Minimal angle between $\not{H}_T$ and the first leading jets $\min\Delta\Phi(\not{H}_T, jet(1,2,3))$ and $\Delta\Phi(jet1, jet2)$ (upper row), and $\Delta\Phi(jet1, jet3)$ and $\Delta\Phi(jet2, jet3)$ (lower row) for the real-tau estimate in $W$ plus jets simulated events. The used jets have at least 30 GeV of $P_T$. See figure 8.8 for details.

# Appendix C

# Data Results without $M_T$ cut

This chapter contains the results for this study with no $M_T$ cut applied on the muon control sample of the real-tau estimate. Table C.1 summarizes the event yield for Base-Line and Full selection for 5 fb$^{-1}$ of CMS data. For the fake-tau estimate, 7651 (Base-Line) and 386 (Full) events have been used. For the real-tau estimate, the muon sample consisted of 1897 (Base-Line) and 128 (Full) events. Figure 9.1, 9.2, 9.3, and 9.4 show control distributions for the Base-Line selection.

| 5 fb$^{-1}$ | Base-Line | Full |
|---|---|---|
| Fake-Tau Est. | $67 \pm 2$ (stat) $\pm 15$ (syst) | $3.4 \pm 0.4$ (stat) $\pm 0.7$ (syst) |
| Real-Tau Est. | $367 \pm 10$ (stat) $\pm 27$ (syst) | $25.9 \pm 2.5$ (stat) $\pm 2.3$ (syst) |
| Sum | $434 \pm 10$ (stat) $\pm 31$ (syst) | $29.3 \pm 2.6$ (stat) $\pm 2.4$ (syst) |
| Data | 444 | 28 |

Table C.1: Event yield and prediction for Base-Line and Full selected events for 5 fb$^{-1}$ of CMS data. No $M_T$ cut has been applied.

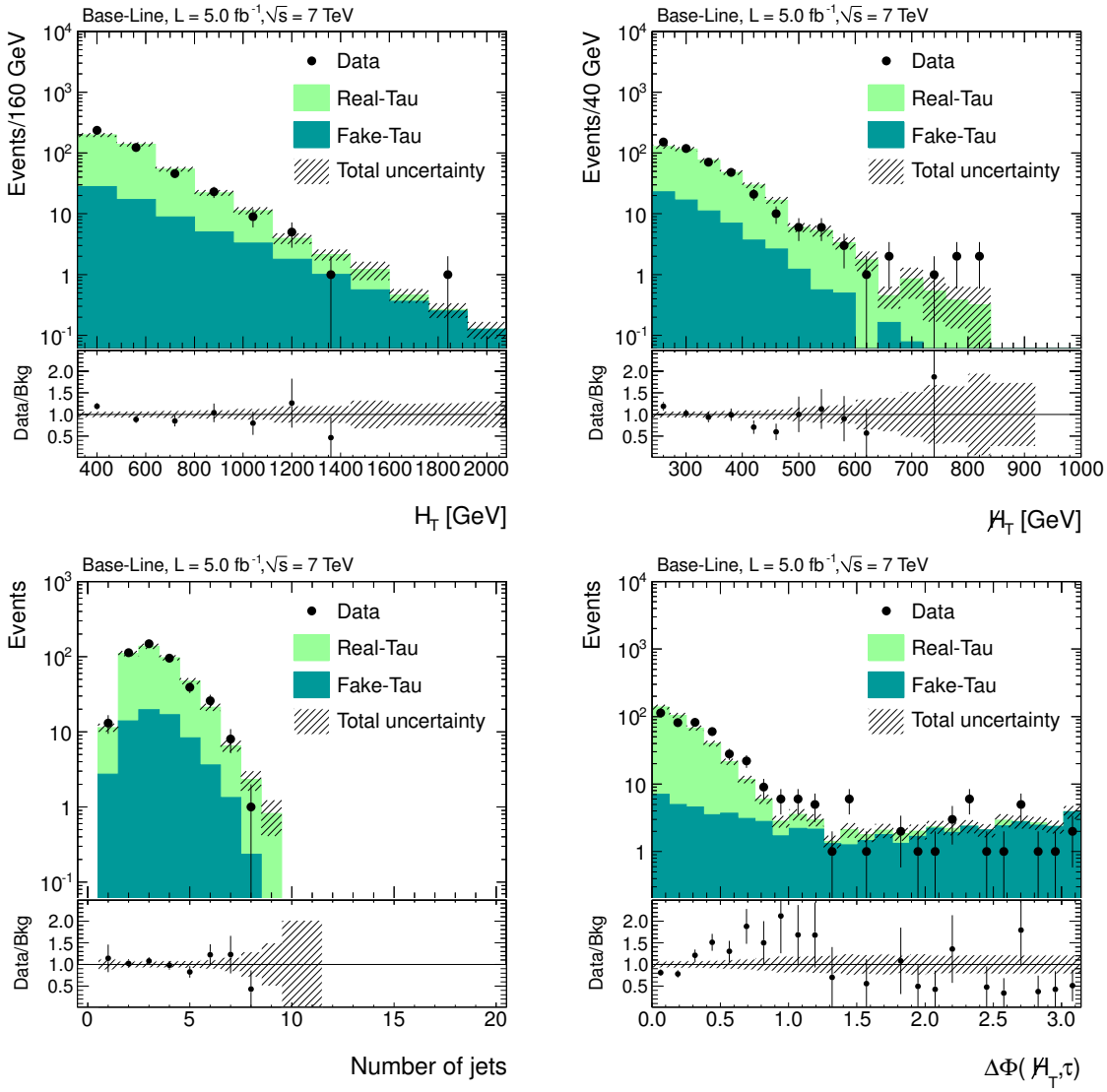


Figure C.1: $H_T$ and $\not{H}_T$ (upper row), and number of Jets with $P_T > 30$ GeV and $\Delta\Phi(\not{H}_T, \tau)$ (lower row) distributions for 5 fb$^{-1}$ of data. The black dots are the data events passing the Base-Line selection. The filled green (light) area gives the predicted background containing a real tau, the filled blue (dark) area describes the predicted background with fake taus. The hatched area indicates the total uncertainty of the background prediction.

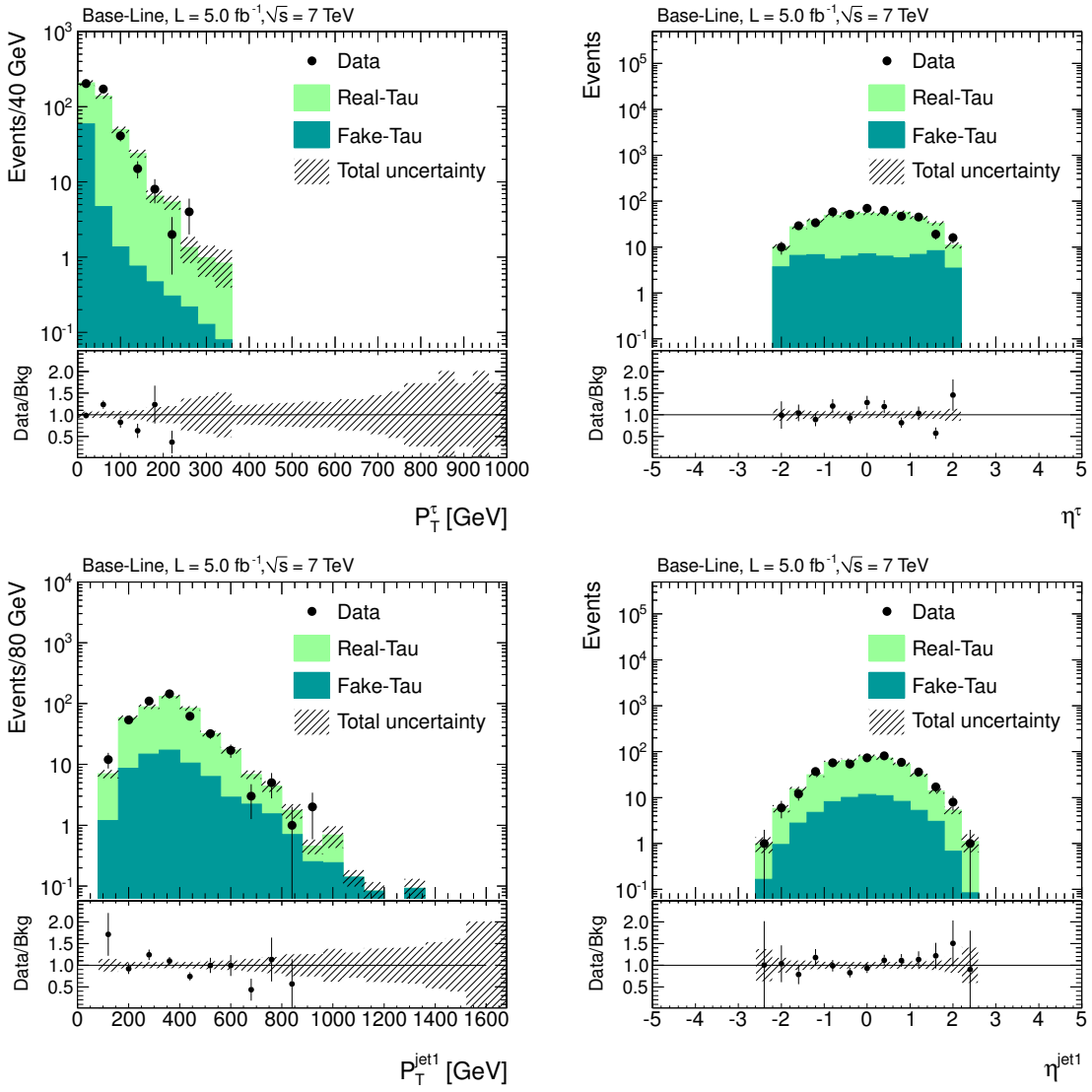


Figure C.2: $P_T$ and $\eta$ of the tau (upper row), and the leading jet for the case of $P_T^{jet} > 30$ GeV (lower row) for 5 fb$^{-1}$ of data. For details, see figure 9.1.

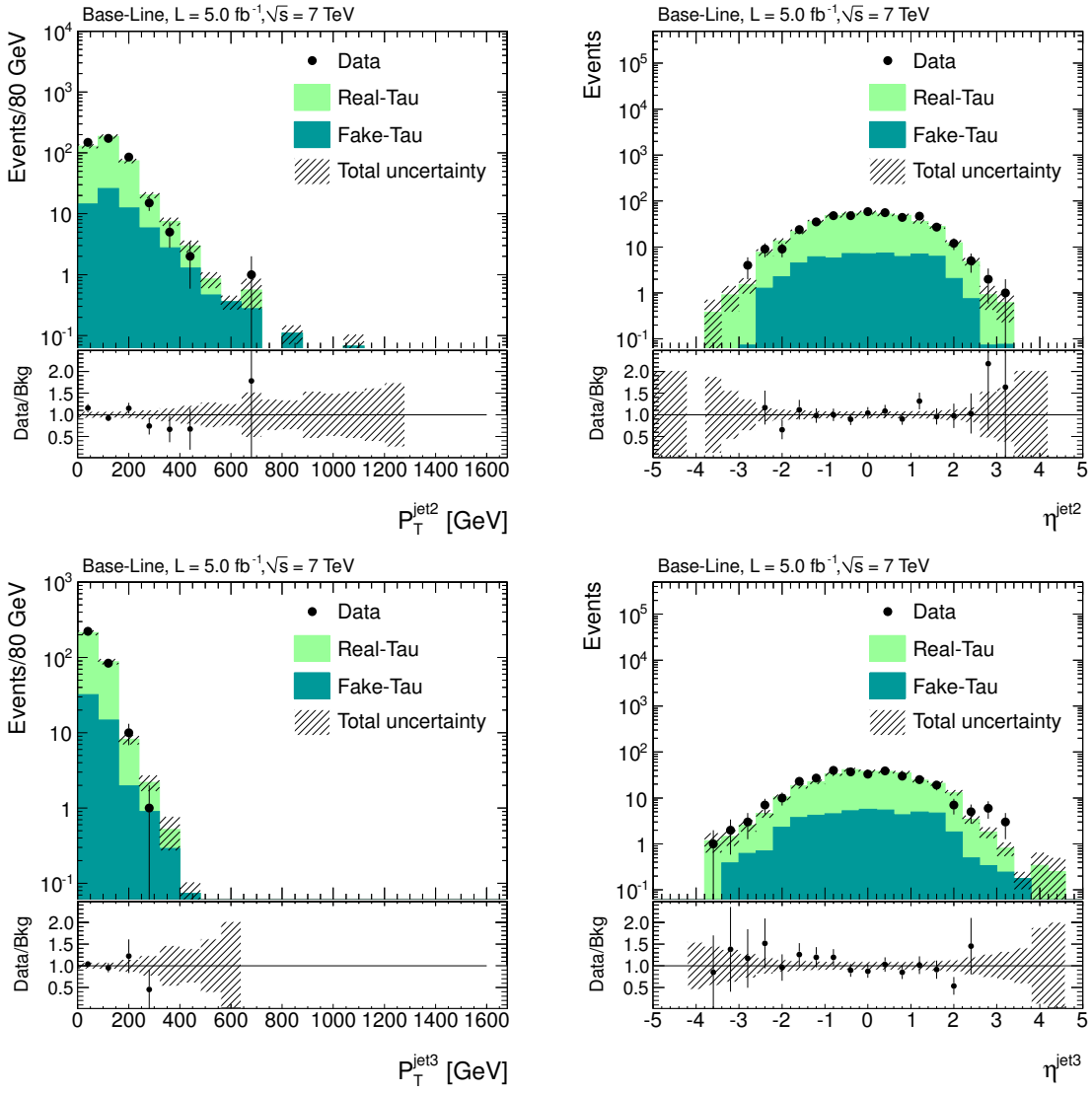


Figure C.3: $P_T$ and $\eta$ of the second (upper row), and the third leading jet (lower row) in case of $P_T^{jet} > 30$ GeV for 5 fb$^{-1}$ of data. For details, see figure 9.1.

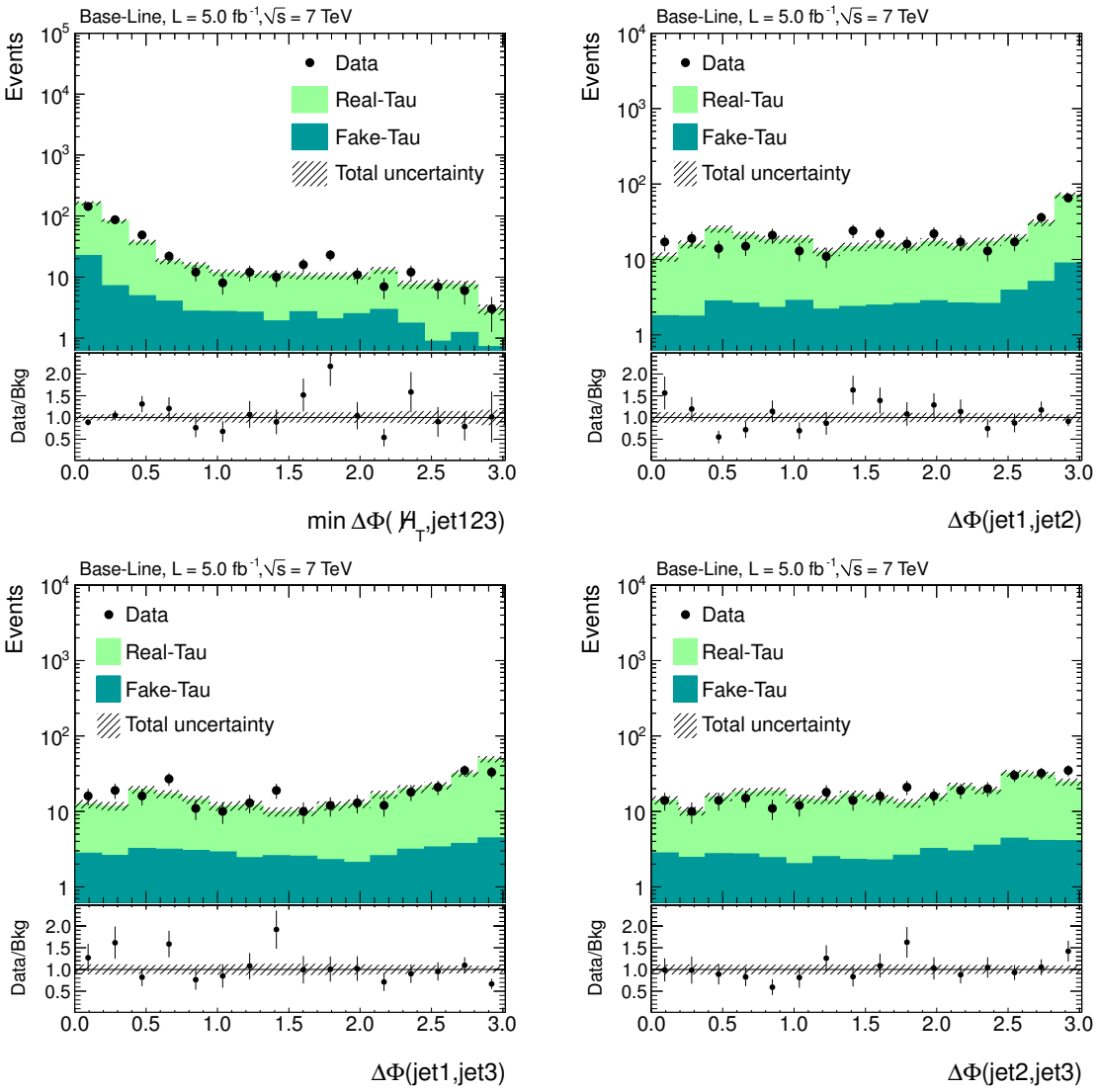


Figure C.4: Minimal angle between $\not{H}_T$ and the first leading jets $\min\Delta\Phi(\not{H}_T, jet(1,2,3))$ and $\Delta\Phi(jet1, jet2)$ (upper row), and $\Delta\Phi(jet1, jet3)$ and $\Delta\Phi(jet2, jet3)$ (lower row) for 5 fb$^{-1}$ of data. For details, see figure 9.1.

# Appendix D

# Event Displays

In this chapter, displays of the data events with the five highest $\not{H}_T$ values are shown.

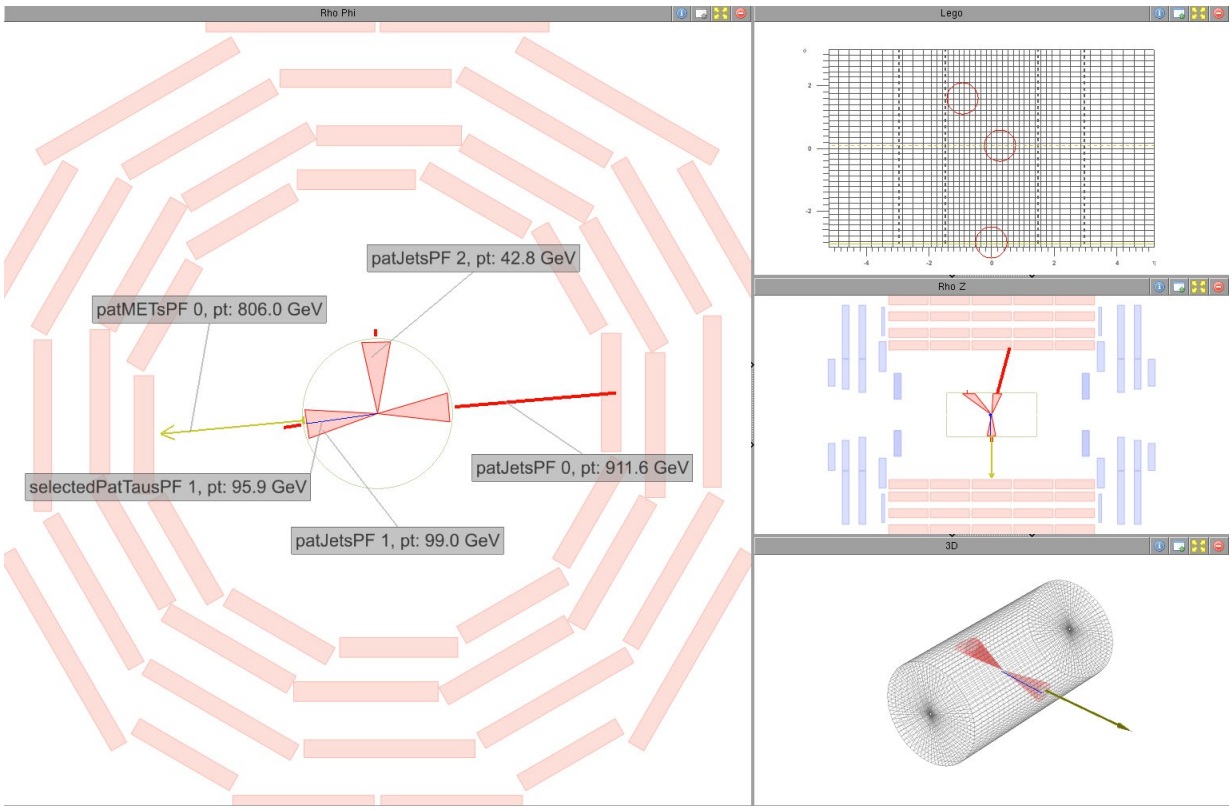


Figure D.1: Event display of event 1049588789, lumi section 1022, and run number 167830. The corresponding $\not{H}_T$ is 815 GeV. Shown are all jets within $\eta < 5$ and $P_T > 30$ GeV (red), taus (blue), and the missing energy vector $\not{E}_T$. It is constructed out of particle flow candidates, and closely related to $\not{H}_T$.

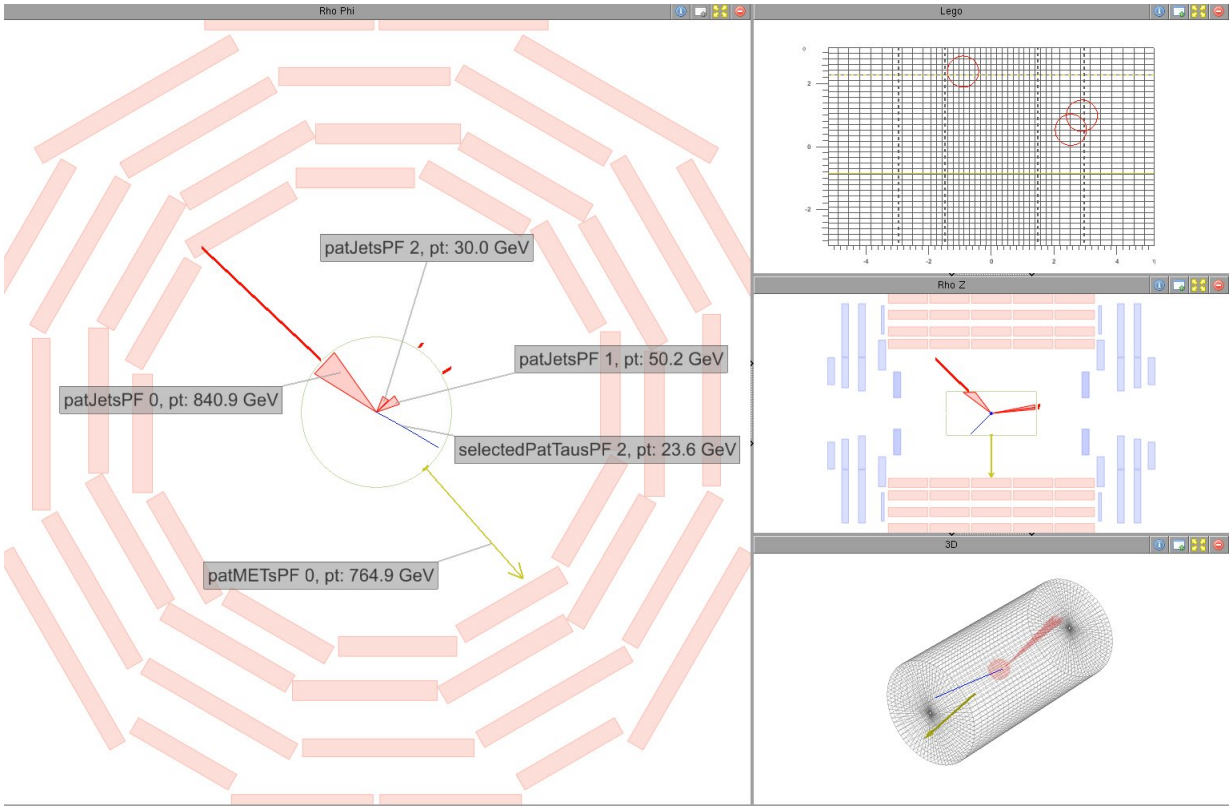


Figure D.2: Event display of event 1058507459, lumi section 649, and run number 178098. The corresponding $\not{H}_T$ is 835 GeV. Shown are all jets within $\eta < 5$ and $P_T > 30$ GeV (red), taus (blue), and the missing energy vector $\not{E}_T$. It is constructed out of particle flow candidates, and closely related to $\not{H}_T$.

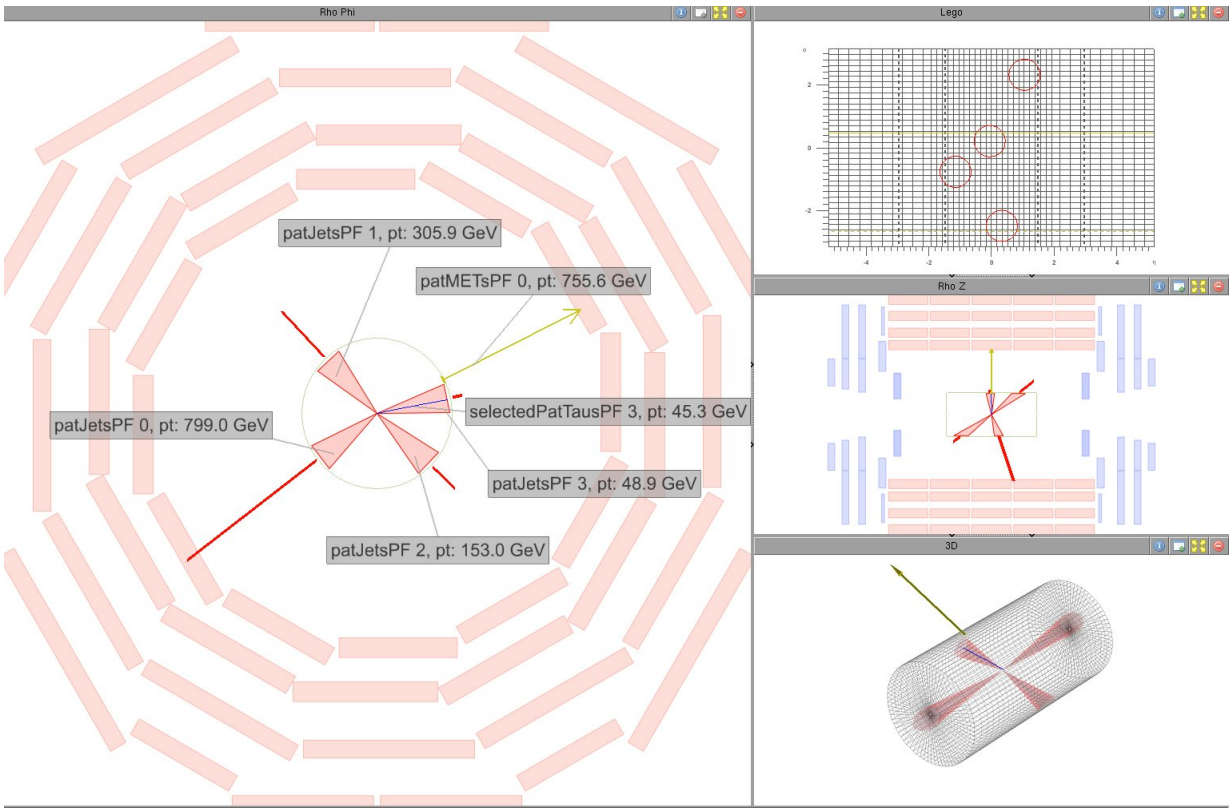


Figure D.3: Event display of event 1343406716, lumi section 1134, and run number 167898. The corresponding $\not{H}_T$ is 770 GeV. Shown are all jets within $\eta < 5$ and $P_T > 30$ GeV (red), taus (blue), and the missing energy vector $\not{E}_T$. It is constructed out of particle flow candidates, and closely related to $\not{H}_T$.

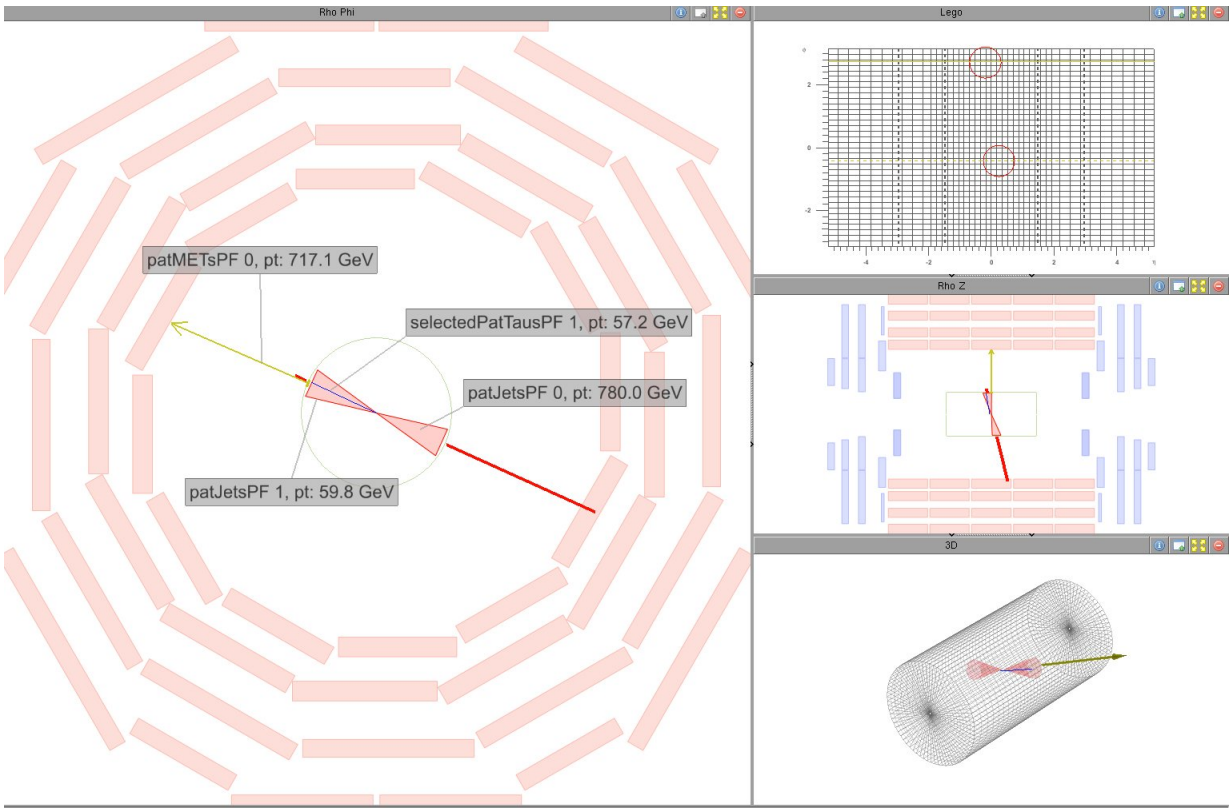


Figure D.4: Event display of event 34221013, lumi section 25, and run number 178854. The corresponding $\not{H}_T$ is 720 GeV. Shown are all jets within $\eta < 5$ and $P_T > 30$ GeV (red), taus (blue), and the missing energy vector $\not{E}_T$. It is constructed out of particle flow candidates, and closely related to $\not{H}_T$.

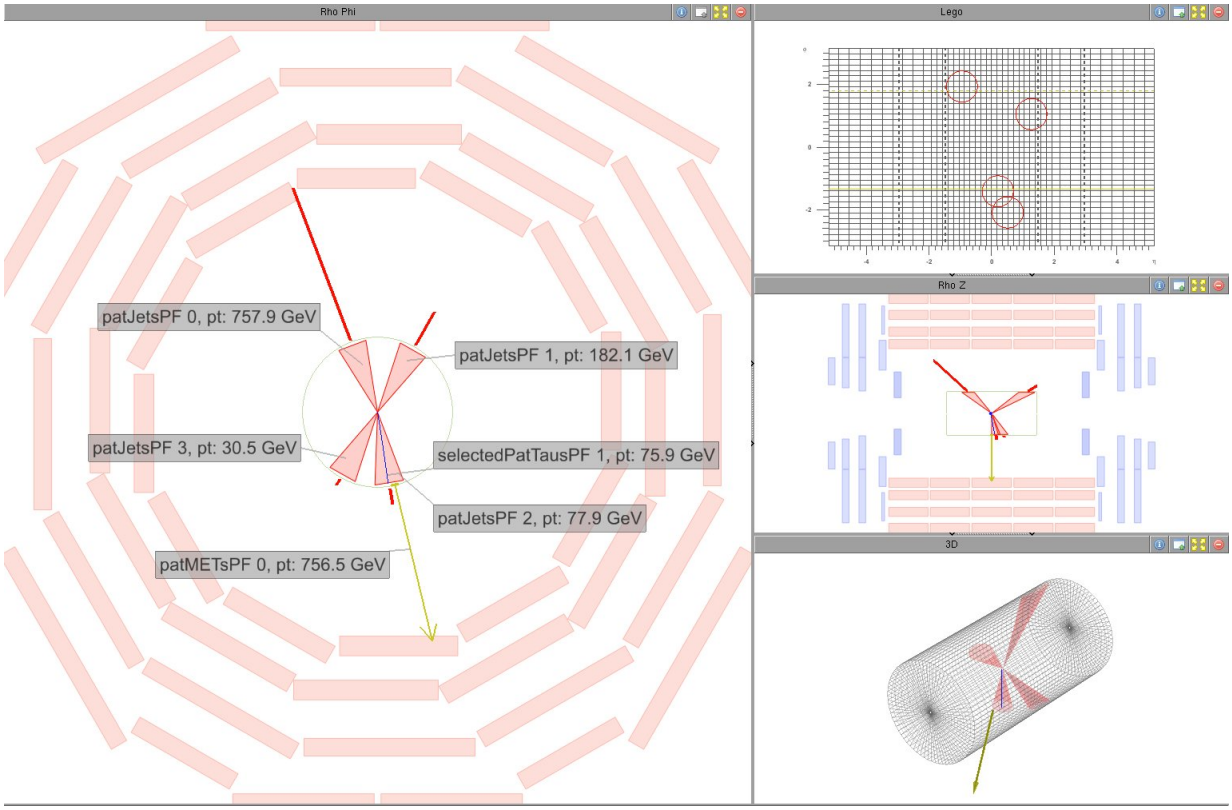


Figure D.5: Event display of event 642989372, lumi section 393, and run number 178866. The corresponding $\not{H}_T$ is 785 GeV. Shown are all jets within $\eta < 5$ and $P_T > 30$ GeV (red), taus (blue), and the missing energy vector $\not{E}_T$. It is constructed out of particle flow candidates, and closely related to $\not{H}_T$.

# Appendix E

# Experimental Signal Uncertainties

In this chapter, the different contributions to the experimental uncertainty on the expected Limit are shown. These are the uncertainty on the event kinematics due to PDF uncertainties, the uncertainty coming from the lepton isolation, the uncertainty from the jet energy corrections and the tau energy scale.

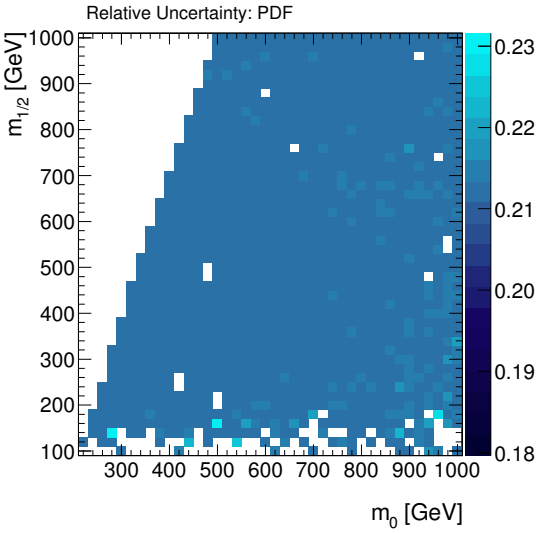


Figure E.1: Relative signal uncertainty coming from the PDF uncertainty on the kinematics for the cMSSM with $\tan\beta = 40$ at the Full selection.

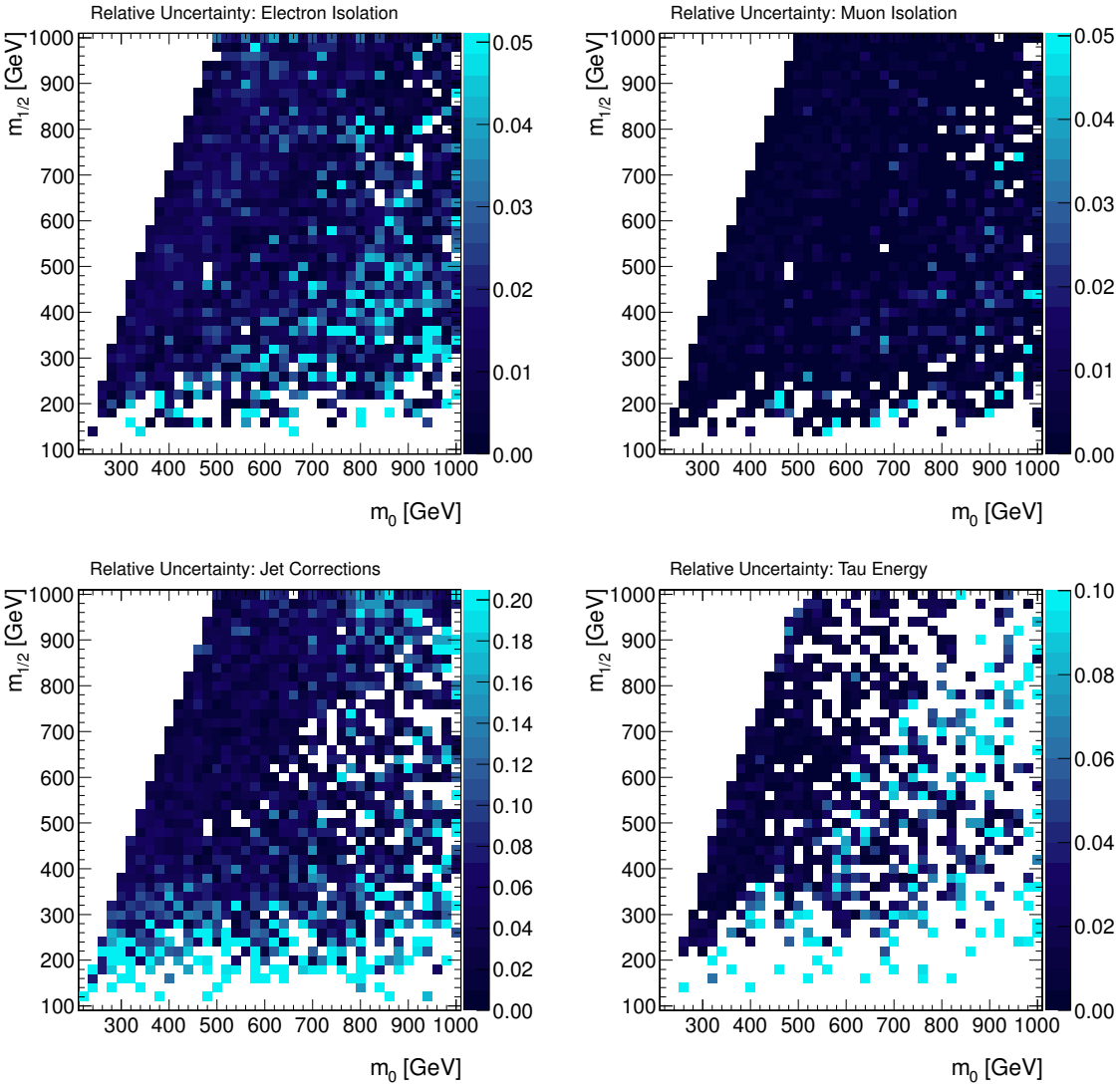


Figure E.2: Relative signal uncertainty coming from the electron (upper left) and muon (upper right) isolation uncertainty, as well as coming from the jet energy correction uncertainty (lower left) and tau energy scale (lower right) for the cMSSM with $\tan\beta = 40$ at the Full selection.

# Bibliography


[1] H. Spiesberger, M. Spira, and P. Zerwas, "The Standard model: Physical basis and scattering experiments", arXiv:hep-ph/0011255. To be published in 'Scattering', P. Sabatier, editor. Academic Press, London, 2000.

[2] D. Gross and F. Wilczek, "Ultraviolet Behavior of Nonabelian Gauge Theories", *Phys.Rev.Lett.* **30** (1973) 1343–1346. doi:10.1103/PhysRevLett.30.1343.

[3] H. Politzer, "Reliable Perturbative Results for Strong Interactions?", *Phys.Rev.Lett.* **30** (1973) 1346–1349. doi:10.1103/PhysRevLett.30.1346.

[4] G. Altarelli, "A QCD Primer", *AIP Conf. Proc.* **631** (Apr, 2002) 70–111.

[5] LEPS Collaboration, "Evidence of the $\Theta^+$ in the $\gamma d \to K^+K^-pn$ reaction", *Phys.Rev.* **C79** (2009) 025210, arXiv:0812.1035. doi:10.1103/PhysRevC.79.025210.

[6] G. P. Salam, "Towards Jetography", *Eur.Phys.J.* **C67** (2010) 637–686, arXiv:0906.1833. doi:10.1140/epjc/s10052-010-1314-6.

[7] F. Mandl and G. Shaw, "Quantenfeldtheorie", *AULA-Verlag Wiesbaden* (1993).

[8] K. Nakamura et al., "Particle Data Group", *Journal of Physics G37, 075021* (2010 and 2011 partial update for the 2012 edition).

[9] Gargamelle Neutrino Collaboration, "Observation of Neutrino Like Interactions Without Muon Or Electron in the Gargamelle Neutrino Experiment", *Phys.Lett.* **B46** (1973) 138–140. doi:10.1016/0370-2693(73)90499-1.

[10] CMS Collaboration, "Combined results of searches for a Higgs boson in the context of the standard model and beyond-standard models", *CMS-PAS-HIG-12-008*.

[11] ATLAS Collaboration, "An update to the combined search for the Standard Model Higgs boson with the ATLAS detector at the LHC using up to 4.9 fb$^{-1}$ of pp collision data at $\sqrt{s} = 7$ TeV", *ATLAS-CONF-2012-019*.

[12] CDF Collaboration, "Combination of CDF's searches for the standard model Higgs boson with up to 10.0 fb$^{-1}$ of data", *CDF Note 10804*.

[13] W. de Boer, C. Sander, V. Zhukov et al., "Egret excess of diffuse galactic gamma rays as tracer of dark matter", *Astron.Astrophys.* **444** (2005) 51, arXiv:astro-ph/0508617. doi:10.1051/0004-6361:20053726.

[14] M. Milgrom, "A Modification of the Newtonian dynamics as a possible alternative to the hidden mass hypothesis", *Astrophys.J.* **270** (1983) 365–370. doi:10.1086/161130.

[15] L. M. J. S. Volders, "Neutral hydrogen in M 33 and M 101", *Bulletin of the Astronomical Institutes of the Netherlands* **14** (September, 1959) 323.

[16] D. Clowe, M. Bradac, A. H. Gonzalez et al., "A direct empirical proof of the existence of dark matter", *Astrophys.J.* **648** (2006) L109–L113, arXiv:astro-ph/0608407. doi:10.1086/508162.

[17] Super-Kamiokande Collaboration, "Evidence for oscillation of atmospheric neutrinos", *Phys.Rev.Lett.* **81** (1998) 1562–1567, arXiv:hep-ex/9807003. doi:10.1103/PhysRevLett.81.1562.

[18] S. R. Coleman and J. Mandula, "ALL POSSIBLE SYMMETRIES OF THE S MATRIX", *Phys.Rev.* **159** (1967) 1251–1256. doi:10.1103/PhysRev.159.1251.

[19] R. Haag, J. T. Lopuszanski, and M. Sohnius, "All Possible Generators of Supersymmetries of the s Matrix", *Nucl.Phys.* **B88** (1975) 257. doi:10.1016/0550-3213(75)90279-5.

[20] J. Wess and B. Zumino, "Supergauge Transformations in Four-Dimensions", *Nucl.Phys.* **B70** (1974) 39–50. doi:10.1016/0550-3213(74)90355-1.

[21] J. Wess and J. Bagger, "Supersymmetry and Supergravity", *Princeton University Press, Princeton, New Jersey* (1992).

[22] M. Spira and P. M. Zerwas, "Electroweak symmetry breaking and Higgs physics", *Lect.Notes Phys.* **512** (1998) 161–225, arXiv:hep-ph/9803257.

[23] D. Chung, L. Everett, G. Kane et al., "The Soft supersymmetry breaking Lagrangian: Theory and applications", *Phys.Rept.* **407** (2005) 1–203, arXiv:hep-ph/0312378. doi:10.1016/j.physrep.2004.08.032.

[24] J. M. Lindert, F. D. Steffen, and M. K. Trenkel, "Direct stau production at hadron colliders in cosmologically motivated scenarios", *JHEP* **1108** (2011) 151, arXiv:1106.4005. doi:10.1007/JHEP08(2011)151.

[25] H. Baer, C.-h. Chen, M. Drees et al., "Supersymmetry reach of Tevatron upgrades: The Large tan Beta case", *Phys.Rev.* **D58** (1998) 075008, arXiv:hep-ph/9802441. doi:10.1103/PhysRevD.58.075008.

[26] http://supernova.lbl.gov/.

[27] WMAP Collaboration, "Seven-Year Wilkinson Microwave Anisotropy Probe (WMAP) Observations: Cosmological Interpretation", *Astrophys.J.Suppl.* **192** (2011) 18, arXiv:1001.4538. 57 pages, 20 figures. Accepted for publication in ApJS. (v2) References added. The SZ section expanded with more analysis. The discrepancy between the KS and X-ray derived profiles has been resolved. (v3) New analysis of the SZ effect on individual clusters added (Section 7.3). The LCDM parameters have been updated using the latest recombination history code (RECFAST version 1.5). doi:10.1088/0067-0049/192/2/18.

[28] A. Lahanas, D. V. Nanopoulos, and V. Spanos, "Updating the constraints to CMSSM from cosmology and accelerator experiments", arXiv:hep-ph/0211286.

[29] G. L. Kane, C. F. Kolda, L. Roszkowski et al., "Study of constrained minimal supersymmetry", *Phys.Rev.* **D49** (1994) 6173–6210, arXiv:hep-ph/9312272. doi:10.1103/PhysRevD.49.6173.

[30] J. R. Ellis, T. Falk, and K. A. Olive, "Neutralino - Stau coannihilation and the cosmological upper limit on the mass of the lightest supersymmetric particle", *Phys.Lett.* **B444** (1998) 367–372, arXiv:hep-ph/9810360. doi:10.1016/S0370-2693(98)01392-6.

[31] K. Hagiwara, A. Martin, D. Nomura et al., "Improved predictions for g-2 of the muon and $\alpha_{\rm QED}(M_Z^2)$", *Phys.Lett.* **B649** (2007) 173–179, arXiv:hep-ph/0611102. doi:10.1016/j.physletb.2007.04.012.

[32] Belle Collaboration Collaboration, "Measurement of Inclusive Radiative B-meson Decays with a Photon Energy Threshold of 1.7 GeV", *Phys.Rev.Lett.* **103** (2009) 241801, arXiv:0907.1384. 9 pages, 3 figures, 2 tables. doi:10.1103/PhysRevLett.103.241801.

[33] "Search for the rare decay $B_s^0 \to \mu^+\mu^-$ at the LHC with the CMS and LHCb experiments", *CMS-PAS-BPH-11-019* (Aug, 2011). Linked to LHCb-ANA-2011-039.

[34] e. Evans, Lyndon and e. Bryant, Philip, "LHC Machine", *JINST* **3** (2008) S08001. doi:10.1088/1748-0221/3/08/S08001.

[35] M. Lamont, "LHC: Status and commissioning plans", arXiv:0906.0347. Moriond 2009 QCD session, 6 pages.

[36] http://public.web.cern.ch/press/pressreleases/Releases2010/PR07.10E.html.

[37] ATLAS Collaboration, "The ATLAS Experiment at the CERN Large Hadron Collider", *JINST* **3** (2008) S08003. doi:10.1088/1748-0221/3/08/S08003.

[38] CMS Collaboration, "The CMS experiment at the CERN LHC", *JINST* **3** (2008) S08004. doi:10.1088/1748-0221/3/08/S08004.

[39] LHCb Collaboration, "The LHCb Detector at the LHC", *JINST* **3** (2008) S08005. doi:10.1088/1748-0221/3/08/S08005.

[40] ALICE Collaboration, "The ALICE experiment at the CERN LHC", *JINST* **3** (2008) S08002. doi:10.1088/1748-0221/3/08/S08002.

[41] LHCf Collaboration, "The LHCf detector at the CERN Large Hadron Collider", *JINST* **3** (2008) S08006. doi:10.1088/1748-0221/3/08/S08006.

[42] TOTEM Collaboration, "The TOTEM experiment at the CERN Large Hadron Collider", *JINST* **3** (2008) S08007. doi:10.1088/1748-0221/3/08/S08007.

[43] http://public.web.cern.ch/public/en/research/AccelComplex-en.html.

[44] CMS Collaboration, "CMS physics: Technical design report", *CERN-LHCC-2006-001, CMS-TDR-008-1* (2006).

[45] CMS Collaboration, "The Tracker Project Technical Design Report", *"CERN/LHCC 98-6"* (1998).

[46] CMS Collaboration, "Addendum to the CMS tracker TDR", *CERN-LHCC-2000-016* (2000).

[47] CMS ECAL, "The CMS Preshower: from functional requirements to design concepts", *CMS ECAL EDR 4, Vol.2: Preshower* (2000).

[48] USCMS Collaboration, ECAL/HCAL Collaboration, "The CMS barrel calorimeter response to particle beams from 2-GeV/c to 350-GeV/c", *Eur.Phys.J.* **C60** (2009) 359–373. doi:10.1140/epjc/s10052-009-0959-5, 10.1140/epjc/s10052-009-1024-0.

[49] CMS Collaboration, "The Magnet Project Technical Design Report", *CERN/LHCC 97-10* (1997).

[50] CMS Collaboration, "Performance of the CMS Drift Tube Chambers with Cosmic Rays", *JINST* **5** (2010) T03015, arXiv:0911.4855. doi:10.1088/1748-0221/5/03/T03015.

[51] CMS Collaboration, "CMS The Muon Project Technical Design Report", *CERN/LHCC 97-32* (1997).

[52] CMS Collaboration, "CMS The TriDAS Project Technical Design Report, Volume 1: The Trigger Systems", *CERN/LHCC 2000-38* (2000).

[53] CMS Collaboration, "CMS The TriDAS Project Technical Design Report, Volume 2: Data Acquisition and High-Level Trigger", *CERN/LHCC 2002-26* (2002).

[54] CMS Collaboration, "CMS The Computing Project Technical Design Report", *CERN/LHCC 2005-23* (2005).

[55] M. Michelotto, M. Alef, A. Iribarren et al., "A comparison of HEP code with SPEC benchmarks on multi-core worker nodes", *J.Phys.Conf.Ser.* **219** (2010) 052009. doi:10.1088/1742-6596/219/5/052009.

[56] http://w3.hepix.org/benchmarks/.

[57] C. D. Spradling, "SPEC CPU2006 benchmark tools", *SIGARCH Comput. Archit. News* **35** (March, 2007) 130–134. doi:10.1145/1241601.1241625.

[58] https://cms-docdb.cern.ch/cgi-bin/DocDB/ShowDocument?docid=5928.

[59] CMS Collaboration, "CMS Computing Model", *CERN-LHCC-2004-035, CERN-CMS-NOTE-2004-031, CMS-NOTE-2004-031, LHCC-G-083* (2004).

[60] http://lcg.web.cern.ch/lcg/.

[61] Worldwide LHC Computing Grid Collaboration, "Memorandum of Understanding for Collaboration in the Deployment and Exploitation of the Worldwide LHC Computing Grid", *CERN-C-RRB-2005-01/Rev1* (2011).

[62] O. Buchmuller, D. Bonacorsi, F. Fanzago et al., "The CMS CERN Analysis Facility (CAF)", *J.Phys.Conf.Ser.* **219** (2010) 052022. doi:10.1088/1742-6596/219/5/052022.

[63] https://twiki.cern.ch/twiki/bin/view/CMSPublic/WorkBookComputingModel.

[64] G. Bagliesi, S. Belforte, K. Bloom et al., "Debugging data transfers in CMS", *J.Phys.Conf.Ser.* **219** (2010) 062055. doi:10.1088/1742-6596/219/6/062055.

[65] https://cmsweb.cern.ch/phedex/.

[66] T. Barrass, A. Afaq, W. Jank et al., "Software agents in data and workflow management", *CHEP* (2005) 838–841.

[67] http://www.dcache.org/.

[68] http://glite.cern.ch/.

[69] A. Duarte, P. Nyczyk, A. Retico et al., "Monitoring the EGEE/WLCG grid services", *J.Phys.Conf.Ser.* **119** (2008) 052014. doi:10.1088/1742-6596/119/5/052014.

[70] S. Belforte, I. Fisk, J. Flix et al., "The commissioning of CMS sites: Improving the site reliability", *J.Phys.Conf.Ser.* **219** (2010) 062047. doi:10.1088/1742-6596/219/6/062047.

[71] D. Spiga, M. Cinquilli, L. Servoli et al., "The CMS Remote Analysis Builder (CRAB)", *Lect.Notes Comput.Sci.* **4873** (2007) 580–586.

[72] J. Andreeva, S. Belov, A. Berejnoy et al., "Dashboard for the LHC experiments", *J.Phys.Conf.Ser.* **119** (2008) 062008. doi:10.1088/1742-6596/119/6/062008.

[73] https://ekptrac.physik.uni-karlsruhe.de/trac/HappyFace/wiki/Version_2.

[74] V. Mauch, C. Ay, S. Birkholz et al., "The HappyFace project", *J.Phys.Conf.Ser.* **331** (2011) 082011. doi:10.1088/1742-6596/331/8/082011.

[75] V. Buge, V. Mauch, G. Quast et al., "Site specific monitoring of multiple information systems: The HappyFace project", *J.Phys.Conf.Ser.* **219** (2010) 062057. doi:10.1088/1742-6596/219/6/062057.

[76] https://sqlite.org/.

[77] http://wwwiexp.desy.de/groups/cms/tier2_monitoring/HappyFaceV2/trunk/webpage/index.php.

[78] A. Gellrich, "A multi VO grid infrastructure at DESY", *J.Phys.Conf.Ser.* **219** (2010) 062048. doi:10.1088/1742-6596/219/6/062048.

[79] https://lemon.physik.rwth-aachen.de/webpage/.

[80] http://ekphappyface.physik.uni-karlsruhe.de/~happyface/gridka/webpage/.

[81] T. Sjostrand, S. Mrenna, and P. Z. Skands, "PYTHIA 6.4 Physics and Manual", *JHEP* **0605** (2006) 026, arXiv:hep-ph/0603175. doi:10.1088/1126-6708/2006/05/026.

[82] J. Alwall, P. Demin, S. de Visscher et al., "MadGraph/MadEvent v4: The New Web Generation", *JHEP* **0709** (2007) 028, arXiv:0706.2334. doi:10.1088/1126-6708/2007/09/028.

[83] F. E. Paige, S. D. Protopopescu, H. Baer et al., "ISAJET 7.69: A Monte Carlo event generator for pp, anti-p p, and e+e- reactions",. http://www.nhn.ou.edu/~isajet/isajet782.ps.

[84] S. Jadach, J. H. Kuhn, and Z. Was, "TAUOLA: A Library of Monte Carlo programs to simulate decays of polarized $\tau$ leptons", *Comput.Phys.Commun.* **64** (1990) 275–299. doi:10.1016/0010-4655(91)90038-M.

[85] J. Allison, K. Amako, J. Apostolakis et al., "Geant4 developments and applications", *IEEE Trans.Nucl.Sci.* **53** (2006) 270. doi:10.1109/TNS.2006.869826.

[86] https://twiki.cern.ch/twiki/bin/view/CMSPublic/SWGuideFastSimulation.

[87] W. Beenakker, R. Hopker, and M. Spira, "PROSPINO: A Program for the production of supersymmetric particles in next-to-leading order QCD", arXiv:hep-ph/9611232.

[88] M. L. Perl, G. Abrams, A. Boyarski et al., "Evidence for Anomalous Lepton Production in e+ - e- Annihilation", *Phys.Rev.Lett.* **35** (1975) 1489–1492. doi:10.1103/PhysRevLett.35.1489.

[89] M. L. Perl, "Evidence for, and Properties of, the New Charged Heavy Lepton", *SLAC-PUB-1923* (1977). Microfiche at Fermilab.

[90] CMS Collaboration, "Particle-Flow Event Reconstruction in CMS and Performance for Jets, Taus, and $E_T^{miss}$", *CMS-PAS-PFT-09-001* (2009).

[91] CMS Collaboration, "CMS Strategies for tau reconstruction and identification using particle-flow techniques", *CMS-PAS-PFT-08-001*.

[92] https://twiki.cern.ch/twiki/bin/view/CMSPublic/SWGuidePFTauID.

[93] C. Collaboration, "Performance of tau-lepton reconstruction and identification in CMS", *JINST* **7** (2012) P01001, arXiv:1109.6034.

[94] CMS Collaboration, "Measurement of the Inclusive Z Cross Section via Decays to Tau Pairs in $pp$ Collisions at $\sqrt{s} = 7$ TeV", *JHEP* **1108** (2011) 117, arXiv:1104.1617. doi:10.1007/JHEP08(2011)117.

[95] CMS Collaboration, "Search for new physics at CMS with jets and missing momentum", *CMS-PAS-SUS-10-005* (2011).

[96] CMS Collaboration, "Determination of Jet Energy Calibration and Transverse Momentum Resolution in CMS", *JINST* **6** (2011) P11002, arXiv:1107.4277. doi:10.1088/1748-0221/6/11/P11002.

[97] Andres Delannoy, Will Flanagan, Alfredo Gurrola, Will Johns, Teruki Kamon, Jieun Kim, Andrew Melo, Roy Montalvo, Sinjini Sengupta, Paul Sheldon, "Search for Supersymmetry in Tau Final States", *CMS AN-2011/519* (2012).

[98] CMS Collaboration, "Missing transverse energy performance of the CMS detector", *JINST* **6** (2011) P09001, arXiv:1106.5048. doi:10.1088/1748-0221/6/09/P09001.

[99] CMS Collaboration, "Search for Physics Beyond the Standard Model in Events with Opposite-sign Tau Pairs and Missing Energy", *CMS PAS SUS 11-007* (2011).

[100] J. Thomsen, "Search for Supersymmetry in the Hadronic Channel with Data from the CMS Experiment". PhD thesis, University of Hamburg, Germany, 2012.

[101] CMS Collaboration, "Tau identification in CMS", *CMS-PAS-TAU-11-001* (2011).

[102] CMS Collaboration, "Absolute Calibration of the Luminosity Measurement at CMS: Winter 2012 Update", *CMS PAS SMP-12-008* (2012).

[103] M. Pioppi (2012). private communication.

[104] H1 and ZEUS Collaboration, "Combined Measurement and QCD Analysis of the Inclusive e+- p Scattering Cross Sections at HERA", *JHEP* **1001** (2010) 109, arXiv:0911.0884. doi:10.1007/JHEP01(2010)109.

[105] A. L. Read, "Modified frequentist analysis of search results (the $CL_s$ method)", in *1st Workshop on Confidence Limits*, L. Lyons, Y. Perrin, and F. E. James, eds. CERN, Geneva, 2000. CERN-OPEN-2000-205.oai:cds.cern.ch:451614.

[106] A. L. Read, "Presentation of search results: the $CL_s$ technique", *Journal of Physics G: Nuclear and Particle Physics* **28** (2002), no. 10, 2693 – 2704. doi:10.1088/0954-3899/28/10/313.

[107] T. Junk, "Confidence level computation for combining searches with small statistics", *Nuclear Instruments and Methods in Physics Research Section A: Accelerators, Spectrometers, Detectors and Associated Equipment* **434** (1999), no. 2-3, 435 – 443. doi:10.1016/S0168-9002(99)00498-2.

[108] https://twiki.cern.ch/twiki/bin/view/RooStats/WebHome.

[109] K. Matchev, R. Remington, "Updated templates for the interpretation of LHC results on supersymmetry in the context of mSUGRA", *arXiv:1202.6580* (2012).

[110] D0 Collaboration Collaboration, "The Upgraded D0 detector", *Nucl.Instrum.Meth.* **A565** (2006) 463–537, arXiv:physics/0507191. doi:10.1016/j.nima.2006.05.248.

[111] http://www-bd.fnal.gov/lug/runII_handbook/RunII_index.html.

[112] D0 Collaboration Collaboration, "Search for squark production in events with jets, hadronically decaying tau leptons and missing transverse energy at $\sqrt{s} = 1.96$ TeV", *Phys.Lett.* **B680** (2009) 24–33, arXiv:0905.4086. doi:10.1016/j.physletb.2009.08.002.

[113] D0 Collaboration Collaboration, "Search for squarks and gluinos in events with jets and missing transverse energy using 2.1 $fb^{-1}$ of $p\bar{p}$ collision data at $\sqrt{s} = 1.96$ TeV", *Phys.Lett.* **B660** (2008) 449–457, arXiv:0712.3805. Submitted to Phys. Lett. B. doi:10.1016/j.physletb.2008.01.042.

[114] "Search for supersymmetry with jets, missing transverse momentum and one or more tau leptons in proton-proton collisions at $\sqrt{s} = 7$ TeV with the ATLAS detector", Technical Report ATLAS-CONF-2012-005, CERN, Geneva, (Feb, 2012).

[115] "Search for Events with Large Missing Transverse Momentum, Jets, and at Least Two Tau Leptons in 7 TeV Proton-Proton Collision Data with the ATLAS Detector", Technical Report ATLAS-CONF-2012-002, CERN, Geneva, (Feb, 2012).

[116] CMS Collaboration, "Absolute Calibration of Luminosity Measurement at CMS: Summer 2011 Update", *CMS-PAS-EWK-11-001* (2011).

[117] "Search for supersymmetry with the razor variables at CMS", *PAS-SUS-12-005* (2012).

[118] https://twiki.cern.ch/twiki/bin/view/CMSPublic/PhysicsResultsSUS12010.

# Acknowledgments

A lot of people helped to make this thesis become real, to whom I would like to express my gratitude.
First, I would like to thank Prof. Peter Schleper for a series of inspiring conversations, useful courtesy and for the opportunity to be part of his working group.
I also thank Prof. Dr. Teruki Kamon for referring my thesis, and also for supporting me with his vast experience and encouragement.
In addition, I am obliged to Dr. Isabell Melzer-Pellmann and Prof. Johannes Haller for referring my disputation.
Especially thankful I am to Prof. Christian Sander, as he was always of a great help and also very patient with his padawan.
I thank all postdocs who supervised me at times, especially Dr. Hartmut Stadie for introducing me to Computing and for the disputes we always liked to have.
Representative for the working group, I would like to thank my office comrades Dr. Holger Enderle and Matthias Schröder for the immense knowledge they shared with me, and Dr. Ulla Gebbert and Dr. Jan Thomsen for the constructive words in phases where nothing would work out as planned. I thank all for the relaxed and motivating athmosphere and for the shared activities beyond physics.
Zu guter letzt danke ich meiner Familie und meinen Freunden, insbesondere Inga Röwer, AC Weber, Kai Körber und Henrik Nowak, die trotz der Tatsache, dass ich für sie nur wenig Zeit übrig hatte, meinen Namen nicht vergaßen, und die hin und wieder eine Wochenendbetreuung organisierten, um mich von allzu widerspenstiger Arbeit abzulenken.

Thank you all.